

COARSENING OF THIN FLUID FILMS

by

Michael B. Gratton

Department of Mathematics
Duke University

Date: _____

Approved:

Thomas P. Witelski, Advisor

Michael Shearer

Stephanos Venakides

John Trangenstein



Dissertation submitted in partial fulfillment of the requirements for the degree of
Doctor of Philosophy in the Department of Mathematics
in the Graduate School of Duke University
2008

ABSTRACT
(Mathematics)

COARSENING OF THIN FLUID FILMS

by

Michael B. Gratton

Department of Mathematics
Duke University

Date: _____

Approved:

Thomas P. Witelski, Advisor

Michael Shearer

Stephanos Venakides

John Trangenstein

An abstract of a dissertation submitted in partial fulfillment of the requirements for
the degree of Doctor of Philosophy in the Department of Mathematics
in the Graduate School of Duke University
2008

Copyright © 2008 by Michael B. Gratton
All rights reserved except those rights granted by the
Creative Commons Attribution-Noncommercial Licence

Abstract

Observed in many physical systems, coarsening is an orderly decrease in the number of localized structures, such as particles, drops, shear bands, solitons, or point defects. Coarsening is a type of pattern formation in which the characteristic length scale between features grows while the total number of features decreases. These phenomena have been studied in many problems and several mathematical techniques for modeling these phenomena have been developed. This dissertation examines the aggregation of drops in the thin film equation, where drops may coarsen through two general mechanisms: collision and collapse. A series of simplifications to model this process is developed. Slender-body asymptotics is applied to the Navier-Stokes equations for fluid motion in order to derive the Reynolds lubrication equation. The lubrication equation is in turn simplified to a coarsening dynamical system (CDS) model for interacting drops through solvability conditions for a perturbation about a drop-type steady state. Lastly, the dynamical system is averaged into an ensemble model to describe the dynamics of the distribution of drop sizes.

The ensemble model takes the form of an integro-differential equation for the distribution function, much like the model of Ostwald ripening proposed by Lifshitz and Slyozov. A convenient choice of scaling yields an intermediate asymptotic self-similar solution. This solution is compared to numerical simulations of the ensemble model and histograms of drop masses from the CDS model. The early-time dynamics before similarity are explored by varying the initial distribution of drop sizes. Interesting far-from-similarity “stairstep” behavior is observed in the coarsening rate when the initial distribution has a very small variance. A well-chosen initial condition with a fractal-like structure is shown to replicate the stairstep behavior.

At very long times, the mean drop size grows large, requiring the inclusion of gravity in the model. The CDS model parameters are modified as a result of the dependence of drop shapes on both size and gravity. The new dynamical system predicts the coarsening rate slowing from a power law to an inverse logarithmic rate. The energy liberated by each coarsening event is shown to approach a gravity-dependent constant as the mean drop mass increases. This suggests a reason for the coarsening slow-down.

To Melanie Bain, for at least a million reasons

Contents

Abstract	iv
List of Figures	x
Acknowledgements	xiii
1 Introduction	1
1.1 Coarsening problems	1
1.2 Thin fluid films with high surface tension	2
1.3 Illustration of thin film coarsening	4
1.4 Plan of the dissertation	5
2 Reynolds lubrication equation	7
2.1 Surface tension driven spreading	11
2.2 Asymptotic behavior of the linearized equation	13
2.3 Intermolecular forces	15
2.4 Uniform film instabilities	20
3 Steady-state droplet solutions	23
3.1 Phase plane description of bounded solutions	23
3.2 Asymptotic description of drop solutions	29
3.2.1 Drops with no gravitational influence	30
3.2.2 Drops with shapes modified by gravity	32

4	Coarsening dynamical system model	37
4.1	Quasi-static model for a single drop with applied fluxes	38
4.2	Arrays of interacting drops	45
4.3	Coarsening Dynamical System (CDS)	47
4.3.1	Modes of coarsening and coarsening rules	48
4.3.2	Thin film CDS	49
4.4	Dilute limit of the CDS	52
5	Droplets coarsening subject to gravity	54
5.1	CDS model parameters	55
5.2	Non-power-law behavior	57
5.3	Energy incentive to coarsen for large drops	63
5.3.1	Basic expansions of the energy	64
5.3.2	Energy released in a two-drop system	66
6	Distribution model for drop coarsening	69
6.1	Mean-field model for drop distributions	71
6.1.1	Model formulation	71
6.1.2	Asymptotic separation of variables	75
6.2	Effect of the initial distribution	79
6.3	Early-time deviations: Stairsteps	82
7	Future directions for research	87
7.1	Collision dominated coarsening distributions	87
7.2	Coarsening in two dimensions	89
A	Physical variables simulation of the lubrication equation	91
A.1	Discretization	92
A.2	Initial conditions and adaptive time-stepping	95

Bibliography

96

Biography

103

List of Figures

1.1	Time series of a dewetting and coarsening film.	4
2.1	A two-dimensional thin film bounded below by a flat substrate.	8
2.2	Oscillations in linearized film equation.	14
2.3	The generalized wetting potential.	18
2.4	The dispersion relation for spinodal dewetting.	21
2.5	The second derivative of the wetting potential.	22
3.1	A schematic of a large thin film droplet.	24
3.2	The fixed points of the steady-state equation as determined by the wetting potential.	25
3.3	The phase plane for a small droplet-type solution.	26
3.4	The phase plane for a large droplet-type solution.	27
3.5	The phase plane for a dimple-type solution.	28
3.6	The phase plane for the heteroclinic solution	29
3.7	The bifurcation diagram for fixed points h_m, h_c, h_α of the steady-state film equation.	30
3.8	Drop profiles for $\alpha = 0.1$ and different pressures $P^* < P < P_{\max}$	32
3.9	Drop profiles for mass $m = 20$ and $0 \leq \alpha \leq 0.4$	33
3.10	The relationship of drop mass m to drop pressure P	36
4.1	The drift coefficient C_x for several values of α	44
4.2	The flux between two droplets as determined by their pressures.	47
4.3	The collision mode of coarsening.	50
4.4	The collapse mode of coarsening.	51
5.1	A numerical simulation of the PDE (2.40) with a small array of interacting drops.	55

5.2	CDS computations with and without droplet drift.	56
5.3	The coarsening rate as modified by α	58
5.4	The coarsening rate as affected by changing \bar{m}_0 , with $0.5 \leq \bar{m}_0 \leq 20$ and fixed $\alpha = 0.1$	59
5.5	The mean log excess pressure \bar{Q} versus τ for the simulations shown in Fig 5.3.	60
5.6	The data appearing in Fig 5.4 replotted using similarity variables. . .	61
5.7	The similarity scaling showing power law and inverse logarithmic be- havior as pieces of a larger trend.	62
5.8	The energy change from a single coarsening event as a function of drop mass.	66
5.9	The energy change from a single coarsening event excluding ΔE_{wl} . . .	67
6.1	An initially uniform random distribution of drops (bold curve) con- verging to the similarity distribution.	70
6.2	A simulation of the drop distribution model (6.12) via a characteristic tracking method.	74
6.3	The characteristic velocity from the mean-field model compared to the bin-averaged velocities from a CDS simulation.	77
6.4	The asymptotic distribution f compared to the averaged self-similar CDS histogram.	78
6.5	The evolution of four initial drop mass distributions in the CDS model.	80
6.6	The distribution of drop masses from spinodal dewetting.	81
6.7	The far-from-similarity coarsening of an initially uniform random dis- tribution of drops with a small variance.	83
6.8	Histograms at various times during the simulation shown in Fig. 6.7.	84
6.9	The evolution of the “fractal” initial condition (6.26) in the CDS model.	85
7.1	World lines of colliding droplets with $\mathbb{K} = 1.5$	89
A.1	The stencil for the four-equation discretization of the film equation (2.40)	92
A.2	A packing diagram for the Jacobian of (A.2).	93

A.3	The computer time for a test problem using the traditional one equation approach for the film equation and the four equation approach (A.1).	94
-----	--	----

Acknowledgements

This work was supported by the National Science Foundation Division of Mathematical Sciences grant numbers 0244498 FRG and 0239125 CAREER. In addition, travel support was kindly provided by Imperial College London, the Engineering Science Research Council (UK), the American Physical Society, and the Society for Industrial and Applied Mathematics. I am also grateful to the Oxford Center for Industrial and Applied Mathematics for their hospitality in September 2007.

I would like to thank the many people who supported my graduate school endeavors. In particular:

- Tom Witelski for his patience and guidance,
- Thomas Laurent for teaching me analysis,
- Nicholas Robbins and Michael Nicholas for teaching me the rest of math,
- Jeff Streets for helping me waste time,
- Abe Smith for the “fireside chats” sans fire,
- Paul Bendich for going insane so I didn’t have to,
- and Ryan Haskett for whiskey and emotional support.

Introduction

Coarsening is an orderly decrease of the number of localized structures, such as particles, drops, shear bands, solitons, or point defects in a physical system. Coarsening is a type of pattern formation in which the characteristic length scale between features grows while the total number of features decreases. These phenomena have been studied in many problems and several mathematical modeling techniques have been developed to describe the dynamics. This chapter briefly reviews the hundred history of coarsening problems and techniques for studying them. It then describes the history of the lubrication approximation as a modeling tool for thin viscous liquid films. Finally, it concludes with the plan of the dissertation.

1.1 Coarsening problems

Coarsening problems have been of interest to mathematicians and physicists since at least the seminal work of Wilhelm Ostwald in 1896 [53]. He described the ripening of small particles of precipitate in a supersaturated fluid into fewer, larger particles. Sixty-five years later, Lifshitz and Slyozov [38] and independently Wagner [75]

developed a mathematical model for the process that treated the ensemble, or distribution, of particle sizes. Their model allowed the observations of Ostwald ripening to be compared with surprisingly simple self-similarity arguments.

The success of a self-similar solution in describing coarsening is indicative of the self-organizing structure of the dynamics. Coarsening is a type of pattern formation in the sense that the distribution of particle sizes approaches the similarity distribution. As time progresses, the typical scale of the pattern grows, as seen in [9, Fig. 2].

Modern methods in coarsening include analytic approaches, such as the Kohn and Otto technique [35], which employs optimal transport theory in order to prove upper bounds on the mean coarsening rate. This technique has been successfully applied to a variety of physical problems, from precipitate ripening to shear bands aggregation in granular flow to thin film droplets coalescing [18, 54, 13]. However, the implications of bounds on the mean coarsening rate provided by this technique can be unexpected, as is illustrated in Chapter 6. Other techniques include coarsening dynamical systems (CDS) [76, 12, 80] and improvements and generalizations of the Lifshitz and Slyozov technique (see [73] for a review). The survey paper by Bray [9] discusses other approaches to modeling coarsening using ideas originating from electromagnetic scattering theory.

1.2 Thin fluid films with high surface tension

Lubrication theory is an important mathematical modeling tool that has proved very adaptable. It is a simplification of the Navier-Stokes equations of fluid motion appropriate for thin, viscous fluid films. Osborne Reynolds developed the theory in 1886 to describe the motion of slider bearings [60] where the lubricating oil sustains incredible force loads from a top-plate without dewetting, where the height of the

oil goes to zero. The large forces result in large pressures in the Navier-Stokes equations [52], and Reynolds' rescaling of these equations takes advantage of this fact. Reynolds' work was focused on films confined between two plates, but later authors generalized the model to include a free liquid-air interface whose position must be determined in solving the model. This version describes many industrial problems that are not necessarily lubrication: painting, masking, spin-coating, and others.

Interestingly, the lubrication equation suffers from a non-integrable singularity at the air-liquid-solid contact line surrounding a drop, or wherever the height of the interface is zero in a larger film [5]. There has been much mathematical interest in describing this break-down (such as [3]). As is typical in fluids, a no-slip condition is applied along the solid substrate so that the fluid velocity there is zero in the frame of the substrate. There is a disconnect between this condition and the need for there to be some nonzero velocity at the height zero contact line to allow a drop to spread. From a physical perspective, the mathematical singularity results in a divergence of the force required to move the contact line. The contact line involves a communication between the macroscopic continuum scale of the drop and the molecular scale of the substrate and fluid just at contact, so it is unlikely that basic lubrication theory can describe its motion. The resolution of this contact line paradox is still a matter of academic debate [44]. One approach to regularizing the problem is discussed in Chapter 2, where the addition of long-range molecular forces such as van der Waals interactions prevents the height of the film from reaching zero. These forces are meant to approximate the molecular dynamics and operate only over short ranges in the thin film equation. A drawback of this approach is that this regularization is only justified when these interactions actually occur in the physical system, and it makes the model dependent on properties of the substrate and the gas, as well as properties of the liquid. Fortunately, dewetting and coarsening

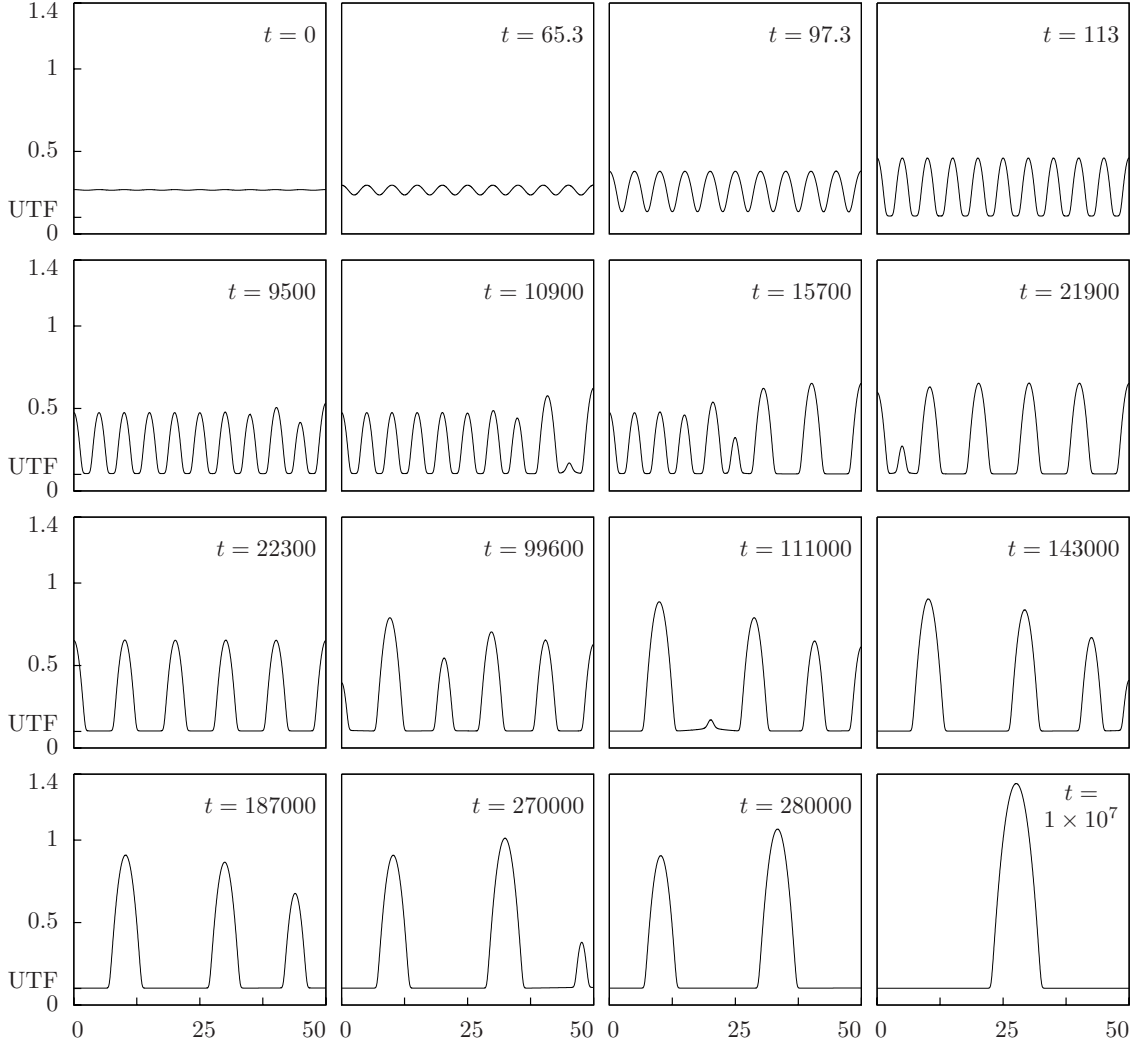


FIGURE 1.1: Time series of a dewetting and coarsening film. Each plot is of the liquid surface $h(x,t)$ versus x at the specified t .

are phenomena that are caused by the presence of these forces, so their inclusion in this study is both necessary and physically justified.

1.3 Illustration of thin film coarsening

The lubrication equation, with the inclusion of intermolecular forces, is capable of a variety of interesting dynamics. Figure 1.1 shows snapshots in time of an initially uniform one-dimensional film $h(x,t)$, plotted as h versus x , spontaneously dewetting

into a set of nearly identical droplets connected by an ultra-thin film (UTF). The UTF height is marked on the h axis. Drops are localized with non-overlapping essential supports (widths or radii) and are only weakly coupled together. Over very long timescales, the drop array evolves quasi-statically, coarsening into one large drop. The coarsening itself consists of two modes: drops may drift left or right, or they may exchange mass through the UTF with their neighbors. These two modes lead to two types of coarsening events. In a collision event, the essential supports of two drops touch and the drops rapidly merge together. In a collapse event, a drop loses all of its mass to its neighbors, leaving behind only ultra-thin film. All coarsening events in Fig. 1.1 are collapse-type events. The computations were performed by using the technique described in Appendix A to simulating the partial differential equation (2.40). The parameters are $\delta = 0.1$ and $\alpha = 0.05$, as defined in (2.31) and (2.35).

1.4 Plan of the dissertation

This dissertation explores thin film droplet coarsening by constructing simplified models to investigate the phenomenon at different levels of detail. In Chapter 2, we derive the thin film equation for hydrodynamic lubrication with the addition of the intermolecular force term discussed above. We also show how this force can lead to film rupture. While the lubrication equation is sufficiently detailed to display coarsening behavior, we derive a further simplification to allow larger scale numerical simulations. This takes the form of a dynamical system model for drop interaction. In Chapter 3, we examine droplet-type steady-state solutions to the thin film equation through phase plane methods. In Chapter 4, we develop a CDS model for thin film drops through solvability conditions for a perturbation about a steady-state drop. In Chapter 5, we explore the effect of gravity on the coarsening rate, effectively the

long-time dynamics of a very large coarsening system. Finally, in Chapter 6 we discuss a Lifshitz and Slyozov-style further simplification of coarsening and develop a theory for the distribution of drop masses during coarsening. Using this model and histograms of drops from CDS simulations, we explore self-similar coarsening and far-from-similarity behavior. Chapter 7 looks forward to new directions in thin film coarsening, namely work in higher dimensions and collision-based coarsening distributions. Appendix A contains details of the numerical method used to solve the thin film equation. Portions of Chapters 3 and 5 are derived from [26] by Gratton and Witeliski.

Reynolds lubrication equation

The Reynolds lubrication equation is a simplification of the Navier-Stokes equations for fluid motion appropriate to model thin viscous liquid films on a solid substrate. It uses three principle assumptions: a long wavelength approximation (the height-scale compared to the length-scale of a typical feature is small), a small Reynolds number approximation, and an assumption of large surface tension. By depth-averaging, the evolution equation is reduced to a single partial differential equation (PDE) for the height of the film, though the velocity field of the fluid can be calculated if required. The lubrication equation is also known as the thin film equation, and we will use the two terms interchangeably.

Consider a thin layer of incompressible Newtonian liquid in two dimensions governed by a body force (such as gravity) and the surface tension at the liquid-gas interface. The fluid is constrained below by a solid substrate, but has a free surface whose location must be found along with the velocity of the fluid, see Fig. 2.1. Following the derivation of Oron et al. [52], we begin with the Navier-Stokes equations

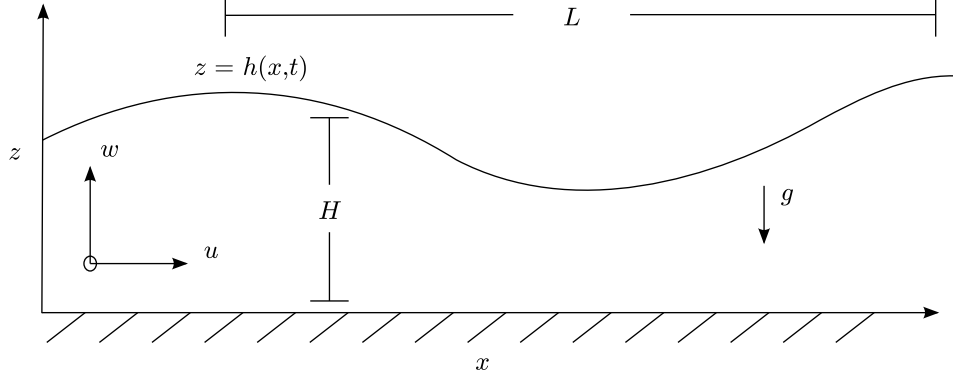


FIGURE 2.1: A two-dimensional thin film bounded below by a flat substrate.

for the velocity field (\hat{u}, \hat{w}) ,

$$\partial_t \hat{u} + \hat{u} \partial_x \hat{u} + \hat{w} \partial_z \hat{u} = -\frac{1}{\rho} \partial_x \hat{p} + \nu \nabla^2 \hat{u} - \frac{1}{\rho} \partial_x \hat{\phi} \quad (2.1a)$$

$$\partial_t \hat{w} + \hat{u} \partial_x \hat{w} + \hat{w} \partial_z \hat{w} = -\frac{1}{\rho} \partial_z \hat{p} + \nu \nabla^2 \hat{w} - \frac{1}{\rho} \partial_z \hat{\phi} \quad (2.1b)$$

$$\partial_x \hat{u} + \partial_z \hat{w} = 0, \quad (2.1c)$$

where ρ is the density, ν is the viscosity, \hat{p} is the pressure, and $\hat{\phi}$ represents the potential for other conservative body forces (such as gravity). Along the substrate we impose a no-slip condition $\hat{u}(\hat{z} = 0) = 0$, and at the free surface $\hat{z} = \hat{h}(\hat{x}, \hat{t})$ we impose both a surface continuity condition

$$\hat{w} = \partial_t \hat{h} + \hat{u} \partial_x \hat{h}, \quad (2.2a)$$

and a stress-balance condition

$$\mathbf{T} \cdot \vec{n} = \left[-\hat{p}I + \mu \begin{pmatrix} 2\frac{\partial \hat{u}}{\partial x} & \frac{\partial \hat{u}}{\partial z} + \frac{\partial \hat{w}}{\partial x} \\ \frac{\partial \hat{u}}{\partial z} + \frac{\partial \hat{w}}{\partial x} & 2\frac{\partial \hat{w}}{\partial z} \end{pmatrix} \right] \cdot \vec{n} = -\sigma \hat{\kappa} \vec{n}. \quad (2.2b)$$

The latter condition balances surface tension with the jump in stress across the interface. Here, \mathbf{T} is the stress tensor, $\hat{\kappa}$ is the mean curvature, σ is the surface tension, and \vec{n} is the unit outward normal vector.

Our principle assumption will be that the fluid film is thin, and we rescale (2.1) to take advantage of this. Let

$$\epsilon = H/L, \quad x = \hat{x}/L, \quad z = \hat{z}/H, \quad (2.3)$$

where $\epsilon \ll 1$ is the aspect ratio. The velocity scales are constrained by the incompressibility condition (2.1c) to be scaling to be

$$u = \hat{u}/U \quad \text{and} \quad w = \hat{w}/(\epsilon U). \quad (2.4)$$

The timescale is set to $t = H/(\epsilon U)$, consistent with the length and velocity scales. We seek a perturbation solution in the limit $\epsilon \rightarrow 0$ of (2.1). The $\text{Re} \rightarrow 0$ assumption removes the inertial terms from the left-hand side. This forces us to rescale pressure to balance viscosity: $p = \epsilon H/(\mu U)\hat{p}$. As expected in lubrication, pressures are large. For consistency, we apply the same scaling to the force, $\phi = \epsilon H/(\mu U)\hat{\phi}$. At leading order in ϵ ,

$$0 = -\partial_x p + \partial_{zz} u - \partial_x \phi \quad (2.5a)$$

$$0 = -\partial_z p - \partial_z \phi \quad (2.5b)$$

$$0 = \partial_x u + \partial_z w \quad (2.5c)$$

with boundary conditions

$$u = w = 0 \quad \text{at} \quad z = 0 \quad (2.6a)$$

$$w = \partial_t h + u \partial_x h \quad \text{at} \quad z = h. \quad (2.6b)$$

The condition on the stress jump across the interface is more involved. In the rescaled variables,

$$\vec{n} = \frac{1}{\sqrt{1 + (\epsilon \partial_x h)^2}} \begin{pmatrix} -\epsilon \partial_x h \\ 1 \end{pmatrix}, \quad \vec{\tau} = \frac{1}{\sqrt{1 + (\epsilon \partial_x h)^2}} \begin{pmatrix} 1 \\ -\epsilon \partial_x h \end{pmatrix},$$

$$\kappa = \frac{\epsilon^2 \partial_{xx} h}{H[1 + (\epsilon \partial_x h)^2]^{3/2}},$$

and

$$\mathbf{T} \cdot \vec{n} = \frac{\mu U}{H} \left[-\frac{p}{\epsilon} \begin{pmatrix} -\epsilon \partial_x h \\ 1 \end{pmatrix} + \begin{pmatrix} -2\epsilon^2 \partial_x h \partial_x u + \partial_z u + \epsilon^2 \partial_x w \\ -\epsilon \partial_x h [\partial_z u + \epsilon^2 \partial_x w] + 2\epsilon \partial_z w \end{pmatrix} \right].$$

Component-wise, the stress jump condition is

$$\mathbf{T} \cdot \vec{n} \cdot \vec{\tau} = \frac{\mu U}{H} (\partial_z u + O(\epsilon^2)) = 0 \quad (2.7a)$$

$$\mathbf{T} \cdot \vec{n} \cdot \vec{n} = p + O(\epsilon^2) = -\frac{\sigma}{U\mu} \epsilon^3 \partial_{xx} h \quad (2.7b)$$

at $z = h$. The inverse of the constant term, $C = \mu U / \sigma$, is known as the *capillary number* — the ratio of surface tension effects to viscosity. We will assume that surface tension is quite strong, so that $\epsilon^3 C^{-1} = O(1)$, and we will take it to be exactly one for simplicity.

Next we rewrite (2.6b) using integration by parts and the boundary conditions at $z = 0$ to obtain

$$\partial_t h + \partial_x \int_0^h u \, dz = 0, \quad (2.8)$$

a depth-averaged version of surface continuity. Depth-averaging reduces ϕ to a function of h , so we replace ϕ by $\Phi(h)$.¹ Proceeding from (2.5b), we can integrate using (2.7b) to determine the constant of integration, obtaining

$$p = \Phi - \partial_{xx} h. \quad (2.9)$$

Integrating (2.5a) twice in z and applying the no-slip condition (2.6a) gives

$$u = \partial_x p \left(\frac{1}{2} z^2 - zh \right). \quad (2.10)$$

Using (2.8) to replace u yields

$$\partial_t h - \partial_x \left(\frac{1}{3} h^3 \partial_x p \right) = 0. \quad (2.11)$$

¹ see [30] for a more detailed explanation where ϕ is a long range inter-molecular force.

Note that surface tension and the body force ϕ both are absorbed into p . The full equation is

$$\partial_t h - \partial_x \left(\frac{1}{3} h^3 \partial_x [\partial_x \Phi - \partial_{xx} h] \right) = 0. \quad (2.12)$$

We will later add physics to the model through Φ , including gravitational and intermolecular forces.

Revisiting the three assumptions of lubrication theory shows the limitations of (2.12). If the aspect ratio is not small, the full form of the curvature governs the dynamics. Even for a static drop, the full curvature creates shapes that are spherical caps rather than the parabolas shown in Chapter 3. If Re is not small, the behavior can be very different. This can occur even for systems with small aspect ratios if there is a significant velocity, such as drops falling from a syringe. If $\epsilon^3 C^{-1} = O(1)$ condition on the capillary number is not met, the thin film equation reduces to creeping flow, with an equation for the interface height identical to the porous media equation [1, Chap. 2].

While not necessary for computing the film evolution, the velocity field can be found from the incompressibility condition as

$$u = \partial_x (\Phi - \partial_x^2 h) \left(\frac{1}{2} z^2 - zh \right) \quad (2.13)$$

$$v = \partial_x^2 (\Phi - \partial_x^2 h) \left(z^3 - \frac{1}{2} z^2 h \right) - \partial_x (\Phi - \partial_x^2 h) \frac{1}{2} z \partial_x h. \quad (2.14)$$

These may be used to compute streamlines inside of a thin film, see [57] for example. Note this is a function of x and t only through the dependence on $h(x, t)$.

2.1 Surface tension driven spreading

Some insight into the behavior of the thin film equation may be obtained by looking at the basic scaling properties of the full equation. Consider arbitrary scales $h = H\tilde{h}$, $t = T\tilde{t}$, and $x = L\tilde{x}$ applied to (2.12), resulting in

$$\frac{H}{T} \partial_{\tilde{t}} \tilde{h} = \frac{H^4}{L^4} \partial_{\tilde{x}} (\tilde{h}^3 \partial_{\tilde{x}}^3 \tilde{h}), \quad (2.15)$$

Looking at the scaling alone, it is natural to choose $T = L^4 H^{-3}$. Conservation of mass implies

$$M = \int_{\Omega} h \, dx = \int_{\Omega} HL\tilde{h} \, d\tilde{x} \quad (2.16)$$

should be free of the timescale. This can be accomplished by setting $H = L^{-1}$. Thus

$$H = T^{-1/7} \quad (2.17)$$

is a self-similar scaling of the thin film equation. Tanner first described this relationship for the time dependence of the radius of a spreading drop [69]. The generalized thin film equation (where the h^3 term is replaced with h^n in (2.11)) has an important source-type similarity solution whose structure obeys a similar scaling, as described in [4]. However, King [33] and King and Bowen [34] show that in the limit of $n \rightarrow 3$, this solution breaks down. Even without a proper similarity solution, in the absence of other forces a droplet $h(x, t)$ of fluid will spread in a manner consistent with this scaling so that $h \rightarrow 0$ like $t^{-1/7}$. Physical fluids whose heights may decay to zero are said to *completely wet* the substrate they spread on.

Mathematically, spreading drop solutions present a problem because the singularities in the pressure that result when $h = 0$ cannot be integrated. Away from the region of zero height, the fluid has some nonzero velocity, but where $h = 0$ the h^3 nonlinear diffusivity-type term is also zero and information cannot propagate beyond this point. The inability of the lubrication model to simulate dry contact has long been recognized as a major shortcoming of the model [5, 82, 3, 31].

Several regularizations have been proposed to avoid this difficulty, including Navier slip models [52], contact angle-contact line velocity relations [69], and diffuse interface models [55]. Each introduces a new parameter: a slip length, a proportionality constant for the velocity, or the strength of the diffuse interface potential. In

general, these must be fit from experiments rather than determined by theory. In some limits, these disparate regularizations may be made self-consistent [17].

The simplest method to avoid the difficulty is to add a prewetting layer of fluid of height $\delta \ll 1$ everywhere in the domain. This method hopes to prevent $h \rightarrow 0$ by choosing δ large enough to avoid dewetting. However, analysis of the linearized equation shows the flaw in this approach.

2.2 Asymptotic behavior of the linearized equation

Linearizing the thin film equation (2.11) about a flat state, $h = \bar{h} + \varepsilon\psi$ results in

$$\partial_t \psi = -\bar{h}^3 \partial_x^4 \psi, \quad (2.18)$$

a fourth-order version of the heat equation. We seek the fundamental solution of this equation to understand its character, and proceed through a similarity argument. A dimensional analysis similar to the one above suggests similarity variables

$$t^{-1/4} \Psi(\eta) = \psi, \quad \eta = x/t^{1/4}. \quad (2.19)$$

Applying this scaling gives the similarity differential equation

$$(\eta\Psi)' = \eta\Psi'''' . \quad (2.20)$$

Integrating once yields

$$\eta\Psi = 4\Psi''', \quad (2.21)$$

where the constant of integration must be zero to conserve mass. We can find an asymptotic solution through the WKB approximation by expanding the equation about $\eta \rightarrow \infty$ [2, Sec. 7.2]. This is an irregular singular point of the equation, so we seek solutions of the type $\Psi = e^{s(\eta)}$. This ansatz gives

$$\eta/4 = s''' + 3s''s' + (s')^3. \quad (2.22)$$

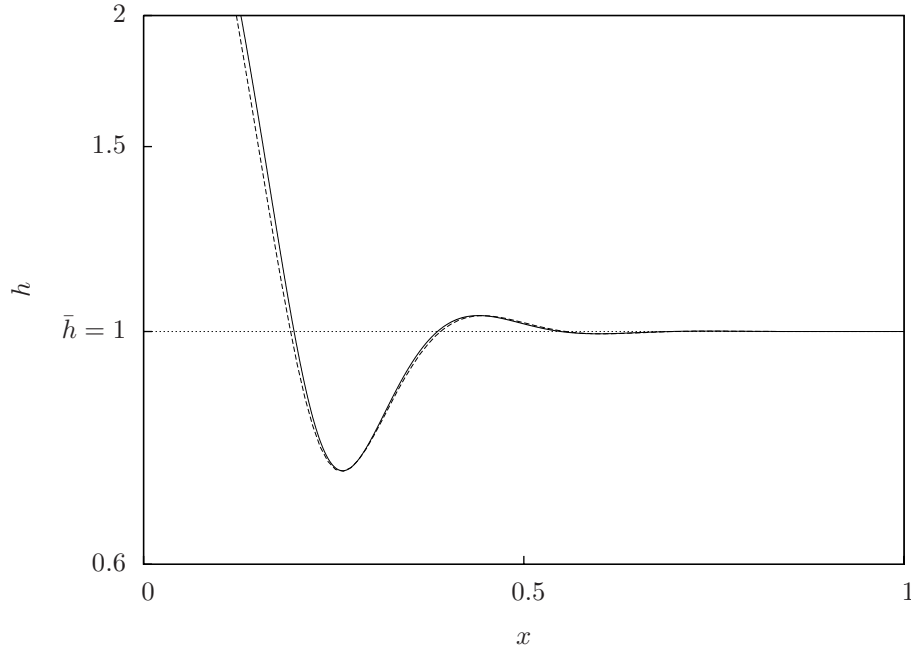


FIGURE 2.2: The kernel of the linearized film equation (dashed) plotted along side a scaled simulation of the fourth-order equation (solid). Note the logarithmic scale in h .

We suppose $s = s_0 + s_1 + s_2 + \dots$ with $s_0 \gg s_1 \gg s_2 \gg \dots$. Making the assumption $s'_0 \gg s'''_0$ results in the dominant balance

$$\eta/4 = (s'_0)^3 \quad (2.23)$$

with

$$s_0 = -\frac{3}{2^{1/3}}(1 \pm i\sqrt{3})\eta^{4/3}, \quad (2.24)$$

where we have discarded the third solution as it is exponentially growing. At next order we obtain the balance

$$\eta^{1/3} + 3\eta^{2/3}s'_1 = 0 \quad (2.25)$$

with

$$s_1 = -\frac{1}{3}\ln(\eta), \quad (2.26)$$

the first non-exponential term in Ψ . The leading order approximation to the kernel is

$$\Psi \sim \eta^{-1/3} \exp\left(-\frac{3}{2}\left(\frac{\eta}{4}\right)^{4/3}\right) \left[\cos\left(\frac{3\sqrt{3}}{2}\left(\frac{\eta}{4}\right)^{4/3}\right) + \sin\left(\frac{3\sqrt{3}}{2}\left(\frac{\eta}{4}\right)^{4/3}\right) \right]. \quad (2.27)$$

This expansion shows the kernel of the fourth-order heat equation decaying, but also oscillating as shown in Fig. 2.2. Note that (2.27) diverges as $x \rightarrow 0$, though this is not shown in the figure. The oscillations preclude a maximum principle for the equation. Without a maximum principle, there is no guaranteed lower bound on the solution, and so merely adding an $O(\delta)$ wetting layer is insufficient to guard against rupture [5]. We will include additional physics to guarantee the prewetting layer keeps $h > 0$ in the next section.

2.3 Intermolecular forces

Thin layers of viscous fluids on hydrophobic solid substrates experience instabilities that drive flat films to dewet into collections of droplets. These instabilities are tied to intermolecular forces between the fluid and the substrate [14, 68, 52] causing perturbations in the film to deepen [81, 78] and grow into holes. Subsequently, the fluid reassembles into localized droplets [6]. In many problems other short-range forces produce an ultra-thin film (UTF) adsorbed on the substrate, and the drops sit on top of this fluid layer. This adsorbed layer acts as the prewetting layer above, but due to the addition of intermolecular forces, the behavior of the linearized lubrication model for small h is bounded below. These forces are occasionally applied even when they are unphysical as a regularization. They may be arrived at through a diffuse interface formulation of the equations [71], and this formality can be used to justify their presence. However, this work is concerned with a physical situation where these forces are fully physical and fundamental to the dynamics we will study.

We model these forces by inserting a contribution to the pressure in (2.11) through the force ϕ . In dimensional form, this is

$$p = -\sigma\partial_{xx}h + \Pi(h) + \rho gh, \quad (2.28)$$

where γ is the fluid's surface tension, ρ the density, and g is the acceleration due to gravity. The disjoining pressure $\Pi(h)$ models the intermolecular forces, and we choose to use the form

$$\Pi(h) = \frac{A}{h^3} \left[1 - \frac{h_{\text{UTF}}}{h} \right], \quad (2.29)$$

for the disjoining/conjoining intermolecular forces [25, 24, 52, 51, 48, 46, 62, 61], where h_{UTF} sets the approximate height of the adsorbed ultra-thin film and A is the Hamaker constant. Other forms for $\Pi(h)$ have been proposed [65, 71, 16], and results are qualitatively similar provided the potential still contains a single minimum near h_{UTF} .

With the addition of these forces, the non-dimensionalization of (2.11) must be revisited to account for the scale separation between very thin heights where $\Pi(h)$ is important and thicker heights where it is not. We introduce scales

$$h = H\hat{h}, \quad x = L\hat{x}, \quad t = T\hat{t}, \quad h_{\text{UTF}} = H\delta, \quad (2.30)$$

where δ represents the height of the UTF relative to a typical film height,

$$\delta = (h_{\text{UTF}}/H) < 1. \quad (2.31)$$

Typically, we consider $\delta \ll 1$. We choose the lengthscale to balance the influence of surface tension and the disjoining pressure, $L = H\sqrt{\Xi}$, where Ξ is the dimensionless ratio

$$\Xi = \gamma h_{\text{UTF}}^2 / A. \quad (2.32)$$

Lengthscale L is comparable to the *healing length* [37] and [15, Chap 4], also called the cicatrization length [43], and we will refer to Ξ as a healing parameter. It is

the appropriate scale for describing small droplets and other structures produced by spinodal dewetting, typically $L = O(\mu\text{m})$.

The time scales with the viscosity, $T = 3\mu H \Xi^2 / \gamma \approx 10^{-2}$ s. Dropping the hats for convenience, we obtain the dimensionless equation

$$\frac{\partial h}{\partial t} = \frac{\partial}{\partial x} \left(h^3 \frac{\partial}{\partial x} \left[f(h) - \frac{\partial^2 h}{\partial x^2} + \alpha h \right] \right). \quad (2.33)$$

The function $f(h)$ is the non-dimensional form of Π ,

$$f(h) = \frac{\delta^2}{h^3} \left[1 - \frac{\delta}{h} \right], \quad (2.34)$$

where the factor of δ^2 is included so that the apparent contact angle of the resulting partially wetting drops is fixed in the limit $\delta \rightarrow 0$ [22, 24], a fact we will verify in Chapter 3.

The only remaining parameter in equation (2.33) is the ratio of the influence of gravity compared with the disjoining pressure, which can be expressed as

$$\alpha = \frac{\rho g H^4 \delta^2}{A} = \frac{\rho g H^2 \Xi}{\gamma} = (H/\ell_c)^2 \Xi. \quad (2.35)$$

The capillary length, $\ell_c = \sqrt{\sigma/(\rho g)}$, is the ratio of surface tension to gravitational force and is the lengthscale over which drops deform from spherical caps to puddles (see Fig. 3.1). The size of α depends strongly on the film thickness scale H . We will consider both $\alpha = 0$ and $\alpha = O(1)$ in this thesis, corresponding to small and large drops respectively.

It is convenient to combine the effects of gravitational hydrostatic pressure, αh , and intermolecular forces, $f(h)$, into one *generalized wetting potential* $U(h)$,

$$U(h) = -\frac{\delta^2}{h^2} \left(\frac{1}{2} - \frac{\delta}{3h} \right) + \frac{1}{2} \alpha h^2. \quad (2.36)$$

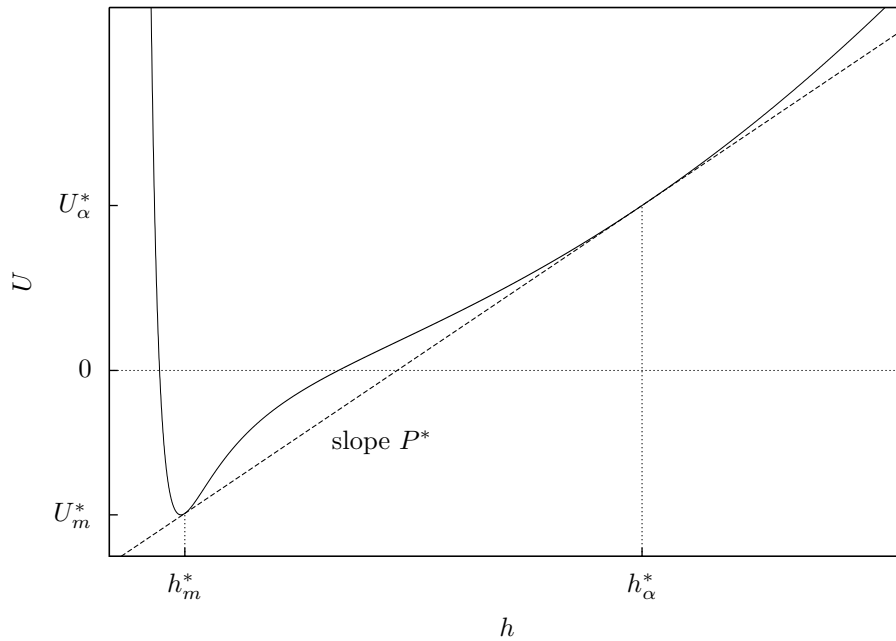


FIGURE 2.3: The generalized wetting potential $U(h)$, incorporating contributions for both intermolecular forces and gravitational forces. The dashed line shows the double tangent of slope P^* meeting the potential at values h_m^* and h_α^* .

shown in Fig. 2.3 with

$$U'(h) = f(h) + \alpha h, \quad (2.37)$$

shown in Fig. 3.2. The final form of the dimensionless pressure is

$$p = -\partial_{xx}h + U'(h), \quad (2.38)$$

the mass flux is

$$J \equiv -h^3 \partial_x p, \quad (2.39)$$

and the governing PDE may be written as

$$\partial_t h = \partial_x (h^3 \partial_x [-\partial_x^2 h + U'(h)]). \quad (2.40)$$

The wetting potential is a non-convex, double-welled potential and correspondingly $U'(h)$ is non-monotone. Similar potentials have been considered by others

[48, 46, 71, 65]. This form of the potential has a local maximum in the first derivative, $U'(h_{\text{peak}}) = p_{\text{max}}$, where for $\delta \rightarrow 0$,

$$h_{\text{peak}} = \frac{4}{3}\delta + \frac{1024}{729}\alpha\delta^3 + O(\delta^7) \quad (2.41a)$$

$$p_{\text{max}} = \frac{27}{256}\delta^{-1} - \frac{512}{729}\alpha^2\delta^3 + O(\delta^5). \quad (2.41b)$$

The potential also has a local minimum in its derivative, $U'(h_{\text{node}}) = p_{\text{node}}$, where

$$h_{\text{node}} = \left(\frac{3}{\alpha}\right)^{1/4} \delta^{1/2} - \frac{1}{3}\delta + O(\delta^{7/2}) \quad (2.42a)$$

$$p_{\text{node}} = \left(\frac{\alpha}{3}\right)^{3/4} \delta^{1/2} + \left(\frac{\alpha}{3}\right)^{5/4} \left(\frac{\sqrt{\alpha}}{3} - 1\right) \delta^{3/2} + O(\delta^2) \quad (2.42b)$$

In addition, there is a double tangent to $U(h)$, touching the curve at h_m^* and h_α^* . Geometrically, these are related by

$$\begin{aligned} P^*(h_\alpha^* - h_m^*) &= U(h_\alpha^*) - U(h_m^*) \\ U'(h_m^*) &= U'(h_\alpha^*) = P^*, \end{aligned} \quad (2.43)$$

where P^* is the slope of the tangent. This has approximate solution

$$\begin{aligned} P^* &= \sqrt{\alpha/3} + \delta\alpha + O(\delta^2), \\ h_m^* &= \delta + \delta^2\sqrt{\alpha/3} + \delta^3\frac{4}{3}\alpha + O(\delta^4), \\ h_\alpha^* &= (3\alpha)^{-1/2} + \delta + O(\delta^2). \end{aligned} \quad (2.44)$$

The structure of the potential remains the same ($p_{\text{node}} < p_{\text{max}}$) so long as $\alpha \ll \delta^{-2}$, a condition that corresponds to the usual scale of forces in experiments. This provides a large upper bound on α . For $\alpha \rightarrow 0$, we have $h_{\text{node}} \rightarrow \infty$, $P^* \rightarrow 0$, $h_{\text{peak}} = 4\delta/3$, and $p_{\text{max}} = 27/(256\delta)$. The case of $\alpha < 0$, corresponding to hanging drops, would be an interesting extension of this work, but will not be considered.

Equation (2.40) may be viewed as a version of the Cahn-Hilliard equation for phase separation [47, 48], and the double-welled potential shares many features with

potentials typically considered in that context. Bray [9] reviews coarsening problems associated with the Cahn-Hilliard model.

2.4 Uniform film instabilities

Including intermolecular forces causes instabilities that are generally classified into two types. The first, spinodal dewetting, is a global instability. Equation (2.40) is a form of the Cahn-Hilliard equation, modeling phase separation between two energetically favorable states [8]. Spinodal dewetting is the direct analog of spinodal decomposition [29, 7, 52], with the preferred states being droplets and the UTF. A second type of instability is known as nucleation dewetting and occurs when a finite sized perturbation allows a nominally stable uniform film to evolve to a stable, lower-energy state [70, 64, 16]. Dewetting has been studied by many authors both theoretically [78, 81, 52, 79], and experimentally [58, 59, 29, 7, 63]. We review the basic result of spinodal dewetting, but do not discuss nucleation dewetting.

Spinodal dewetting can be seen through a linear instability analysis. Assuming $h = \bar{h} + \varepsilon \tilde{h}(x, t)$, we obtain at leading order

$$\partial_t \tilde{h} + \bar{h}^3 [U''(\bar{h}) \partial_{xx} \tilde{h} - \partial_{xxxx} \tilde{h}] = 0. \quad (2.45)$$

Inserting $\tilde{h}(x, t) = \exp(\lambda t + ikx)$ gives the dispersion relation

$$\lambda = -\bar{h}^3 k^2 [k^2 + U''(\bar{h})]. \quad (2.46)$$

Figure 2.4 shows this dispersion relation for $\bar{h} = 0.25$, $\delta = 0.1$ and $\alpha = 1$. There is a critical wave number

$$k_c = \sqrt{-U''(\bar{h})} \quad (2.47)$$

marking the boundary between growing and decaying modes. The fastest growing mode is given by $k_{\max} = k_c / \sqrt{2} > 0$, and is consistent with a pattern forming

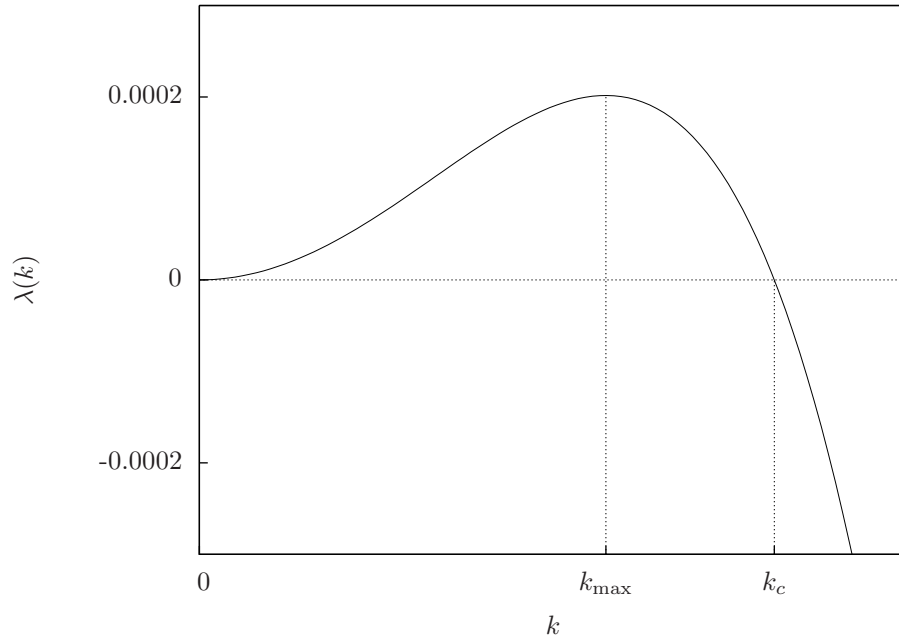


FIGURE 2.4: The dispersion relation for spinodal dewetting.

instability [71]. Diez and Kondic show that the spacing between drops resulting from spinodal dewetting is almost exactly $1/k_{\max}$ [16]. The critical wave number k_c is only defined when $U''(\bar{h}) < 0$. This occurs between the two extrema of $U'(h)$, $h_{\text{peak}} < \bar{h} < h_{\text{node}}$, see Fig. 2.5. For $\bar{h} > h_{\text{node}}$, the uniform film is linearly stable. The fact that $h_{\text{node}} \rightarrow \infty$ as $\alpha \rightarrow 0$ forces even very thick films to be unstable. It is the finite influence of gravity that limits the height range for spinodal dewetting.

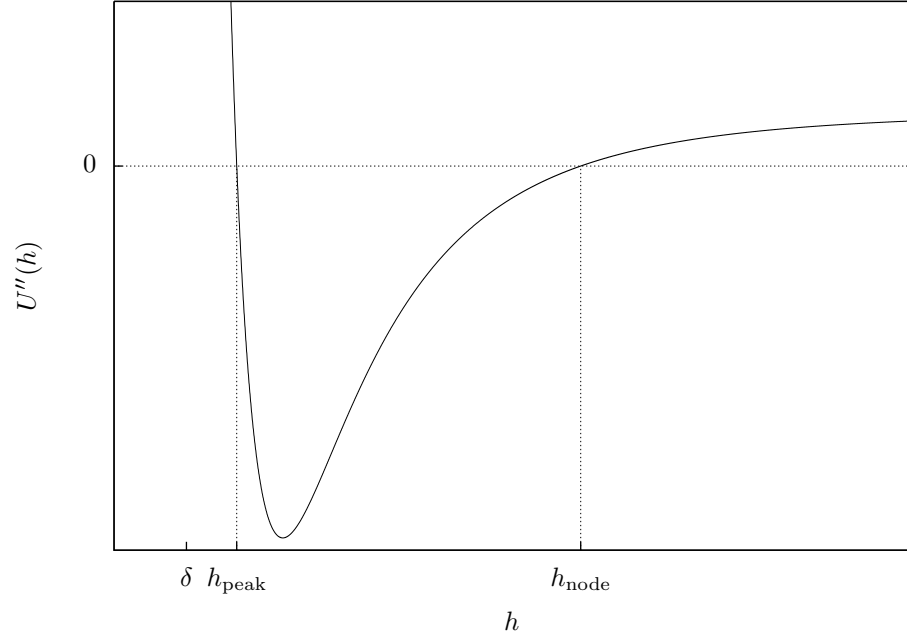


FIGURE 2.5: The second derivative of the wetting potential $U''(h)$ for $\alpha = 0.5$ and $\delta = 0.1$.

Steady-state droplet solutions

For partially wetting fluid/substrate systems ($U(h) \neq 0$), there exist stable droplet-type steady-states of the thin film equation. These states exhibit a fixed contact angle determined by the physio-chemical properties of the system and a nonzero height UTF outside of their essential support. Both of these properties depend on $U(h)$. In this chapter we first develop a phase plane description followed by an asymptotic description of these solutions and their properties, especially in the limit of large drops (see Fig. 3.1). These solutions have been observed by others, see [14, Sec. D2] and [15, 6, 71, 26].

3.1 Phase plane description of bounded solutions

The lubrication equation (2.40) has a monotone decreasing energy functional,

$$E = \int U(h) + \frac{1}{2}(\partial_x h)^2 dx, \quad \Rightarrow \quad \frac{dE}{dt} = - \int h^3(\partial_x p)^2 dx \leq 0. \quad (3.1)$$

Nontrivial equilibria are stationary points of the energy and must have constant pressure, $p(x, t) \equiv P$. Alternatively, the flux $J = -h^3\partial_x p$ is zero at steady-state; this

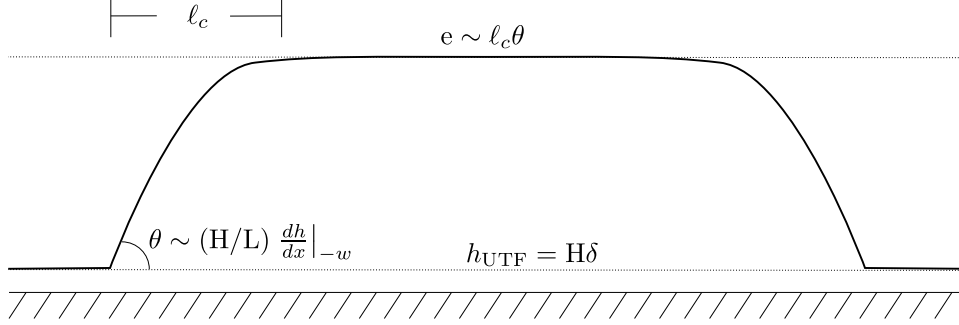


FIGURE 3.1: A schematic of a large thin film droplet showing the puddle height e (3.28), the contact angle θ (3.20), and the capillary length ℓ_c .

is also achieved by having a constant pressure. Note that physical solutions do not exist for $h = 0$, though a zero height film everywhere is technically a steady-state solution.

Steady state solutions are then given by the differential equation

$$\frac{d^2 h}{dx^2} = U'(h) - P. \quad (3.2)$$

Multiplying through by $\partial_x h$ and integrating gives the first integral

$$\frac{1}{2} \left(\frac{dh}{dx} \right)^2 = U(h) - Ph + C. \quad (3.3)$$

Choosing the constant of integration C selects a contour in the (h, h') phase plane. Equation (3.2) has at most three fixed points, $\{h_m, h_c, h_\alpha\}$, given by the roots of

$$U'(h) = P, \quad (3.4)$$

see Fig. 3.2. For the potential (2.36) these fixed points for $\delta \rightarrow 0$ are approximated by

$$h_m = \delta + \delta^2 P + \delta^3 (4P^2 - \alpha) + O(\delta^4), \quad (3.5a)$$

$$h_c = \frac{1}{P^{1/3}} \delta^{2/3} - \frac{1}{3} \delta + \delta^{4/3} \left(\frac{2}{9} P^{1/3} - \frac{\alpha}{3P^{5/3}} \right) + O(\delta^{5/3}), \quad (3.5b)$$

$$h_\alpha = \frac{P}{\alpha} + O(\delta^2). \quad (3.5c)$$

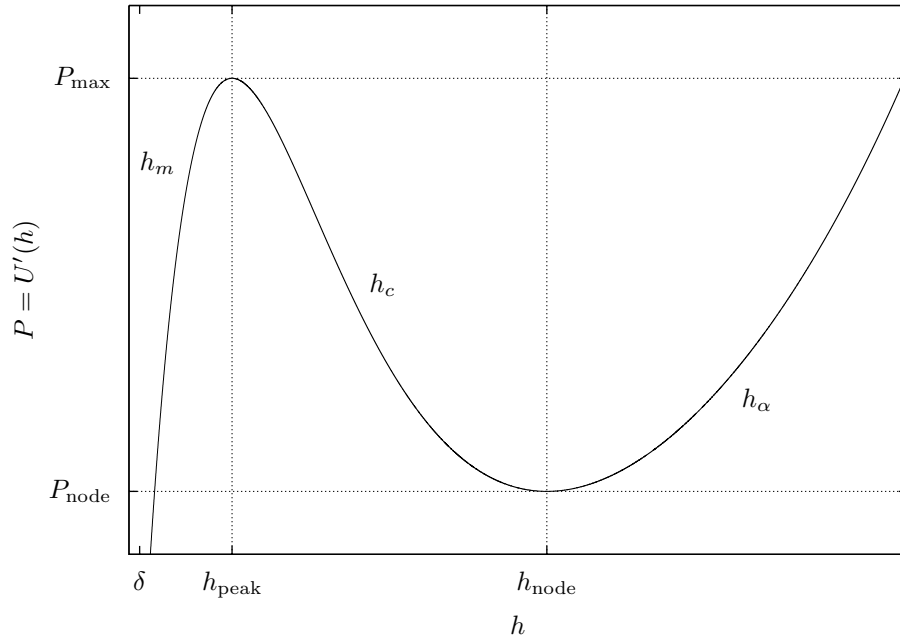


FIGURE 3.2: The fixed points (3.5) of (3.2) as determined from the wetting potential. Dotted lines separate the three branches of fixed points $\{h_m, h_c, h_\alpha\}$. Note h is plotted on a logarithmic scale.

Fixed points h_c and h_α depend on the pressure at leading order while the nominal UTF thickness, h_m , has a weaker dependence. Linearizing about these fixed points gives eigenvalues of $\lambda \pm \sqrt{U''(h)}$ and corresponding eigenvectors $(\pm\sqrt{U''(h)}, 1)^T$. At h_m and h_α , $U'' > 0$, making each of these points saddles. For h_c , $U''(h_c) < 0$, making it a center.

Non-periodic bounded-in-height solutions must originate and terminate at a saddle point, orbiting h_c once in the process. Figure 3.2 shows that there is a saddle-node bifurcation at P_{\max} and at P_{node} (see also Fig. 3.7). Each of these bifurcations destroys a saddle and a center, leaving only a single saddle (h_α or h_m , respectively) in the phase plane. Without a center, solutions are no longer bounded in height.

For $P_{\text{node}} < P < P_{\max}$, there are three possible bounded-in-height solutions: a homoclinic orbit through h_m for $P^* < P < P_{\max}$, a homoclinic orbit through h_α

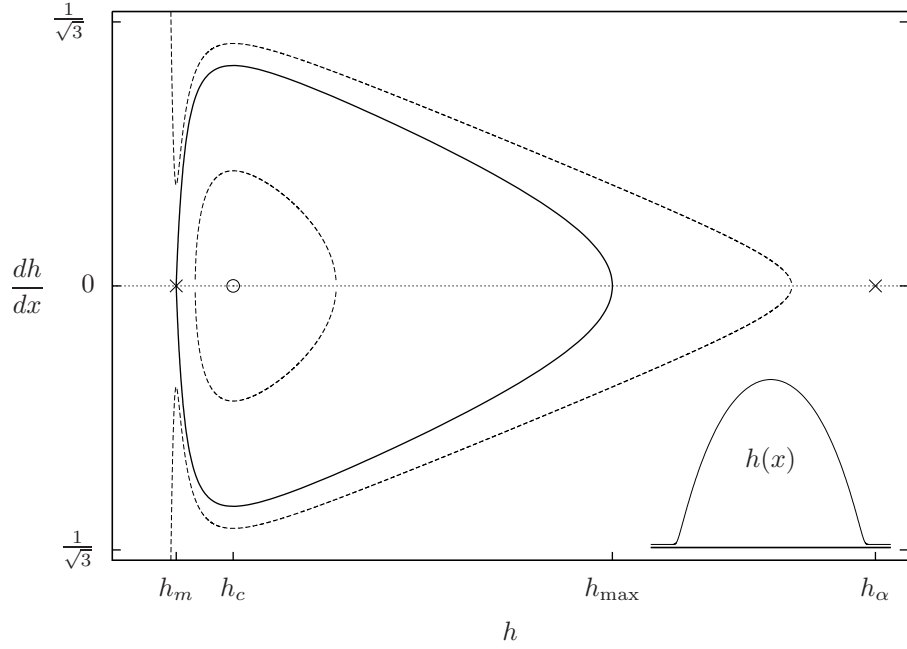


FIGURE 3.3: The phase plane for a small droplet-type solution, $P^* \ll P < P_{\max}$. The inset shows the parabolic drop profile $h(x)$ corresponding to the homoclinic orbit.

for $P_{\text{node}} < P < P^*$, or a heteroclinic orbit from h_m to h_α for $P = P^*$. The orbit homoclinic to h_m is given by choosing $C = Ph_m - U(h_m)$ in (3.3) so that

$$\frac{dh}{dx} = \pm r(h; P) = \pm \sqrt{2[U(h) - U(h_m) + P(h - h_m)]}. \quad (3.6)$$

This orbit has a zero of $r(h; P)$ corresponding to the maximum of h , h_{\max} , given by

$$U(h_{\max}) - U(h_m) = P(h_{\max} - h_m), \quad (3.7)$$

and approximately

$$h_{\max} = \frac{1}{\alpha}(P - \sqrt{P^2 - \alpha/3}) + \delta P(P^2 - \alpha/3)^{-1/2} + O(\delta^2). \quad (3.8)$$

Notice that

$$\lim_{\alpha \rightarrow 0} h_{\max} = \frac{1}{6P}. \quad (3.9)$$

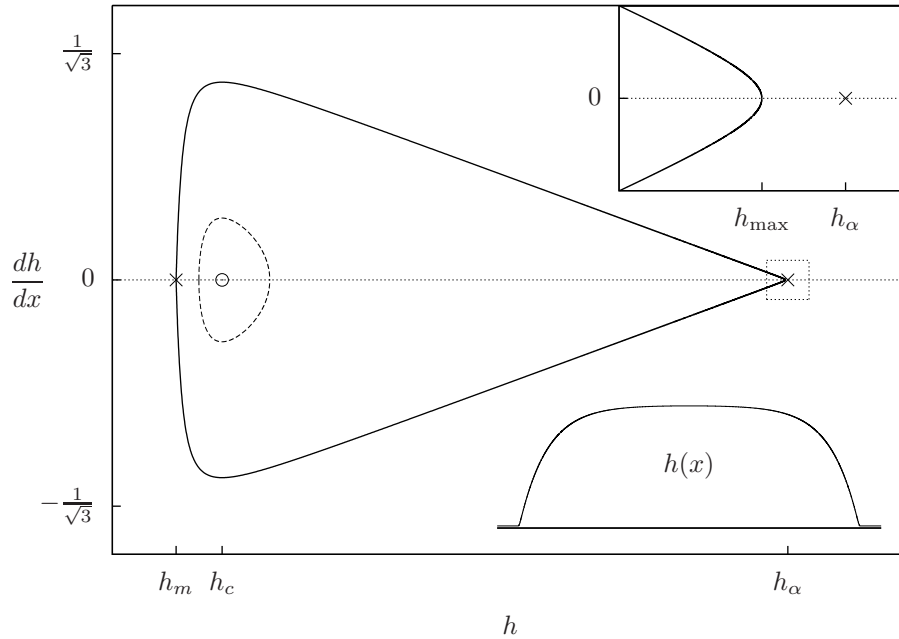


FIGURE 3.4: A large drop ($P \gtrsim P^*$) phase plane. Note that the homoclinic orbit passes through h_m and very near h_α (see top inset). The bottom inset shows the corresponding mesa-like drop profile $h(x)$.

These orbits correspond to droplet-type solutions with an UTF layer height of h_m and are the most physically relevant, see Figs. 3.3 and 3.4. As $P \rightarrow P^*$, the droplet grows larger and flattens in height.

Orbits homoclinic to h_α are given by

$$\frac{dh}{dx} = \pm r(h; P) = \pm \sqrt{2[U(h) - U(h_\alpha) + P(h - h_\alpha)]}. \quad (3.10)$$

Analogous to the drop-type orbits, these have a local minimum, a dimple of height h_{dim} , given by

$$U(h_{\text{dim}}) - U(h_\alpha) = P(h_{\text{dim}} - h_\alpha), \quad (3.11)$$

and for $\delta \rightarrow 0$,

$$h_{\text{dim}} = \delta \left(\frac{\zeta(\alpha, P)}{6P} + \frac{2\alpha}{P\zeta(\alpha, P)} \right) + O(\delta^2), \quad (3.12)$$

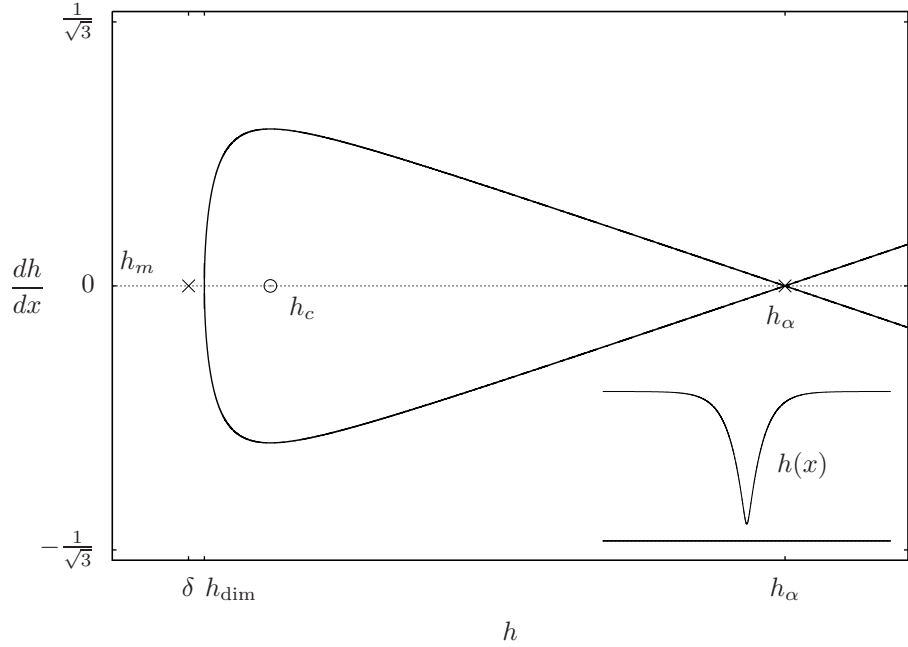


FIGURE 3.5: The phase plane for a dimple-type solution. The inset shows the profile $h(x)$.

where $\zeta = [12\alpha (\sqrt{9P^2 - 12\alpha} - 3P)]^{1/3}$. See Fig. 3.5 for the shape of the solution. As $P \rightarrow P^*$, the minimum height shrinks to become $O(\delta)$.

Finally, at the bifurcation value P^* , the heteroclinic orbit approaches h_α for $x \rightarrow \infty$ and h_m for $x \rightarrow -\infty$ (or vice versa). This half-infinite drop (see Fig. 3.6) has $h_{\max} = h_\alpha$ and $h_{\dim} = h_m$, the starred values given in (2.43).

Geometrically, a line of slope P is tangent to $U(h)$ at a saddle and intersects $U(h)$ at the local extremum. A droplet-type solution has the line tangent at h_m and intersecting at h_{\max} , while a dimple-type solution has a tangent at h_α and an intersection at h_{\dim} . The heteroclinic orbit corresponds to the double tangent at h_m^* and h_α^* . This is similar to the double tangent construction shown in [15, Fig. 7.3] and [46].

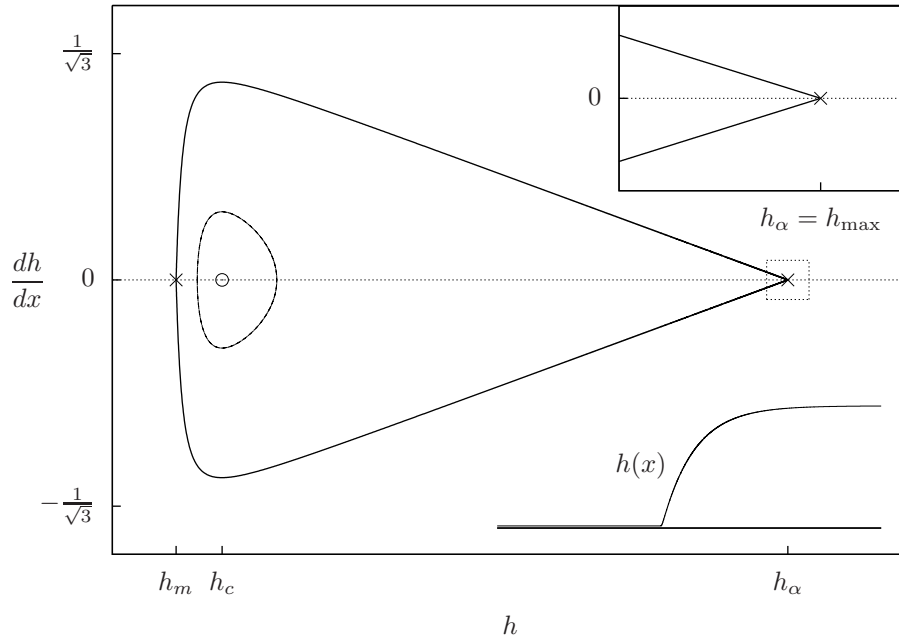


FIGURE 3.6: Phase plane for the heteroclinic solution with $P = P^*$. The inset shows the corresponding step-up profile $h(x)$.

3.2 Asymptotic description of drop solutions

We now focus on the more interesting droplet-type solutions and develop an asymptotic description of these solutions and their properties.

Two basic drop properties, the mass and width, may be found by integrating in the phase plane using $\frac{dh}{dx} = r(h; P)$ (3.3). The drop mass m , or volume, may be found by

$$m(P) = 2 \int_{-\infty}^{\infty} (h - h_m) dx = 2 \int_{h_m}^{h_{\max}} \frac{h - h_m}{r(h; P)} dh, \quad (3.13)$$

where we subtract the UTF contribution so that the integral is finite. To define an effective droplet width we use the position where $h = h_{\text{peak}}$; this value corresponds to the maximum of $U'(h)$ gives an effective dividing line between the edge of the

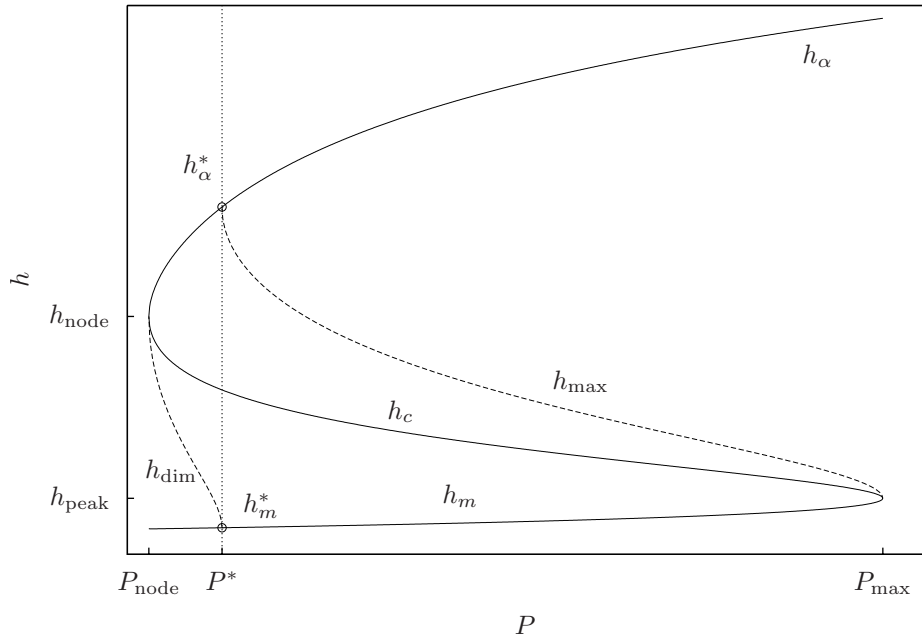


FIGURE 3.7: The bifurcation diagram for fixed points $\{h_m, h_c, h_\alpha\}$ of (3.2), shown as solid curves. The dashed curve shows the value of h_{\max} for $P > P^*$ and h_{\dim} for $P < P^*$. Note h is plotted on a log scale. Droplet solutions exist for $P^* < P < P_{\max}$.

droplet core and the outer UTF [6], leading to the expression for the width:

$$w(P) = \int_{h_{\text{peak}}}^{h_{\text{max}}} \frac{1}{r(h; P)} dh. \quad (3.14)$$

In general, m and w must be found numerically. For the two special cases of large and small drops, we can additionally describe these drop properties through asymptotic expressions.

3.2.1 Drops with no gravitational influence

The case of small drops, given by the $\alpha \rightarrow 0$ limit, is identical to the analysis in [24, 25]: (i) the lower bound on pressures goes to zero, $P^* \rightarrow 0$ and (ii) the upper bound on heights diverges, $h_\alpha \rightarrow \infty$. The structure of the solution can be described asymptotically as an outer solution for the drop core $h = O(1)$ and an $O(\delta)$ boundary

layer to match to h_m . In the outer solution, the $U'(h)$ term is neglected in (3.2) and the remainder may be integrated to obtain

$$h \sim \frac{1}{2}P(w^2 - x^2) \quad \text{for } |x| < w, \quad (3.15)$$

where we have imposed $h(w) = 0$ and $h'(0) = 0$ so that the drop is localized inside width w and is symmetrical. Matching this solution to h_{\max} (3.9) gives

$$w \sim 1/(\sqrt{3}P). \quad (3.16)$$

The mass of a drop is approximately the integral of (3.15)

$$m \sim \frac{\sqrt{3}}{27}P^{-2}. \quad (3.17)$$

The boundary layer occurs on a scale of $H = \delta\hat{h}$ and $x = -w + \delta z$. Although the equation is still nonlinear at leading order, the structure may be gleaned from $r(H; P)$. As $H \rightarrow h_m/\delta$, $r \rightarrow 0$, so the solution flattens into the UTF. In the limit $H \rightarrow \infty$,

$$r \sim \sqrt{-H^{-2} + \frac{2}{3}H^{-3} + 1/3 + O(\delta)} \rightarrow 1/\sqrt{3}. \quad (3.18)$$

This matches the outer solution $\hat{h}_x(w) = wP = 1/\sqrt{3}$, in agreement with (3.16).

The approximation (3.15) holds for the related limits $\alpha \rightarrow 0$, $P \rightarrow P_{\max}$, or $m \rightarrow 0$. This can be seen from the form of h_α , where we expect that when $\alpha > 0$ but P is large, solutions will resemble (3.15). By examining (3.8) we deduce that the regime of small droplets in (3.2) can be defined by the condition

$$P \gg \sqrt{\alpha} \quad \text{or} \quad \frac{1}{m} \gg \alpha. \quad (3.19)$$

As expected, gravity has a weaker influence than surface tension and the disjoining pressure for small droplets. Hence (3.15) remains a good description of droplets with pressures in the range $\sqrt{\alpha} \ll P \leq P_{\max}$, see Figs. 3.3 and 3.4.

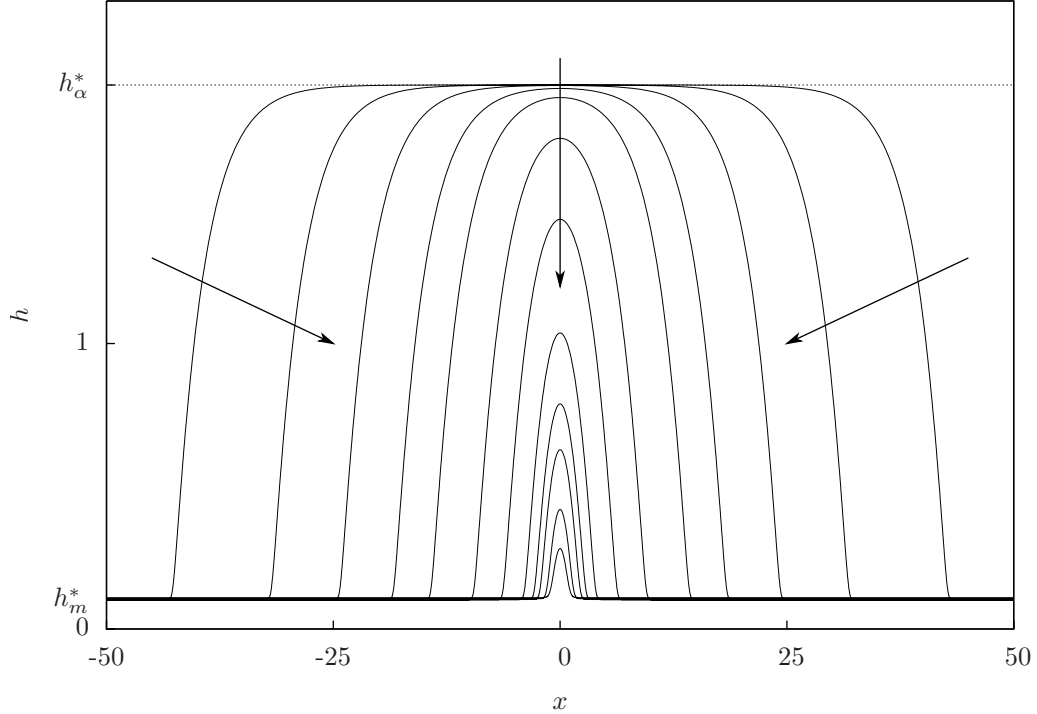


FIGURE 3.8: Drop profiles for $\alpha = 0.1$ and different pressures $P^* < P < P_{\max}$. The arrows show the trend for increasing pressure.

3.2.2 Drops with shapes modified by gravity

Our focus turns to the structure of very large drops, where gravity comes into play. Droplets of arbitrarily large masses are possible, the definition of large vs. small masses has to be given relative to α , see (3.19). Since their height is strictly bounded by h_α^* , they take the form of wide, flat “mesas,” “pancakes,” or “puddles” [28, 15, 10] see Fig. 3.4. In this context, we will find it more convenient to distinguish drops as being parabolic or mesa-like, rather than large or small. For mesa-like drops, the homoclinic orbit passes very near the h_α saddle point resulting in a long region where the height is nearly constant. Note that $h_\alpha > h_{\text{node}}$, so locally, the cores of mesa drops are in the linearly stable range of film heights.

Figure 3.8 shows the family of drops at a fixed value of α with the pressure being

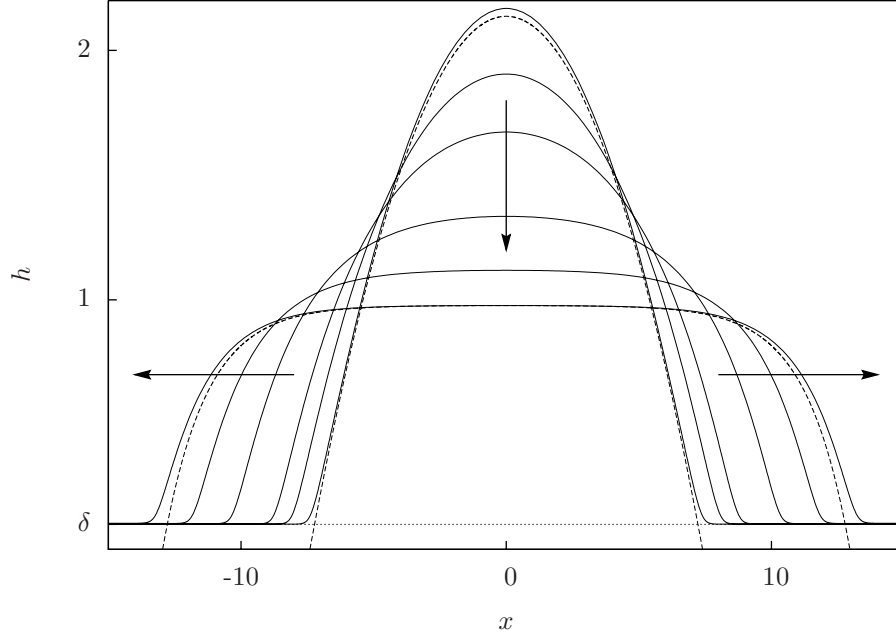


FIGURE 3.9: Drop profiles for mass $m = 20$ and $0 \leq \alpha \leq 0.4$. The arrows show the direction of increasing α . The dashed profiles are the asymptotic approximations to the $\alpha = 0$ and the $\alpha = 0.4$ drops from (3.15) and (3.23) respectively.

increased over the range $P^* < P < P_{\max}$. Larger drops ($P \rightarrow P^*$) have $h_{\max} \approx h_{\alpha}^*$ and a mesa-like shape, while smaller drops ($P \rightarrow P_{\max}$) approach a more parabolic structure. Figure 3.9 shows a series of drop profiles with mass fixed as the relative influence of gravity is increased. The contact angle for our drops in the small mass limit is given analytically by (3.18) as $\tan \theta \sim (H/L) \left. \frac{dh}{dx} \right|_{-w} \sim \sqrt{A/(3\gamma h_{\text{UTF}}^2)}$, yielding the fixed angle

$$\theta \sim 1/\sqrt{3\Xi}. \quad (3.20)$$

This angle is independent of δ through the scaling of (2.34). As can be seen from Figs. 3.8 and 3.9, the contact angle of drops is also independent of gravity. Physically, the contact angle is determined by a balance of surface tension and disjoining pressure at the contact line, where other forces are small, and this is consistent with (3.20).

The structure of large drops is most easily examined by considering the $P \rightarrow P^*$

limit. Some droplet properties can be obtained as regular perturbation expansions,

$$\begin{aligned}
h_m &= h_m^* + \frac{P - P^*}{U''(h_m^*)} + O([P - P^*]^2), \\
h_\alpha &= h_\alpha^* + \frac{P - P^*}{U''(h_\alpha^*)} + O([P - P^*]^2), \\
h_{\max} &= h_\alpha^* - \beta^* \sqrt{P - P^*} + O(P - P^*),
\end{aligned} \tag{3.21}$$

where

$$\beta^* = \sqrt{\frac{2(h_\alpha^* - h_m^*)}{U''(h_\alpha^*)}} \sim \left(\frac{4}{3\alpha^3}\right)^{1/4}.$$

In this limit, the height profile approaches the heteroclinic trajectory connecting h_m^* to h_α^* , see Fig. 3.4. Comparing the eigenvalues of the two saddles, $\lambda = \pm\sqrt{U''(h)}$, of (3.2) reveals that $(\lambda_m^* \approx 1/\delta) \gg (\lambda_\alpha^* \approx \sqrt{\alpha})$, so the form of the solutions will be dominated by the behavior near h_α . Linearizing (3.2) about h_α gives

$$\frac{d^2 h}{dx^2} \sim U''(h_\alpha)(h - h_\alpha) \tag{3.22}$$

where we assume that $h_\alpha - h_{\max}$ is small. Solving this equation subject to $h(0) = h_{\max}$ and $h'(0) = 0$ gives

$$h \sim \left[h_\alpha - (h_\alpha - h_{\max}) \cosh \left(x \sqrt{U''(h_\alpha)} \right) \right]_+, \tag{3.23}$$

see Fig. 3.9. The edge of the region of support for this linearized solution gives a good estimate for the width of drops, $h = 0$ at

$$w = \frac{1}{\sqrt{U''(h_\alpha)}} \operatorname{arccosh} \left(\frac{h_\alpha}{h_\alpha - h_{\max}} \right), \tag{3.24}$$

while the detailed structure near the contact line involves further matched asymptotics [10]. The mass may be approximated by

$$\begin{aligned}
m &= \int_{-w}^w h(x) - h_m \, dx \\
&= 2 \left[h_\alpha w - \frac{h_\alpha - h_{\max}}{\sqrt{U''(h_\alpha)}} \sinh \left(w \sqrt{U''(h_\alpha)} \right) \right].
\end{aligned} \tag{3.25}$$

To explicitly describe the sensitive dependence of the drop mass and width on the pressure, it is convenient to define a new parameter, *log excess pressure*

$$Q = \ln(P - P^*), \tag{3.26}$$

with $Q \rightarrow -\infty$ corresponding to $P \rightarrow P^*$. Expanding w and m gives

$$w(Q) \sim \frac{1}{\lambda_\alpha^*} \ln \left(\frac{2h_\alpha^*}{\beta^*} \right) - \frac{Q}{2\lambda_\alpha^*}, \tag{3.27a}$$

and

$$m(Q) \sim \lambda_\alpha^* \beta^{*2} \ln \left(\frac{2h_\alpha^*}{\beta^*} \right) - \frac{2h_\alpha^*}{\lambda_\alpha^*} - \frac{1}{2} \lambda_\alpha^* \beta^{*2} Q \approx \frac{1}{\alpha \sqrt{3}} \left(-Q + \frac{1}{2} \ln \alpha \right). \tag{3.27b}$$

Figure 3.10 shows the numerically computed mass of drops as a function of pressure compared against the low-mass and high-mass limits, (3.17) and (3.27b) respectively.

The $Q \rightarrow -\infty$ limit corresponds to the heavy drops analyzed in [15, Ch. 2]. The global maximum height h_α^* may be related to the expression for the dimensional value of the puddle height of a drop with a small contact angle θ ,

$$e = 2\sqrt{\gamma/\rho g} \sin(\theta/2) \sim \ell_c \theta, \tag{3.28}$$

where $\ell_c = \sqrt{\sigma/(\rho g)}$ is the capillary length. Using (2.44) for h_α^* with (3.20) and (2.35) yields

$$\text{H} h_\alpha^* \sim \frac{\text{H}}{\sqrt{3\Xi(\text{H}/\ell_c)^2}} = \ell_c \theta, \tag{3.29}$$

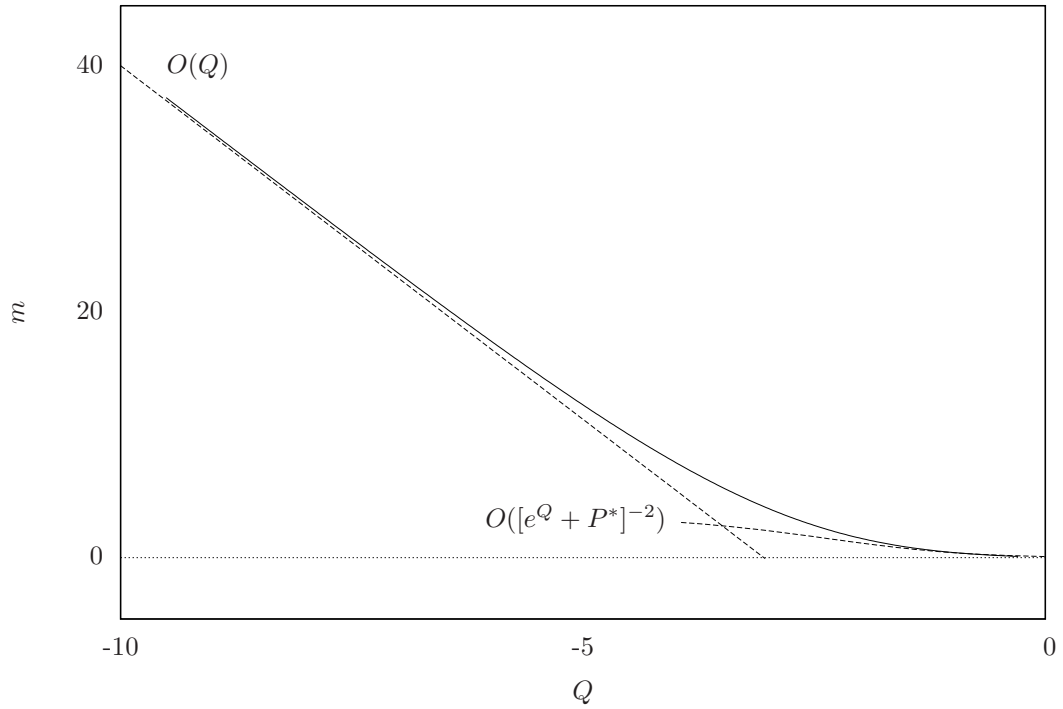


FIGURE 3.10: The m to Q relationship for $\alpha = 0.1$. Dashed lines show the estimates (3.27b) for large drops and (3.17) for small drops.

corresponding exactly with e showing that our analysis is consistent with the previous studies of large equilibrium drops (see also Fig. 3.8 and Fig. 3.1).

Returning to our analysis, we see that by combining (3.27b) with (3.19), a drop is well-approximated by the pancake profile (3.23) when its *mesa parameter* is large,

$$\mathbb{M} \equiv m\alpha \gg 1. \tag{3.30}$$

This condition provides an effective dividing line between parabolic and mesa drop behaviors that will be useful later.

Coarsening dynamical system model

Following the break-up of an unstable uniform film into an array of droplets (Section 2.4), the drop array continues to evolve. Laugesen and Pugh [36] show that the only steady state of (2.40) with no-flux boundary conditions is a single drop with its maximum on the boundary, and so no drop array is a steady-state solution. The dynamics taking an array to a single drop occurs on timescales that are $O(\delta^3)$ due to the form of the flux (2.39) and the scale of the UTF separating drops. The film evidently evolves quasi-statically through a series of metastable states: N drops, $N - 1$ drops, and so on.

We describe the coarsening by deriving a reduced model for droplet interaction. Using the description of static drops from Chapter 3, we examine first how these drops change in response to small fluxes far away, and then how to compute the fluxes between drops caused by pressure differences. Together these allow us to reduce the PDE (2.40) to a pair of ordinary differential equations (ODEs) for each drop. The two coarsening modes — collision and collapse — both cause blow-up in the ODEs. We approximate these fast timescale events as instantaneous processes

that delete drops, and return to computing the ODEs for the remaining drops. We also review the scaling arguments of [25] that relate the details of the initial drop array to the dominant mode of coarsening.

This model was originally proposed by Glasner and Witelski [24]. It appears here in more detail.

4.1 Quasi-static model for a single drop with applied fluxes

Consider a static drop $\bar{h}(x; P)$ of the form (3.6) confined to $-L \leq x \leq L$, where $2L$ is larger than the width of the drop w . At each boundary there is an imposed a flux

$$J(-L) = J_-, \quad J(L) = J_+ \quad (4.1)$$

and $\partial_{xxx}h(-L) = \partial_{xxx}h(L) = 0$. Since the domain is finite, h is not an exact steady-state solution to (2.11), but is in quasi-equilibrium, experiencing influences through the boundary layer representing its ultra-thin film and changing shape from the steady-state drop profile at one P to another. We neglect the exponentially small changes to \bar{h} arising from the confinement to a finite domain and consider only the effect of the applied flux. Adopting a slow timescale, $\tau = \sigma t$, we seek a perturbation solution of the form

$$h(x, t) = \bar{h}(x - X(\tau); P(\tau)) + \sigma \hat{h}(x, \tau) + O(\sigma^2), \quad (4.2)$$

where X is the location of the center of the drop, P is the pressure, and both are functions of the slow time. Calculating the flux from (2.39) gives

$$\begin{aligned} J &= -h^3 p_x = \bar{h}^3 \frac{d}{dx} \left(U'(\bar{h}) - \frac{d^2 \bar{h}}{dx^2} \right) + \sigma \bar{h}^3 \frac{\partial}{\partial x} \left(U''(\bar{h}) \hat{h} + \frac{d^2 \hat{h}}{dx^2} \right) + O(\sigma^2) \\ &= 0 + \sigma \hat{J} + O(\sigma^2), \end{aligned} \quad (4.3)$$

so the fluxes must be $J_- = \sigma \hat{J}_-$ and $J_+ = \sigma \hat{J}_+$ for (4.2) to be consistent with the boundary conditions. Substituting the perturbation into (2.40), at order σ we obtain

$$-\partial_x \bar{h} \frac{dX}{d\tau} + \partial_p \bar{h} \frac{dP}{d\tau} = \mathcal{L} \hat{h}, \quad (4.4)$$

for the linear operator

$$\mathcal{L}y = \partial_x (\bar{h}^3 \partial_x [-\partial_{xx} y + U''(\bar{h})y]). \quad (4.5)$$

We want to find P and X by projecting the problem onto the proper basis of eigenfunctions. By the Fredholm Alternative, the perturbation solution (4.2) only exists if the right side of (4.4) is in the nullspace of the adjoint,

$$\mathcal{L}^* z = [U''(\bar{h}) - \partial_{xx}] (\partial_x (\bar{h}^3 \partial_x z)), \quad (4.6)$$

see [67]. The above has been formed using the formal (L_2) inner product on an infinite domain and hence has no boundary terms. In what remains, we will define and use the inner product on a bounded domain:

$$\langle u, v \rangle \equiv \int_{-L}^L uv \, dx.$$

A basis of eigenfunctions for the nullspace of \mathcal{L}^* is

$$\phi_1 = 1 \quad (4.7)$$

$$\phi_2 = \int_0^x \frac{\bar{h}(s) - h_m}{\bar{h}(s)^3} \, ds. \quad (4.8)$$

These functions correspond to the two symmetries of \bar{h} : translation in x and dilation through changing P , respectively. It is clear from the form of (4.6) that ϕ_1 is in the nullspace. To see that ϕ_2 is also in the nullspace, we compute

$$\begin{aligned} \mathcal{L}^* \phi_2 &= [U''(\bar{h}) - \partial_{xx}] \left(\partial_x \left(\bar{h}^3 \frac{\bar{h} - h_m}{\bar{h}^3} \right) \right) \\ &= \partial_x (U'(\bar{h}) - \partial_{xx} \bar{h}) \\ &= \partial_x P = 0. \end{aligned} \quad (4.9)$$

Under the finite domain inner product the boundary conditions cause the inner products of $\mathcal{L}\hat{h}$ with these ϕ_i functions to be nonzero. It is convenient assume that the essential support of the drop $[X - w, X + w]$ lines inside $[-L, L]$ so that integrals of \bar{h} may be re-written as

$$\int_{-L}^L \bar{h} dx = \int_{X-w}^{X+w} \bar{h} dx + h_m^2(L - 2w) + \text{EST}. \quad (4.10)$$

The exponentially small term (EST) is the contribution of the exponentially decaying boundary layer (3.18) and can be neglected. The other small term is $O(\delta^2 L)$. We will assume that

$$\delta^2 L \ll 1, \quad (4.11)$$

so that the effective domain size around a drop compared to the UTF height is not too large.

Calculating the inner product of (4.4) with ϕ_1 gives

$$\left\langle \phi_1, -\partial_x \bar{h} \frac{dX}{d\tau} + \partial_p \bar{h} \frac{dP}{d\tau} \right\rangle = \left\langle \phi_1, \mathcal{L}\hat{h} \right\rangle. \quad (4.12)$$

On the right side,

$$\begin{aligned} \left\langle \phi_1, \mathcal{L}\hat{h} \right\rangle &= \int_{-L}^L \partial_x (\bar{h}^3 \partial_x [-\partial_{xx} \hat{h} + U''(\bar{h}) \hat{h}]) dx \\ &= \left[\bar{h}^3 \partial_x \left(-\partial_x^2 \hat{h} + U''(\bar{h}) \hat{h} \right) \right]_{-L}^L \\ &= \hat{J}_+ - \hat{J}_-, \end{aligned} \quad (4.13)$$

where the flux (4.3) appears on the second line. On the left side,

$$\begin{aligned} \left\langle \phi_1, -\partial_x \bar{h} \frac{dX}{d\tau} + \partial_p \bar{h} \frac{dP}{d\tau} \right\rangle &= -\frac{dX}{d\tau} \int_{-L}^L \partial_x \bar{h} dx + \frac{dP}{d\tau} \int_{-L}^L \partial_p \bar{h} dx \\ &\sim \frac{dX}{d\tau} \int_{X-w}^{X+w} \partial_x \bar{h} dx + \frac{dP}{d\tau} \int_{-L}^L \partial_p \bar{h} dx \\ &\sim \frac{dP}{d\tau} \int_{-L}^L \partial_p \bar{h} dx, \end{aligned} \quad (4.14)$$

where we have restricted the first integral to one over the core of the drop as described above. Since the drop is symmetric on $(X - w, X + w)$, and $\partial_x \bar{h}$ is odd over the same interval, the integral vanishes. Thus we have

$$\begin{aligned} \frac{dP}{d\tau} &= \left[\int_{-L}^L \partial_p \bar{h} dx \right]^{-1} (\hat{J}_+ - \hat{J}_-) \\ &= C_p(P)(\hat{J}_+ - \hat{J}_-). \end{aligned} \quad (4.15)$$

The inner product of (4.4) with ϕ_2 is

$$\left\langle \phi_2, -\partial_x \bar{h} \frac{dX}{d\tau} + \partial_p \bar{h} \frac{dP}{d\tau} \right\rangle = \left\langle \phi_2, \mathcal{L}\hat{h} \right\rangle. \quad (4.16)$$

On the right side,

$$\begin{aligned} \left\langle \phi_2, \mathcal{L}\hat{h} \right\rangle &= \int_{-L}^L \mathcal{L}\hat{h} \left(\int_0^x \frac{\bar{h}(s) - h_m}{\bar{h}^3(s)} ds \right) dx \\ &= \left[\left(\int_0^x \frac{\bar{h} - h_m}{\bar{h}^3} ds \right) \bar{h}^3 \partial_x \left(-\partial_{xx} \hat{h} + U''(\bar{h}) \hat{h} \right) \right]_{-L}^L \\ &\quad - \int_{-L}^L (\bar{h} - h_m) \partial_x \left(-\partial_{xx} \hat{h} + U''(\bar{h}) \hat{h} \right) dx \\ &\sim \left(\int_X^{X+w} \frac{\bar{h} - h_m}{\bar{h}^3} dx \right) (\hat{J}_+ + \hat{J}_-) \\ &\quad - \int_{-L}^L (\bar{h} - h_m) \partial_x \left(-\partial_{xx} \hat{h} + U''(\bar{h}) \hat{h} \right) dx \end{aligned} \quad (4.17)$$

where we have integrated by parts on the second line and restricted the $(0, \pm L)$ integral domain to $(X, X \pm w)$ so that we could use a symmetry argument. The

remaining integral can be simplified using integration by parts again, giving

$$\begin{aligned}
\langle \phi_2, \mathcal{L}\hat{h} \rangle &= \left(\int_0^L \frac{\bar{h} - h_m}{\bar{h}^3} dx \right) (\hat{J}_+ + \hat{J}_-) - \left[\left(-\partial_{xx}\hat{h} + U''(\bar{h})\hat{h} \right) (\bar{h} - h_m) \right]_{-L}^L \\
&\quad + \int_{-L}^L \partial_x \bar{h} \left(-\partial_{xx}\hat{h} + U''(\bar{h})\hat{h} \right) dx \\
&\sim \left(\int_0^L \frac{\bar{h} - h_m}{\bar{h}^3} dx \right) (\hat{J}_+ + \hat{J}_-)
\end{aligned} \tag{4.18}$$

where we have assumed that \hat{h} is even over $(X - w, X + w)$ so the last integral is of an even function times an odd function ($\partial_x \bar{h}$) and vanishes. We have also assumed that $h(\pm L) \sim h_m$, so that the boundary term also vanishes. In addition, we have re-extended the integral on the flux term to $(0, L)$ for convenience. The left side of (4.16) is

$$\begin{aligned}
\left\langle \phi_2, -\partial_x \bar{h} \frac{dX}{d\tau} + \partial_p \bar{h} \frac{dP}{d\tau} \right\rangle &\sim \frac{dP}{d\tau} \int_{X-w}^{X+w} \partial_p \bar{h} \phi_2(x) dx \\
&\quad - \frac{dX}{d\tau} \left[\left(\bar{h} \int_0^x \frac{\bar{h} - h_m}{\bar{h}^3} ds \right)_{-L}^L - \int_{-L}^L \frac{\bar{h} - h_m}{\bar{h}^2} dx \right] \\
&\sim -2 \frac{dX}{d\tau} \left[h_m \int_0^L \frac{\bar{h} - h_m}{\bar{h}^3} - \frac{\bar{h} - h_m}{\bar{h}^2} dx \right],
\end{aligned} \tag{4.19}$$

where we have used the fact that ϕ_2 is an odd function (the integral of an even function) while $\partial_p \bar{h}$ is even to conclude that the first integral is zero. The result of (4.16) is

$$\begin{aligned}
\frac{dX}{d\tau} &= - \left[\frac{\int_{-L}^L \frac{\bar{h} - h_m}{\bar{h}^3} dx}{2 \int_{-L}^L \frac{(\bar{h} - h_m)^2}{\bar{h}^3} dx} \right] (\hat{J}_+ + \hat{J}_-) \\
&= -C_x(P) (\hat{J}_+ + \hat{J}_-).
\end{aligned} \tag{4.20}$$

The timescale σ appears in both τ and in the flux \hat{J} on opposite sides of (4.15) and (4.20), and so these may be rewritten in terms of the original t and J .

When the effects of gravity are important ($\alpha > 0$), pressures are bounded above by P^* in such a way that for drops with $m \gg 1/\alpha$, exponentially small differences in pressure correspond to large differences in mass. To alleviate this computational difficulty, we use

$$Q = \ln(P - P^*), \quad (4.21)$$

the reduced pressure. Carrying through a change of variables from P to Q gives

$$\frac{dQ}{dt} = C_q(Q)(J_+ - J_-) \quad (4.22a)$$

$$\frac{dX}{dt} = C_x(Q)(J_+ + J_-) \quad (4.22b)$$

where now

$$C_q = \left[(P - P^*) \int_{-L}^L \partial_Q h \, dx \right]^{-1}, \quad (4.23)$$

and C_x is unchanged. A plot of C_q for $\alpha = 0.1$ appears in Fig. 4.4, and Fig. 4.1 shows C_x for several values of α . In what follows, we will refer to P and Q interchangeably.

Notice that (4.15) and (4.22a) are just restatements of conservation of mass:

$$\frac{dm}{dt} = J_R - J_L = \frac{dP}{dt} C_p^{-1} \Rightarrow \frac{dm}{dP} = C_p^{-1}$$

and similarly $\frac{dm}{dQ} = C_q^{-1}$. The mass-exchange coefficients may then be estimated from the mass-pressure relationship as

$$C_p \sim -18\sqrt{3}P^3, \quad \text{or} \quad (4.24a)$$

$$C_q \sim -\sqrt{3}\alpha - \frac{(3\alpha^3)^{1/4}}{\sqrt{2}} e^{Q/2} \quad (4.24b)$$

for $\delta \rightarrow 0$ and $Q \rightarrow -\infty$, respectively. The drift coefficient may be estimated by approximating the integrals in (4.20). In [25], this yields

$$C_x \approx \frac{-B}{\delta \log(P/P_{\max})} \quad (4.25)$$

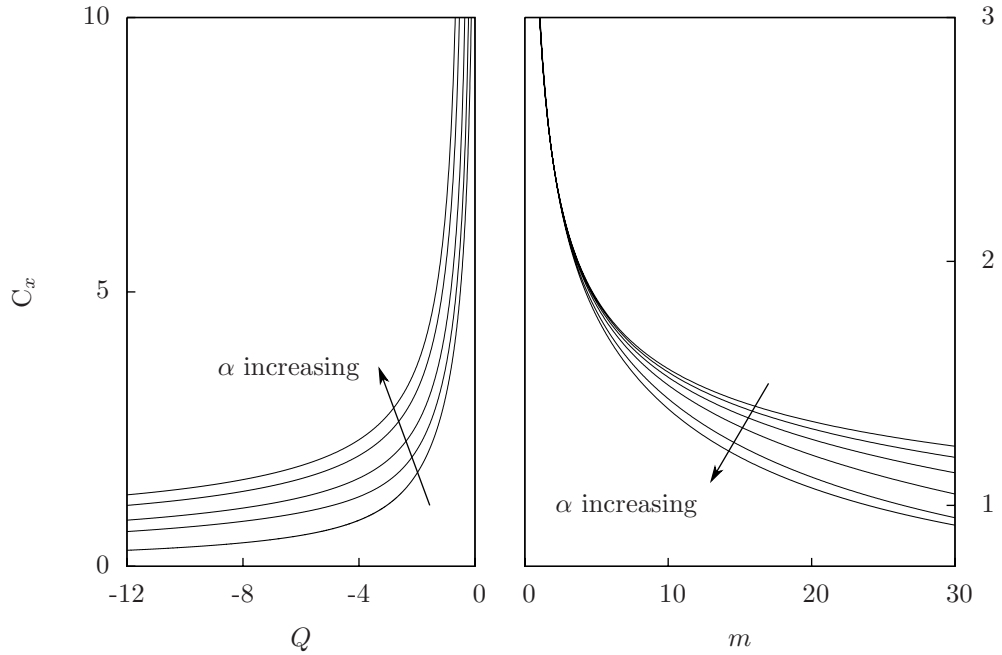


FIGURE 4.1: The drift coefficient C_x for several values of α . Note the right panel has a different C_x scale.

for $\alpha = 0$, where B is positive constant. A similar form holds for $\alpha > 0$, provided m is small, see Fig. 4.1. For larger m , increasing α decreases the drift coefficient.

It is useful to note that both C_x and C_q may be obtained numerically from integrals in the phase plane. The integral mass definition (3.13) already uses $r(h; P)$, and $m(P)$ may be differentiated to obtain C_p . For C_x , we use the inverse function theorem to write

$$C_x = \int_{h_m}^{h_{\max}} \frac{h - h_m}{h^3} \frac{dh}{r(h; P)} \Big/ \int_{h_m}^{h_{\max}} \frac{h - h_m}{h^2} \frac{dh}{r(h; P)}. \quad (4.26)$$

This and (3.13) may be numerically integrated to high accuracy once care is taken to avoid the square root singularity introduced by $r(h; P)$.

4.2 Arrays of interacting drops

Now we look for a simplified description of the flux between two drops by rescaling (2.11) to examine the structure of the ultra-thin film in between. To derive asymptotically valid expressions for the fluxes between drops, we introduce a length scale L as the typical separation distance between two drops. Let $\varepsilon = L^{-1} \ll 1$, and consider the rescaling

$$x = \varepsilon^{-1}z, \quad h = \delta H, \quad t = \delta^{-3}\varepsilon^{-1}\tau, \quad U'(h) = \delta^{-1}\hat{U}'(H). \quad (4.27)$$

The last scaling represents the particular form of the potential evaluated for $h = O(\delta)$. The choice of timescale is motivated by the form of the flux (2.39). In terms of the rescaled variables, (2.11) becomes

$$\delta\varepsilon^{-1}\partial_\tau H = \partial_z \left(H^3 \left[\delta^{-1}\hat{U}'(H) - \delta\varepsilon^2 H_{zz} \right] \right), \quad (4.28)$$

where the curvature term, $\delta\varepsilon^2 H_{zz}$ is evidently small and can be neglected. We can express (4.28) as

$$\delta^2\varepsilon^{-1}\partial_\tau H = \partial_{zz}\hat{V}(H) \quad (4.29)$$

where $\hat{V}(H)$, sometimes called a chemical potential, is defined by

$$\hat{V}(H) = \int^H S^3 \hat{U}''(S) dS. \quad (4.30)$$

Removing the scaling (4.27),

$$V(h) = -3\delta^2 \ln(h) - 4\delta^3/h + \alpha h^4/4. \quad (4.31)$$

From (4.29), the flux between drops can be viewed as the derivative of a function that depends on the spatial variable alone, $\mathcal{V}(x) = V(h(x))$,

$$J = -\partial_x \mathcal{V}. \quad (4.32)$$

The equation for the ultra-thin film (4.29) can be simplified further by assumption (4.11), equivalent to $\delta^2 \varepsilon^{-1} \ll 1$. In this case, the ultra-thin film evolves quasi-statically according to the elliptic problem

$$\begin{aligned} \partial_{xx} \mathcal{V} &= 0 \\ \mathcal{V} &= V(h_m(P_i)) \quad \text{at } x = X_i + w_i \\ \mathcal{V} &= V(h_m(P_{i+1})) \quad \text{at } x = X_{i+1} + w_{i+1} \end{aligned} \tag{4.33}$$

where the boundary conditions match $\mathcal{V}(x)$ to the value of $V(h)$ imposed at the contact line of each adjoining drop. The solution is simply a line connecting the values of V on either boundary. Labeling the left-hand i and the right-hand drop $i + 1$, the flux between them is

$$J_{i,i+1} = -\frac{V(h_m(P_{i+1})) - V(h_m(P_i))}{[X_{i+1} - w(P_{i+1})] - [X_i + w(P_i)]}, \tag{4.34}$$

see Fig. 4.2. Replacing $V(h_m(P))$ by a series expansion in δ yields

$$V(P) = -(3 \ln \delta + 4)\delta^2 + \delta^3 P + O(\delta^4), \tag{4.35}$$

where now V can be thought of as a function of the pressure of a drop. The difference of V values in (4.34) cancels the constant term, leaving

$$J_{i,i+1} \sim -\delta^3 \frac{P_{i+1} - P_i}{[X_{i+1} - w(P_{i+1})] - [X_i + w(P_i)]}. \tag{4.36}$$

This formula matches the basic expectations one has from (2.39) and Fig. 4.2. The value of h^3 is replaced by δ^3 , and $\partial_x p$ is approximated by a simple difference of the pressure values imposed by either adjoining drop. The timescale as set by the flux, $O(\delta^{-3})$, is also consistent with quasi-steady evolution.

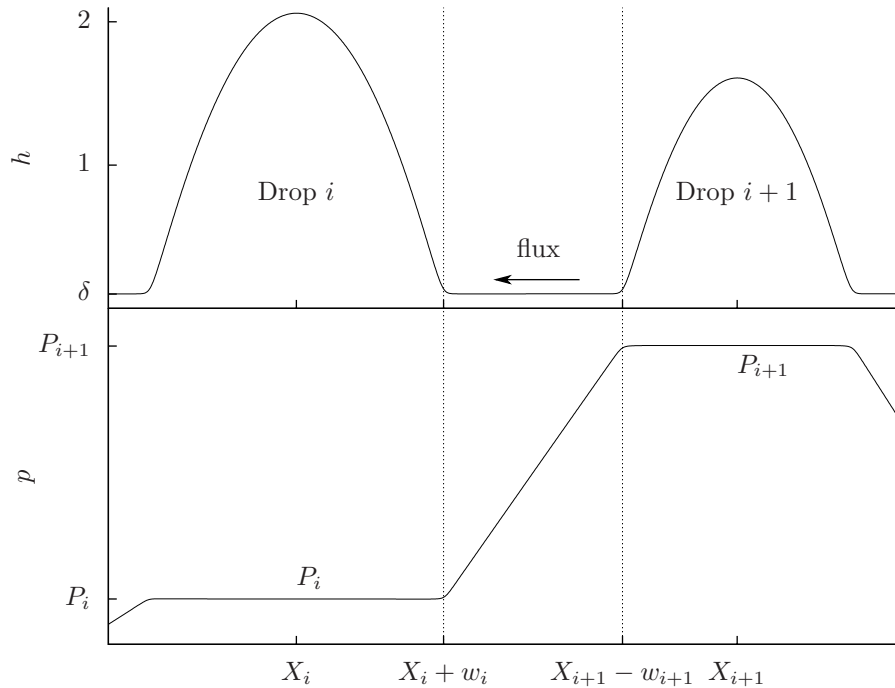


FIGURE 4.2: The flux between two droplets as determined by their pressures. The top shows $h(x, t)$ with the drop widths as determined by (3.16). The bottom shows $p(x, t)$. Note that the pressure is approximately constant inside of the width of each drop and transitions between values linearly as described by (4.34).

4.3 Coarsening Dynamical System (CDS)

We can simulate large numbers of drops using the ODEs (4.22) for the dynamics and coupling neighboring drops through the flux approximation (4.34). This is a major improvement from direct simulation of (2.40), but there are two difficulties with this approach. It is evident from the form of the flux that if the contact lines of two drops touch, the flux becomes unbounded. More subtly, if $P_i > P_{\max}$, drop-type steady states no longer exist (see Fig. 3.2) and the perturbation (4.2) can no longer be formulated. Both of these phenomena result in finite-time blow-up of (4.22). We will avoid these events by altering the system to approximate the dynamics of the PDE near the blow-up of the ODEs through heuristic rules.

These rules may be obtained from observation of the PDE behavior. This idea is predicated on the fact that blow-up is a rapid event — much more rapid than the quasi-steady time scale on which (4.22) is valid — and so it may be approximated by an instantaneous modification to the dynamical system. These modifications are referred to as *coarsening rules*. We refer to the differential equations and the coarsening rules together as a *Coarsening Dynamical System* (CDS). This name was coined by Watson et al. [76] in the context of kink/anti-kink coarsening in the convective Cahn-Hilliard equation where the technique was applied to construct a model similar to the one presented here.

4.3.1 Modes of coarsening and coarsening rules

Each type of finite-time blow-up corresponds to a different class of coarsening event. We investigate the death of a drop in (2.40) to develop coarsening rules for each class.

Collision rule

When the contact lines of neighboring drops overlap, i.e.

$$(X_{i+1} - w_{i+1}) - (X_i + w_i) < \epsilon \tag{4.37}$$

for some $\epsilon \ll 1$, it is no longer true that the flux (2.39) is $O(\delta^3)$. Rather, the evolution of the two-drop complex occurs rapidly. Numerical simulation, shown in Fig. 4.3, demonstrates that the mass and center of mass are approximately conserved in the two-drop system¹. Other authors [25] also confirm this. We therefore replace colliding drops i and $i + 1$ by a new drop with mass

$$m_i^{\text{new}} = m_i + m_{i+1} \tag{4.38a}$$

¹ The PDE (2.40) does not conserve the center of mass. This may be observed in Fig. 1.1, where the initial center of mass is at the middle of the domain, but the center of mass in the final frame is slightly to the right.

and position

$$X_i^{\text{new}} = \frac{m_i X_i + m_{i+1} X_{i+1}}{m_i + m_{i+1}}, \quad (4.38b)$$

and relabel all of the drops with indexes greater than i .

Collapse rule

If $P_i > P_{\text{max}}$, drop-type solutions no longer exist. However, examining C_q (shown in Fig. 4.4) shows that there is a unique global minimum at Q_{fast} where the drop is changing pressure the fastest. To avoid unnecessary refinement of the time step when integrating near the collapse of a drop, we instead delete drops with $Q_i > Q_{\text{fast}}$. To conserve mass, we add the remaining small amount of mass to the two neighboring drops as weighted by their relative fluxes at the time of collapse:

$$m_{i-1}^{\text{new}} = m_{i-1} + m_i \frac{|J_{i-1,i}|}{|J_{i-1,i}| + |J_{i,i+1}|} \quad m_i^{\text{new}} = m_{i+1} + m_i \frac{|J_{i,i+1}|}{|J_{i-1,i}| + |J_{i,i+1}|}, \quad (4.39)$$

and relabel all of the drops with indexes greater than i .

4.3.2 *Thin film CDS*

Combining (4.22) with the rules gives the full model for drops $i = 1, 2, \dots, N$:

$$\frac{dQ_i}{dt} = C_q(Q_i)(J_{i,i+1} - J_{i-1,i}) \quad (4.40a)$$

$$\frac{dX_i}{dt} = C_x(Q_i)(J_{i,i+1} + J_{i-1,i}) \quad (4.40b)$$

$$\text{Collision: If } (X_i + w_i) - (X_{i+1} - w_{i+1}) < \epsilon, \quad (4.40c)$$

then merge $i, i + 1 \rightarrow i$ via (4.38)

$$\text{Collapse: If } Q_i > Q_{\text{fast}}, \text{ then delete } i \text{ and use (4.39)} \quad (4.40d)$$

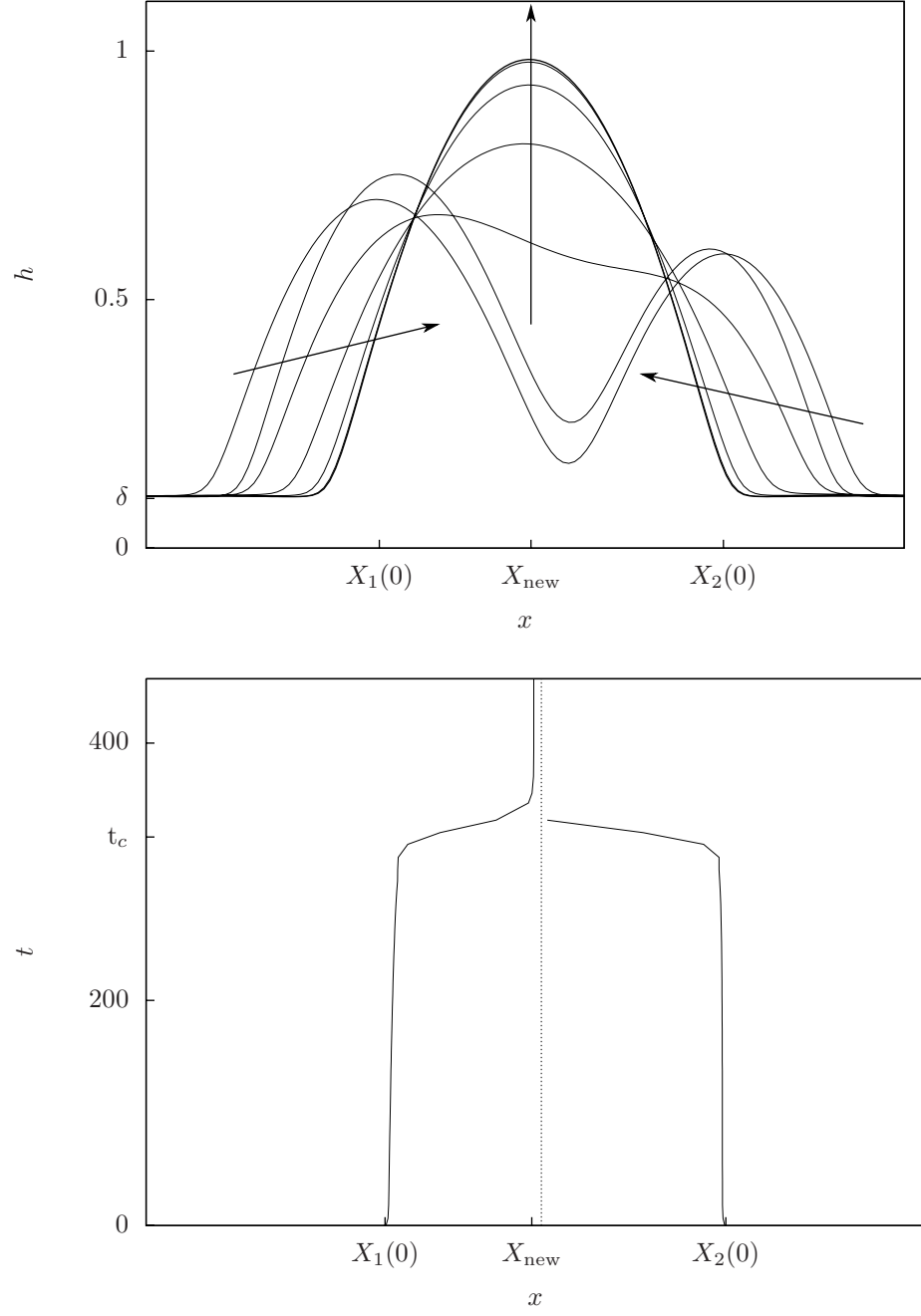


FIGURE 4.3: Top: the contact lines of two drops touch and they coalesce rapidly (37 time units compared to $\delta^{-3} = 1000$). Bottom: The center of mass of each drop around the time of the collision, t_c . The dotted line is the initial center of mass of the two-drop system.

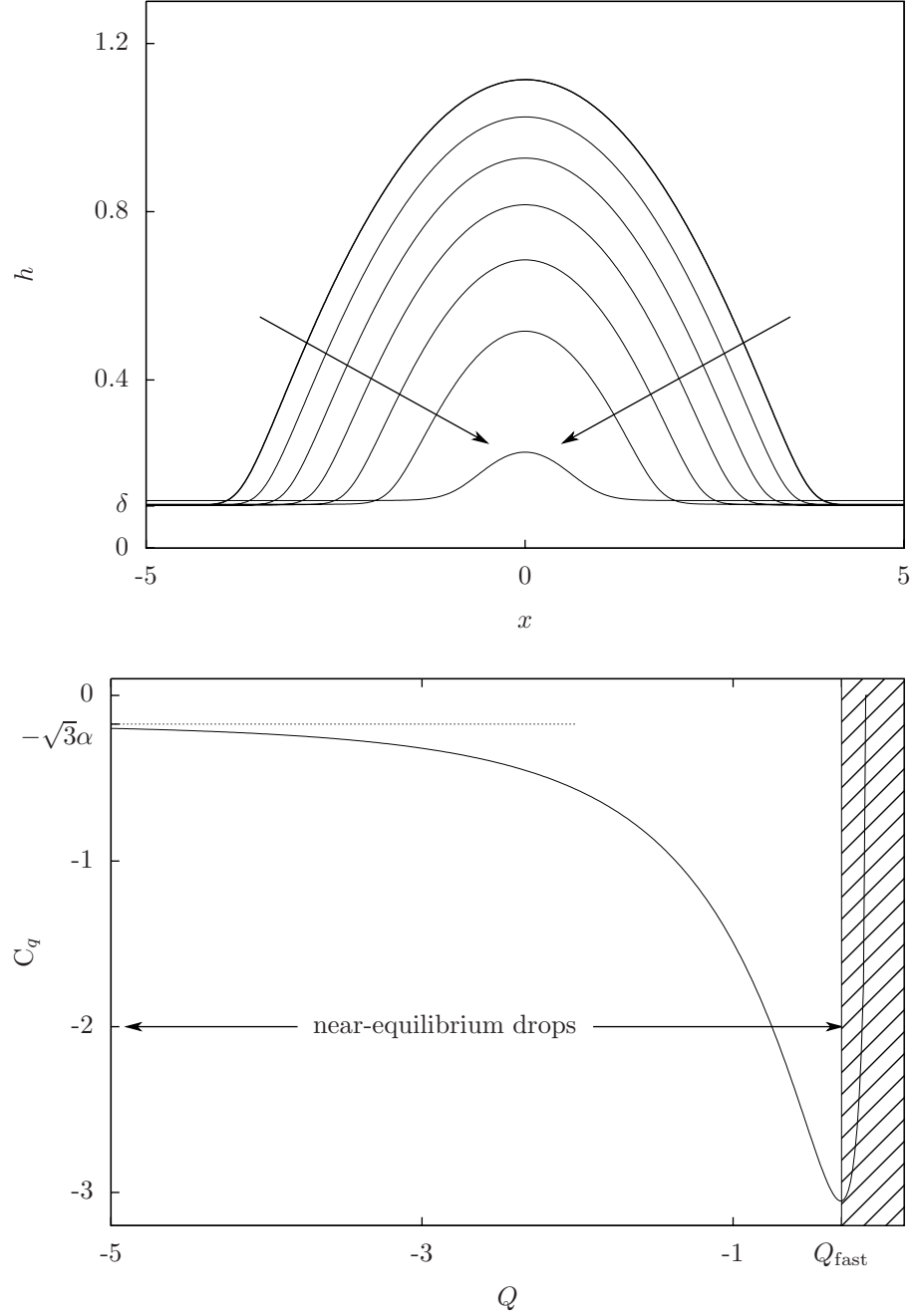


FIGURE 4.4: Top: A drop loses all of its mass due to outward fluxes. See also Fig. 3.8 where the arrows also show the direction of quasi-static evolution for a shrinking drop. Bottom: The mass-exchange coefficient $C_q(Q)$ showing a global minimum Q_{fast} where the drop shrinks rapidly.

4.4 Dilute limit of the CDS

Some immediate insight into (4.40) can be obtained by simple scaling analysis. We review here the work of Glasner and Witeliski [25, Sec. 4.1]. Assuming that droplets are dilute (widely spaced compared to their widths), the CDS may be rescaled to see two parameters that control the coarsening behavior. The dilute assumption may be written

$$J_{i,i+1} = -\frac{V(h_m(P_{i+1})) - V(h_m(P_i))}{X_{i+1} - X_i}, \quad (4.41)$$

where the drop widths have been neglected. Suppose the mean drop has mass \bar{m} and is separated from its neighbors by an average center-to-center distance of ℓ . If $\alpha = 0$, (3.17) holds, so

$$\bar{P} \sim \frac{1}{3^{5/4}\sqrt{\bar{m}}}, \quad (4.42)$$

and approximation (4.24a) is appropriate. These suggest the rescaling

$$P_i(t) = \bar{P}\mathcal{P}(\tau), \quad X_i(\tau) = \ell\mathcal{X}(\tau), \quad t = \frac{\ell}{18\sqrt{3}\delta^3\bar{P}}\tau. \quad (4.43)$$

Using approximations (4.24a), (4.36), and (4.41), we have

$$\frac{d\mathcal{P}_i}{d\tau} = -\mathcal{P}_i^3 \left(\frac{\mathcal{P}_{i+1} - \mathcal{P}_i}{\mathcal{X}_{i+1} - \mathcal{X}_i} - \frac{\mathcal{P}_i - \mathcal{P}_{i-1}}{\mathcal{X}_i - \mathcal{X}_{i-1}} \right), \quad (4.44a)$$

$$\frac{d\mathcal{X}_i}{d\tau} = -\frac{\mathbb{K}}{\ln(\mathbb{R}\mathcal{P}_i)} \left(\frac{\mathcal{P}_{i+1} - \mathcal{P}_i}{\mathcal{X}_{i+1} - \mathcal{X}_i} + \frac{\mathcal{P}_i - \mathcal{P}_{i-1}}{\mathcal{X}_i - \mathcal{X}_{i-1}} \right). \quad (4.44b)$$

The two parameters are

$$\mathbb{K} = \frac{4B\bar{m}}{\delta\ell}, \quad \mathbb{R} = \frac{\bar{P}}{P_{\max}}, \quad (4.45)$$

where B is the constant from (4.25) and $\mathbb{R} > 1$ by virtue of the collapse rule. For $\alpha > 0$, similar scalings hold.

In either case, the reduced *coarsening parameter* \mathbb{K} represents mass density and directly controls the speed of droplet drift (in [25], the coarsening parameter is defined as $\delta\mathbb{K}$). The denominator of the same term in (4.44b) changes with time, but logarithmically. For a coarsening system, the surviving drops are larger, hence \bar{P} is growing. This causes drift to become less and less important as coarsening continues. Glasner and Witelski also show that $\mathbb{K} < 1$ corresponds to collapse-dominated coarsening, while large values of \mathbb{K} indicate collision dominated behavior. The bifurcation in system behavior at about $\mathbb{K} = 1$ is fairly sharp. Unless otherwise specified, we consider only $\mathbb{K} < 1$.

In summary, the CDS model (4.40) reduces the thin film equation (2.40) to a system of $2N$ ODEs for N drops. Coarsening events are simulated through the coarsening rules of merging (4.38) and deleting (4.39) drops. The dominant mode of coarsening can be controlled by varying the coarsening parameter \mathbb{K} , and by keeping $\mathbb{K} < 1$, we can avoid collision events.

Droplets coarsening subject to gravity

Starting with several drops connected by an ultra-thin film in (2.40), the work in the previous chapter shows this state will evolve slowly to reduce the number of drops and thereby equalize the pressure. Figure 5.1 shows the result of partial differential equation (PDE) simulations using the method described in Appendix A over a long time period. Drops vanish through the collapse coarsening mechanism that will be the focus of this chapter. Notice that small parabolic drops generally decrease in mass until they collapse, while the surviving drops are larger on average and more mesa-like in shape.

We efficiently compute the coarsening behavior using the coarsening dynamical system (CDS) description (4.40). This model enables us to study the properties of very large systems of interacting drops. Here, we focus on $N(t)$, the number of surviving drops. The number of drops is a robust quantity that is easy to measure experimentally and whose behavior determines the scales for other evolving properties in the system. We will explore more detailed measurements of coarsening in Chapter 6.

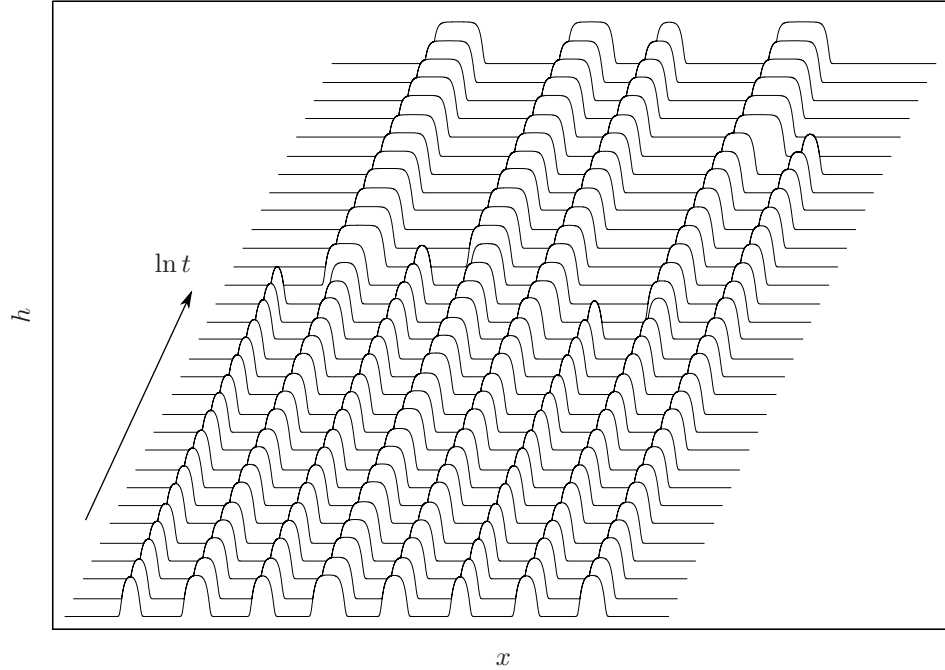


FIGURE 5.1: A numerical simulation of a small array of interacting drops using the PDE model (2.40).

5.1 CDS model parameters

We start with N_0 initial drops in a domain of length L with no-flux boundary conditions at its edges. The total active mass $M_c = \sum_{i=1}^N m_i$ (and hence \mathbb{K}) is conserved throughout each simulation.¹ Drops in the array are chosen to be initially equally-spaced and have mass randomly distributed about a mean,

$$X_i = i\ell \tag{5.1a}$$

$$P_i = P(\mathcal{N}(\bar{m}_0, \sigma)), \tag{5.1b}$$

for $i = 1, 2, 3, \dots$, and where $\ell = L/N_0$ and $P(m)$ is the inverse function that relates mass to pressure found numerically from (3.13). $\mathcal{N}(\bar{m}, \sigma)$ is the normal distribution with mean $\bar{m}_0 = M_c/N_0$ and standard deviation σ . Other choices for the initial

¹ The UTF layer is adsorbed to the substrate, and while it is essential to the dynamics, its mass is constant up to $O(\delta)$. The definition of m in (3.13) also excludes mass below h_m , consistent with this definition.

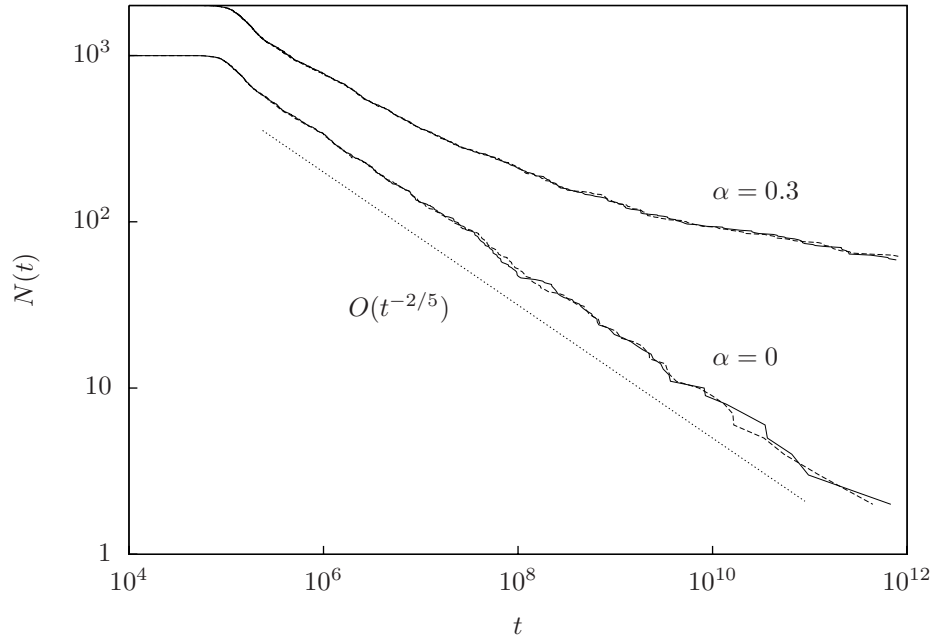


FIGURE 5.2: The total number of drops N versus t for the model with drift (solid) without drift (dashed). The differences in the curves are more noticeable when N is small. The dotted line shows the predicted power law for $\alpha = 0$.

distribution are possible, and the effects of the initial distribution on the early-time dynamics are explored in Chapter 6. If $\alpha > 0$, we will compute using $Q = \ln(P - P^*)$ instead of P , but this is for numerical convenience and does not effect the results. For all computations shown here, we use a fourth order adaptive Runge-Kutta scheme. We tabulate h_m , w , C_x , and C_q for Q ahead of computation and interpolate using cubic splines to supply these values when they are needed in the simulation. All computations use parameters $\delta = 0.1$, $0 < \alpha < 0.5$, and $\mathbb{K} \leq 1/2$.

With these parameters, the influence of the drift equations $\frac{dX_i}{dt}$ (4.40b) are negligible. Figure 5.2 shows the results of simulations with drift (dashed lines) and without drift (solid lines). In each run, $\bar{m}_0 = 1$, $\sigma = 0.1$, and $\mathbb{K} = 1/4$. The $\alpha = 0.3$ runs use 2000 initial drops so that the two cases are graphically distinct. The onset of coarsening can be seen around $t = 10^5$, and after this self-similar coarsening be-

havior sets in. The variation between the model without drift (4.40a) and the full model (4.40) only becomes apparent as the number of drops becomes small. Even here, both curves still follow the same average trend, though with different variations. Examining C_x as a function of m shows that larger drops move slower, and the rate of slow-down is proportional to α (see Fig. 4.1). We use this observation as motivation to neglect the drift equations (4.40b) for simulations in this chapter. For $\alpha = 0$, there is a clear $N \propto t^{-2/5}$ power law that can be observed across six decades. This behavior was first discovered in [24] and a rigorous proof of the coarsening rate appears in [54]. The $\alpha = 0.3$ curve appears to follow the power law for times close to onset, but longer times show the rate slowing down. At $t = 10^{12}$, there are some 60 drops remaining for $\alpha = 0.3$, compared to only 2 for $\alpha = 0$.

5.2 Non-power-law behavior

When α is positive, non-power-law behavior is clear at large times. The pressure-dependence of the drop shape due to the presence of gravity causes a dramatic slow down in the coarsening rate. While the rate approaches a $t^{-2/5}$ power law when the drops are parabolic, it slows down as more drops grow to become mesa-like (see Fig. 5.1). The effects of changing α over a range of values can be seen in Fig. 5.3, where we plot $N(t)$ on a log-log scale. To properly compare initial conditions, we use (5.1) in all simulations, with $\bar{m}_0 = 2$ and $\mathbb{K} = 1/2$; for each α this distribution yields a different range of Q_i due to the form of (3.27b). The $\alpha = 0$ curve follows the power law to the end of the coarsening regime, but all of the $N(t)$ curves with $\alpha > 0$ eventually deviate from this behavior. For the smallest value plotted, $\alpha = 0.02$, the curve maintains the power law for nearly seven decades, after which the coarsening rate slows. For the largest value, $\alpha = 0.5$, $N(t)$ slows from the power law almost immediately. The coarsening is quite slow; after 10^{40} units of time, nearly 1300 drops

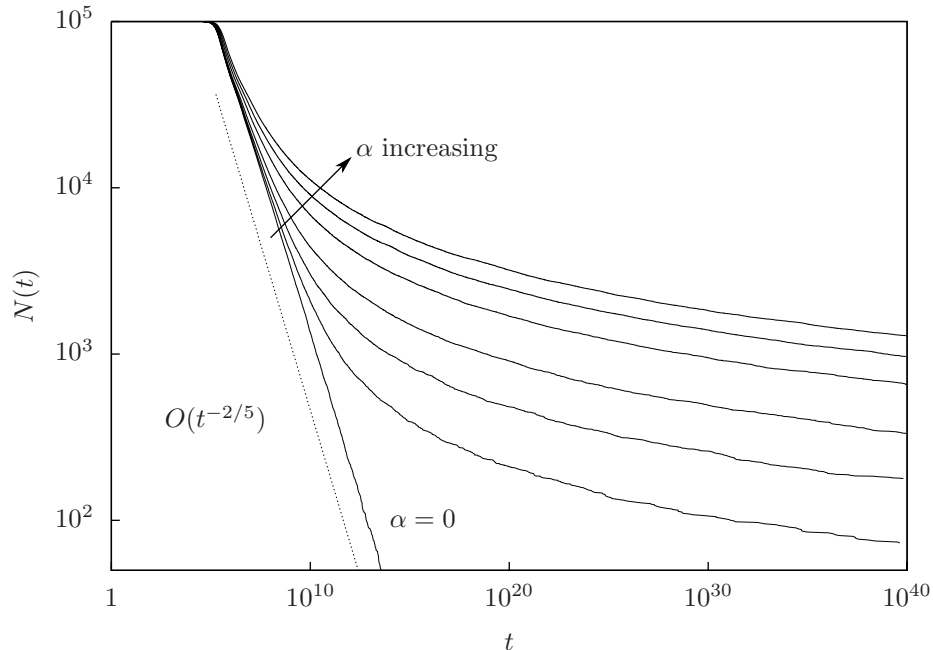


FIGURE 5.3: The coarsening rate as modified by α for $0 \leq \alpha \leq 0.4$. The results for $\alpha = 0$ follow a $t^{-2/5}$ power-law behavior (dotted), different from the results for $\alpha > 0$.

remain for $\alpha = 0.5$, while the $\alpha = 0$ system has essentially reached steady-state 24 decades earlier.

In Fig 5.4, several simulations with $\alpha = 0.1$ and $N_0 = 10000$ show different onsets of the slower coarsening behavior tied to different values of the droplet initial mass, $0.5 \leq \bar{m}_0 \leq 20$. The coarsening parameter is fixed at $\mathbb{K} = 1/5$ by varying ℓ in proportion to \bar{m}_0 . For $\bar{m}_0 = 20$ and $\bar{m}_0 = 17.5$, the two largest values plotted, $\bar{\mathbb{M}} = \bar{m}_0 \alpha \gg 1$ and so the droplets are initially mesa-like. The slower coarsening is in effect for these curves almost at the onset of the coarsening itself. For the smallest value of \bar{m}_0 , drops are initially parabolic with $\bar{\mathbb{M}} = 1/20$, and the $N(t)$ curve can be seen following the power law for several decades.

To study the long-time dependence of the coarsening rate on the drop shape, we first choose an appropriate timescale. We are interested in times when the average

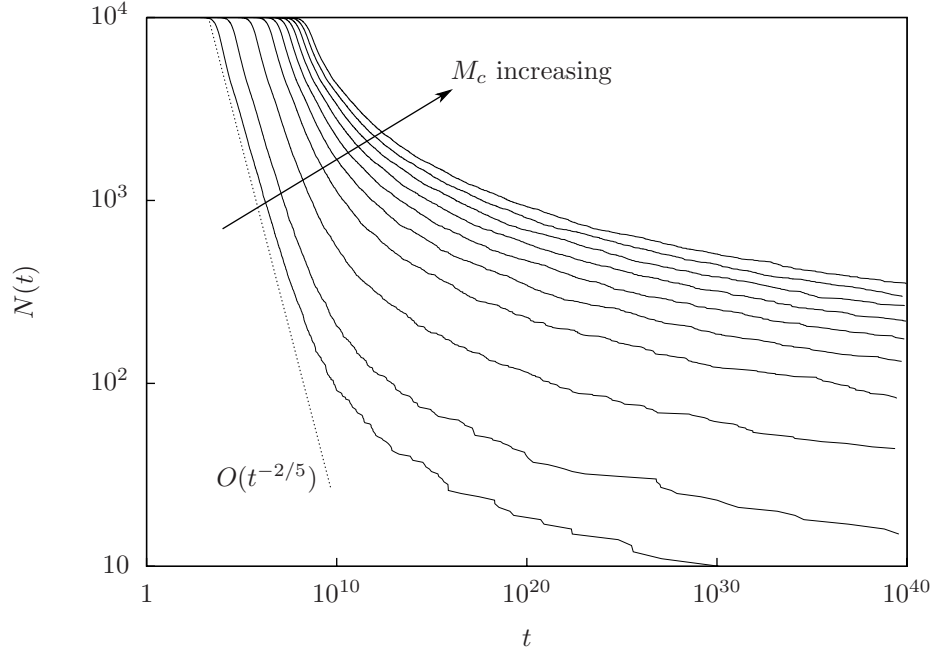


FIGURE 5.4: The coarsening rate as affected by changing \bar{m}_0 , with $0.5 \leq \bar{m}_0 \leq 20$ and fixed $\alpha = 0.1$.

drop has the mesa shape (3.23). Examining (4.22a), we see that the appropriate timescale must account for values of Q , C_q , and J in the range of mesa drops. For these drops, (3.27b) suggests scaling Q by $\alpha\bar{m}_0$, (4.24b) shows that $C_q(Q)$ scales like α , and J scales like the drop separation ℓ . Taken together, these scaling relations motivate the choice of timescale

$$\tau = t/T \quad \text{where} \quad T = \frac{1}{\alpha^2 \mathbb{K}}. \quad (5.2)$$

The limit $\alpha \rightarrow 0$ forces $T \rightarrow \infty$. Hence the timescale T is when the remaining array is dominated by mesa-like drops and slow coarsening occurs may be very long if α is small². In fact, if $\alpha M < 1$ then all coarsening will follow the power law leading to a single final parabolic drop. We will focus attention on the behavior of the other case, $\alpha M > 1$, for the remainder of this section.

² Physically, the timescale corresponds to the typical time for a drop to grow large enough that ℓ_c/H is comparable to Ξ^{-1} , the inverse of the healing parameter

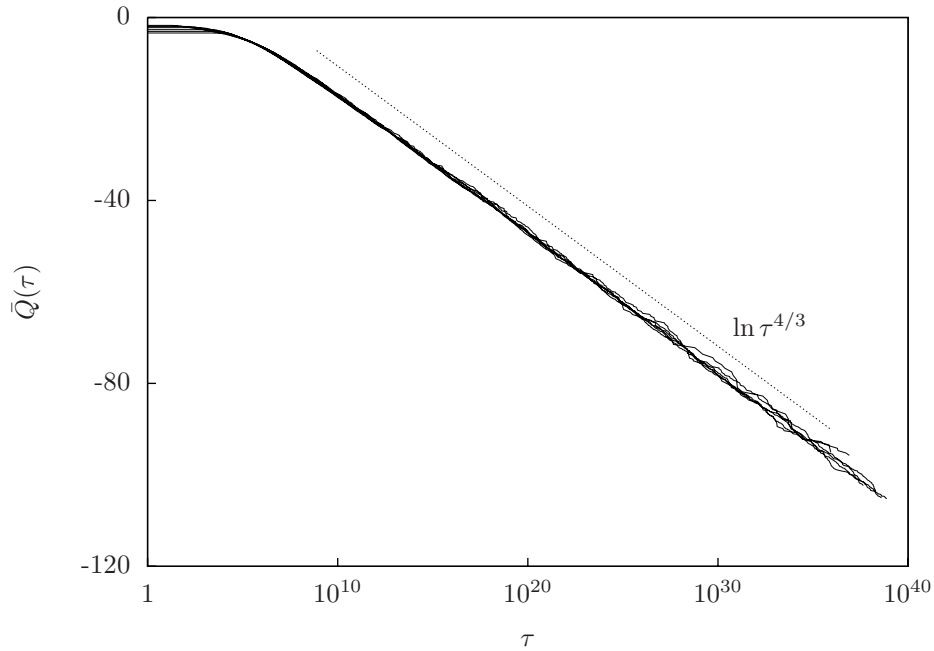


FIGURE 5.5: The mean log excess pressure \bar{Q} versus τ for the simulations shown in Fig 5.3. The dashed line shows the conjectured behavior.

Using the new time τ , our simulations show the self-similar structure of the coarsening. From the data used for Fig. 5.3, we conjecture that

$$\bar{Q}(\tau) \approx \ln \tau^{-4/3}, \quad (5.3)$$

see Fig 5.5, where the value 1.33 was obtained from a one-parameter numerical fit. Further work is needed to understand this result. Using the fact that the total mass M is constant, we can write

$$N(\tau; \alpha) = \frac{\bar{m}_0}{\bar{m}(\tau)} N_0 \quad (5.4)$$

where $\bar{m}(\tau)$ is the current mean droplet mass. The dynamics of $\bar{m}(\tau)$ can then be found by using (3.27b) and replacing Q by $\bar{Q}(\tau)$. Doing this gives

$$\bar{m}(\tau) \approx \frac{1}{\sqrt{3\alpha}} (\ln \tau^{4/3} + \frac{1}{2} \ln \alpha). \quad (5.5)$$

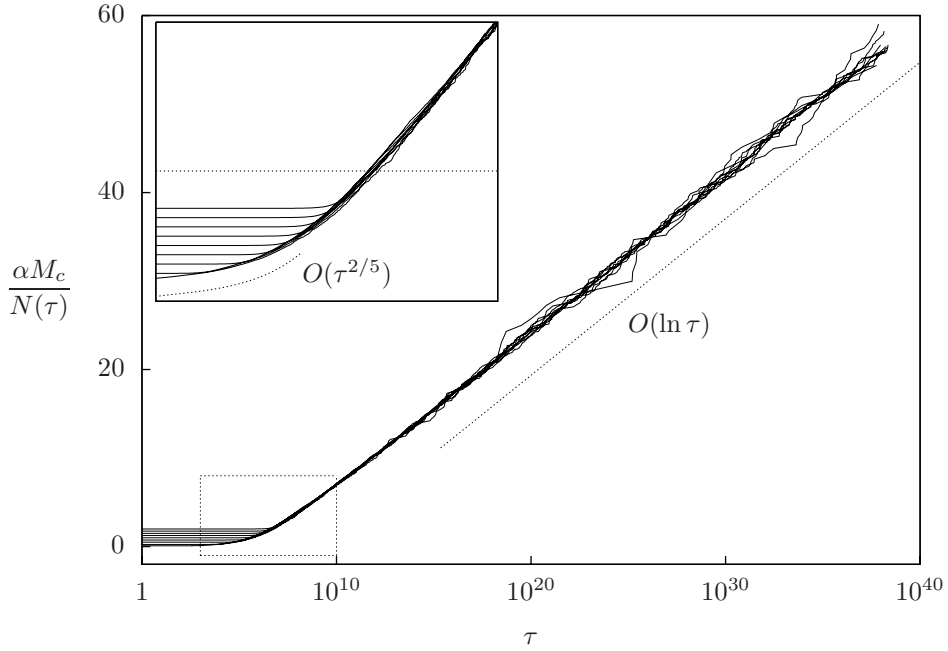


FIGURE 5.6: The same data as in Fig 5.4 plotted using $\alpha M_c/N$ versus τ . The dotted line is the prediction (5.7) for long times. The boxed region is shown enlarged in the inset, where the horizontal dotted line divides mesa-like behavior and parabolic-like behavior. The line corresponds to \bar{M} being large. Below this line, the power law for parabolic drops can be seen.

Using (5.4),

$$N(\tau) \approx \frac{\sqrt{3}\alpha M_c}{\ln \tau^{4/3} + \frac{1}{2} \ln \alpha}, \quad (5.6)$$

where the $\frac{1}{2} \ln \alpha$ term acts to scale the onset time of slow coarsening. In rough terms,

$$N(\tau) \propto \frac{\alpha \bar{m}_0}{\ln \tau} N_0 \quad \text{for } \tau \rightarrow \infty, \quad (5.7)$$

see Fig 5.6. Instead of a power law, N decays at a slow inverse logarithmic rate. In terms of the mesa parameter, this behavior is equivalent to $\alpha \bar{m}_0 N_0 / N = \bar{M}(\tau) \propto \ln \tau$, where $\bar{M} = \bar{M}(\tau)$ is the average mesa parameter. Thus increasing either α or \bar{m}_0 increases the initial \bar{M} , causing slower coarsening to begin earlier.

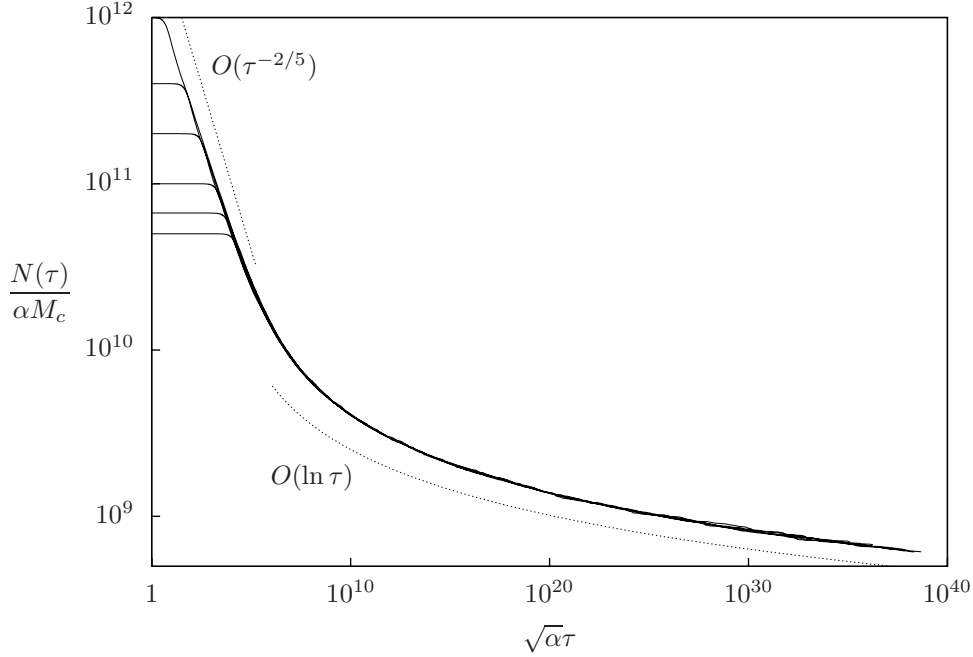


FIGURE 5.7: The data of both Fig 5.4 and Fig 5.3 replotted using $N/(\alpha M_c)$ versus $\sqrt{\alpha\tau}$. All curves collapse onto a single trend that follows the parabolic drop power law for short times and the mesa drop inverse logarithmic behavior for long times (both shown dotted).

Re-plotting the data in Fig 5.4 with $\alpha M_c/N$ versus τ (Fig 5.6) shows that all of the curves collapse onto a single large τ trend as described by (5.6). The inset shows an enlargement of the boxed early-time portion. The transition from the power law to the log-law occurs on either side of the dotted horizontal line representing large \bar{M} .

It is also illustrative to plot $N/(\alpha M_c)$ against $\sqrt{\alpha\tau}$ on a log-log plot, as in Fig 5.7 where all of the data from Fig 5.3 and Fig 5.4 are re-plotted. This scaling shows both the small and large \bar{M} behavior collapsed onto a single trend. Short times exhibit the parabolic drop related power law, while long times display the mesa drop related³ log-law.

³ Even in the regime of large \bar{M} , the drop population still consists of a range of drops from small parabolic drops to large mesa drops, but the behavior of the smaller drops is less important.

The $\alpha = 0$ rate of $N \propto t^{-2/5}$ is an upper-bound approached when the mean mesa parameter $\bar{\mathbb{M}}(t) \ll 1$. Provided there is sufficient total mass, the decrease in the number of drops forces the average drop mass to grow, eventually making $\bar{\mathbb{M}} \gg 1$. This shift changes the shape, and more importantly, the mass-to-pressure relationship of the average drop. This results in the slower log-law (5.7) coarsening rate, a reflection of the growth of $\bar{\mathbb{M}}$ with time in the later stages of coarsening.

5.3 Energy incentive to coarsen for large drops

To understand the slow-down of coarsening, we examine the energy dissipated by each coarsening event. The thin film equation, and thin film coarsening by extension, is a dissipative system. The total energy (3.1) is non-increasing, and the elimination of a drop is always energetically favorable. An array of N identical drops is in unstable equilibrium, and the metastable dynamics that takes this state to $N - 1$ drops can be understood in terms of the *energy incentive* $\Delta E < 0$ of a coarsening event. In this section, we examine the effect of gravity on the size of ΔE . A smaller ΔE is suggestive of slower coarsening, though not conclusive evidence of it.

As a model system, consider two near steady-state drops on a domain of size L with no-flux boundary conditions. We locate the maxima of these drops on the left and right edges of the domain, effectively eliminating droplet drift using the boundary conditions. We examine the effect of $\bar{\mathbb{M}} = \alpha(m_l + m_r)/2$ on ΔE , where m_l and m_r are the half-masses of the left and right drops. Since the system coarsens through collapse, ΔE is not well-defined, as we may choose to measure the initial energy at any point before the disappearance of one of the drops. However, since we assume that both drops are large ($\bar{\mathbb{M}} \gg 1$), these effects are mitigated by the form of the energy approximations below.

The energy of the two drop system may be decomposed into three terms,

$$E_2 = E_{w1} + E_{st} + E_\alpha,$$

where

$$E_{w1} = \left(L - \sum_i w_i \right) U(\bar{h}_m) \quad (5.8a)$$

$$E_{st} = \sum_i \int_0^{w_i} \left(\frac{dh}{ds} \right)^2 ds \quad (5.8b)$$

$$E_\alpha = \alpha \sum_i \int_0^{w_i} h^2 ds. \quad (5.8c)$$

Here $s = x - X_i$ is a local coordinate inside each drop and $i = l, r$. The usual factor of one-half in E_{st} and E_α cancels with the factor of two from writing the integrals over 0 to w_i . These terms are the energy from space outside of drops at the mean field UTF thickness ($\bar{h}_m \approx \delta$), energy from surface tension, and energy from gravity, respectively. The above formulation of the energy assumes that the gravitational and surface tension energies of the wetting layer are negligible. As the height is $O(\delta)$, the gravitational energy contribution is $O(\delta^2)$ and can be neglected provided $L\delta^2 \ll 1$. The shape of the wetting layer is controlled by the scaled film equation (4.29), and $\frac{dh}{dx} = O(\delta/L)$, making the surface tension energy $O(\delta^2/L^2)$. We have also assumed that the energy from intermolecular forces inside of a drop is negligible. The outer solutions for steady-state drops in Chapter 3 all proceed by dropping the $O(\delta^2)$ effects of the wetting potential, and so we incur errors here of $O(\delta^2 w_i)$ here. Since we have already assumed $L\delta^2 \ll 1$ and $w_i < L$, we may safely neglect this piece of the energy as well.

5.3.1 Basic expansions of the energy

We use asymptotic results from Chapter 3 to simplify the expression for the energy in the limit of large mass drops.

The mass-pressure relationship (3.27b) may be inverted to find

$$Q(m) \sim 2 \ln \left(\frac{2h_\alpha^*}{\beta^*} \right) - \frac{4h_\alpha^*}{\lambda_\alpha^{*2}\beta^{*2}} - \frac{2}{\lambda_\alpha^*\beta^{*2}}m \approx -\sqrt{3}\alpha m + \frac{1}{2} \ln \alpha \quad (5.9)$$

in the limit of large \mathbb{M} . This equation allows us to re-express (3.27a) as

$$w(m) \sim \frac{2h_\alpha^*}{\lambda_\alpha^*} + \frac{1}{\lambda_\alpha^{*2}\beta^{*2}}m \approx \frac{\sqrt{3}}{2}\sqrt{\alpha}m + \frac{1}{4\sqrt{\alpha}} \ln\left(\frac{4}{3}\right). \quad (5.10)$$

Notice that as $\mathbb{M} \rightarrow \infty$ the $O(1)$ term shrinks in importance, leaving $w(m)$ as a linear function in m .

Using (3.5a), we may also rewrite (5.8a) as

$$E_{\text{wl}} = -\frac{1}{6} \left(L - \sum_i w_i \right) + O(\delta^2). \quad (5.11)$$

The energy cost of introducing a drop of mass m_i into a domain of size L is

$$E_{\text{wl}}^i \sim \frac{1}{6\lambda_\alpha^{*2}\beta^{*2}}m_i + \frac{2h_\alpha^*}{\lambda_\alpha^{*3}\beta^{*2}} \approx \frac{1}{3\sqrt{\alpha}} + \frac{\sqrt{3\alpha}}{12}m_i. \quad (5.12)$$

Note this expression is positive; the removal of a drop frees space to be at height $O(\delta)$, where $U(h)$ is near its global minimum (see Fig. 2.3). The creation of UTF is the dominant energy incentive for coarsening. E_{wl}^i increases like $\mathbb{M}/\sqrt{\alpha}$.

The contribution of a drop of mass m_i to each energy term may be estimated using the approximation (3.23). The surface tension energy in the drop is

$$\begin{aligned} E_{\text{st}}^i &\sim \frac{\lambda^* h_\alpha^{*2}}{2} - \frac{2h_\alpha^* \exp(-4h_\alpha^*/\lambda_\alpha^{*2}\beta^{*2})}{\beta^{*2}} m_i \exp(-2m_i/\lambda_\alpha^*\beta^{*2}) \\ &\approx \frac{1}{6\sqrt{\alpha}} - e^{-2\alpha m_i} e^{-\sqrt{3}\alpha m_i}, \end{aligned} \quad (5.13)$$

where we have used the approximation $\cosh(\sqrt{\alpha}w_i) \sinh(\sqrt{\alpha}w_i) \sim \exp(\sqrt{2\alpha}w_i)/4$ for large w_i . As $\mathbb{M} \rightarrow \infty$, $E_{\text{st}}^i \rightarrow \frac{1}{6\sqrt{\alpha}}$, a fixed value. The gravitational energy is

$$E_\alpha^i \sim \frac{3h_\alpha^{*2}\alpha}{2\lambda_\alpha^*} + \frac{4h_\alpha^{*3}\alpha}{2\lambda_\alpha^{*3}\beta^{*2}} + \frac{\alpha h_\alpha^{*2}}{\lambda_\alpha^{*2}\beta^{*2}}m_i \approx \frac{5}{6\sqrt{\alpha}} + \frac{\sqrt{\alpha}}{2\sqrt{3}}m_i, \quad (5.14)$$

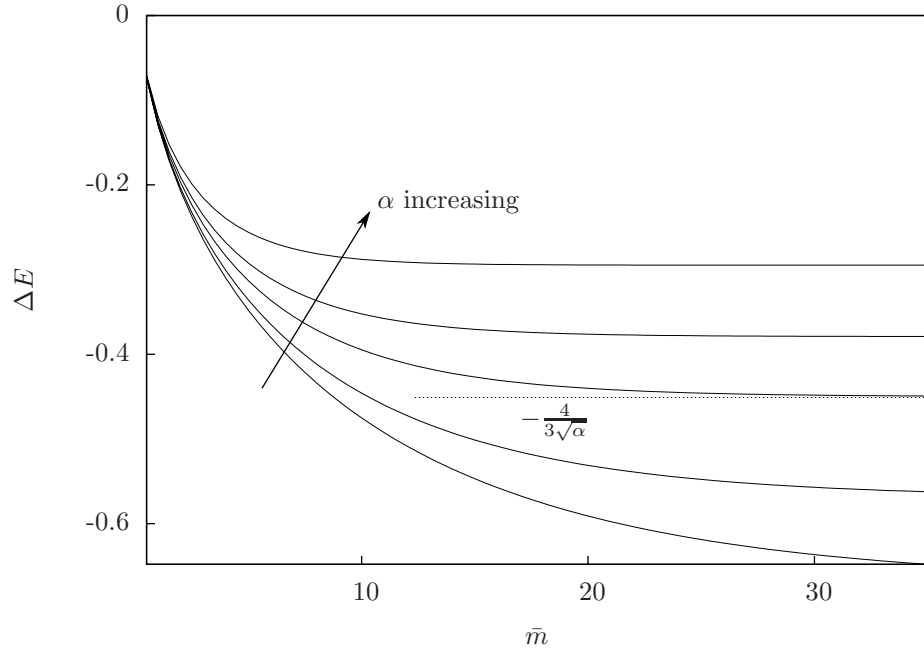


FIGURE 5.8: The energy change after two drops coarsen into one drop. ΔE saturates at a negative value that depends inversely on α .

where we have used a similar approximation for the hyperbolic functions. This expression grows with $M/\sqrt{\alpha}$.

5.3.2 Energy released in a two-drop system

As the system of drops m_l and m_r coarsens into one drop with mass m_c , the liberated energy ΔE may be calculated as $\Delta E = E_c - E_2$. Before the merger,

$$\begin{aligned}
 E_2 &\sim -\frac{L}{6} + \frac{2h_\alpha^*}{3\lambda_\alpha^{*3}\beta^{*2}} + \frac{1}{\lambda_\alpha^{*2}\beta^{*2}}(m_l + m_r) \\
 &\quad + \frac{3h_\alpha^{*2}\alpha}{\lambda_\alpha^*} + \frac{4h_\alpha^{*3}\alpha}{\lambda_\alpha^{*3}\beta^{*2}} + \frac{\alpha h_\alpha^{*2}}{\lambda_\alpha^{*2}\beta^{*2}}(m_l + m_r) + \lambda_\alpha^* h_\alpha^{*2} \\
 &\approx -\frac{L}{6} + \frac{8}{3\sqrt{\alpha}} + \frac{\sqrt{3\alpha}}{4}(m_l + m_r).
 \end{aligned} \tag{5.15}$$

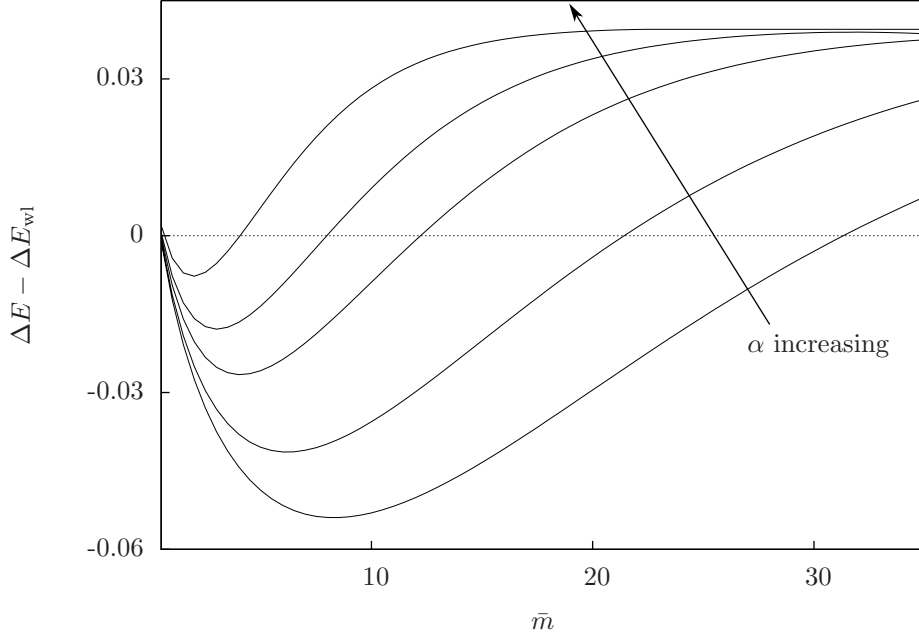


FIGURE 5.9: The energy change excluding ΔE_{wl} . Each curve crosses the axis at $\mathbb{M} \approx 1$ (equivalent to $\bar{m} = 1/\alpha$).

Afterward, since $m_c = m_l + m_r$, E_c is nearly the same as E_2 . The only remaining terms are

$$\Delta E \sim -\frac{h_\alpha^*}{3\lambda_\alpha^{*3}\beta_\alpha^{*2}} - \frac{3h_\alpha^{*2}\alpha}{2\lambda_\alpha^*} - \frac{4h_\alpha^{*3}\alpha}{\lambda_\alpha^{*3}\beta_\alpha^{*2}} - \frac{\lambda_\alpha^*h_\alpha^{*2}}{2} \approx -\frac{4}{3\sqrt{\alpha}}. \quad (5.16)$$

The first decaying term in ΔE is $O(me^{-\sqrt{3}\alpha m})$. While other quantities in the coarsening system are growing (the mean drop separation, the mean mass that must be removed for a collapse to occur), the energy incentive approaches a fixed value.

Computing the energy numerically from simulating (2.40) allows us to calculate the ΔE of a coarsening event as a function of the total mass in the system. Figure 5.8 shows the result of a PDE simulation of a two drop system coarsening into one drop through a collapse. The two drops are pinned to the no-flux boundaries, so no motion occurs. The energy incentive ΔE saturates at the value predicted in (5.16). If E_{wl} is excluded (see Fig. 5.9), there is a striking transition from negative to positive energy

change that occurs at about $\bar{m} = 1/\alpha$. For larger systems, $\bar{M} > 1$ and drops have a mesa shape. Surface tension energy, which can be reduced by the merger of two small parabolic drops into one larger parabolic drop, is no longer reduced by mesa drop mergers. Rather, the overall gravitational energy is increasing, though not as much as the wetting layer energy is reduced. Thus coarsening is still favorable, but ΔE approaches a constant.

Distribution model for drop coarsening

Focusing on drops small enough that gravity is negligible, this chapter examines the evolution of the distribution of drop sizes during coarsening. It is motivated by the classical model of a coarsening binary alloy derived by Lifshitz and Slyozov [38] and, independently, by Wager [75]. Their model, known as the LSW model, consisted of an evolution equation for the distribution giving the frequency of finding a given sized particle scaled by the total number of particles. A mean-field approximation for the concentration of the supersaturated phase is an essential part of Lifshitz and Slyozov's description. The mean-field approximation replaces a concentration field that may be a function of space and time with a spatial average. Despite the model ignoring all spatial information, both from the concentration field and the location of the growing and shrinking particles, it successfully captured the power-law behavior of the number of particles versus time [73]. Moreover, this power law is found by a clever use of similarity variables [41] that describes an intermediate asymptotic solution — a self-similar distribution — that persists during the power-law coarsening. Subsequent modifications to this model improved on it by extending

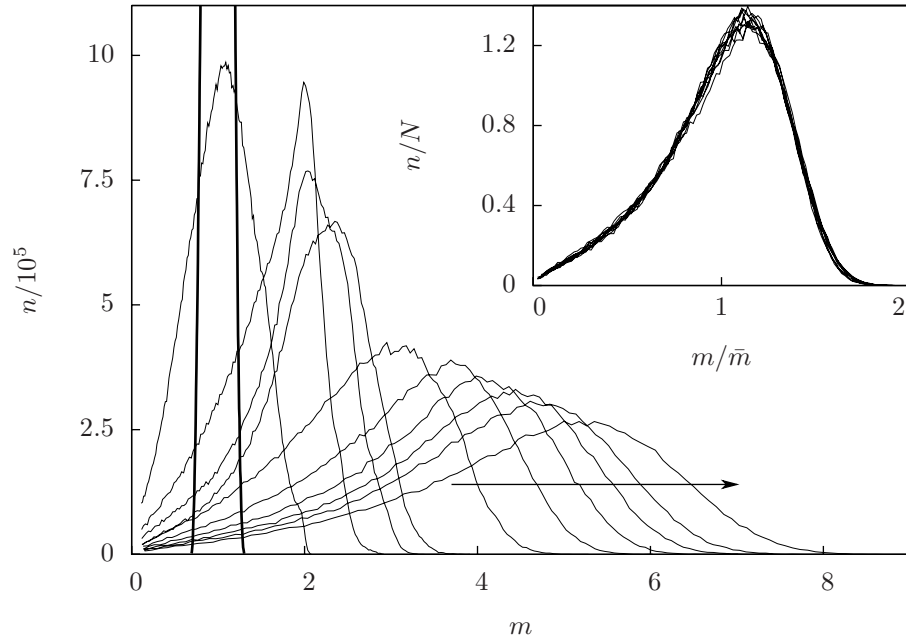


FIGURE 6.1: An initially uniform random distribution of drops converging to the similarity distribution. The arrow shows the direction on increasing time, while the inset re-plots the late-time curves to show the self-similar scaling.

it to cover systems densely packed with growing particles, or by replacing the mean-field approximation with more detailed statistics[74, 42, 72].

Turning to the drop mass distribution in film coarsening, Fig. 6.1 shows the result of a CDS simulation (4.40) starting with one million drops whose masses and separations were uniformly distributed ($0.6 < m < 1.3$ and $20 < \ell < 25$). Binning the drops by mass shows a histogram of drop sizes that shrinks in area as the number of drops decreases and grows in support as the population of surviving drops includes larger members. The inset shows a simple change of variables collapsing the long-time behavior onto one self-similar histogram. Like the initial data for this figure, we assume that $\mathbb{K} < 1$ throughout this chapter so that collisions do not occur. This assumption restricts the dynamics of the thin film CDS to LSW-like behaviors.

In this chapter, we explore this self-similar evolution by constructing an LSW-

like model for droplet coarsening. We examine the effect of the initial distribution of drop masses on the rate of convergence to the similarity distribution. We also observe far-from-similarity behavior in the CDS model with a distinctive “stairstep” pattern in $N(t)$. This same stairstep signature can be observed in other coarsening models (see [18, Fig. 6] for an example in image de-noising), though to the best of our knowledge, this phenomenon has yet to be described in the literature. Stairstep behavior provides an interesting example of how maximum average coarsening rates proved by the technique of Kohn and Otto [35] can be realized in non-self-similar forms.

We do not necessarily assume that drift is negligible, but we employ averaged quantities to avoid modeling drop spacing.¹

6.1 Mean-field model for drop distributions

This section first makes use of approximations developed in Chapters 3 and 4 to develop a LSW-like model. Secondly, it examines similarity solutions to this model and compares these to the self-similar histogram.

6.1.1 Model formulation

Let $n(m, t)$ be the distribution of drops with mass m at time t , scaled so that $\int_m^{m+\Delta} n(s, t) ds$ is the number of drops with masses between m and $m + \Delta$. Integrating over all masses gives

$$N(t) = \int_0^\infty n(m, t) dm, \tag{6.1}$$

the total drop at time t . We require $n(m, t) \rightarrow 0$ as $m \rightarrow \infty$ sufficiently rapidly so that $N(t)$ is finite.

¹ See 7.1 for more information on how this approach becomes invalid for larger values of \mathbb{K} .

The total active mass contained in all of the drops is

$$M_c = \int_0^\infty mn \, dm, \quad (6.2)$$

and, while the total number of drops may change, we know $M_c = \sum m_i$ to be approximately due to no-flux boundaries at the edges of the drop array. The total mass in the system includes the adsorbed UTF, $M_{tot} = \sum m_i + \delta L + O(\delta^2 L)$, where the last term represents the local deviation in the UTF. We assume that $\delta^2 L$, the total mass involved in the equilibration of the wetting layer, is small enough that conservation of mass for the drop cores holds.

We also assume that all drops of a particular mass grow or shrink in the same way in response to a mean-field flux. This assumption is almost certainly not true for any particular drop, but should hold on average. We will later check this assumption through comparison with CDS model simulations. This allows us to construct characteristics along which the drop population evolves.

As we neglect collisions, the only mechanism for a drop to be destroyed is collapse ($m \rightarrow 0$). If m_0 and m_1 are both positive, the number of drops between these two values is conserved. In terms of the distribution, this is

$$\int_{m_0}^{m_1} n(m, t) \, dm = u(m_1)n(m_1, t) - u(m_0)n(m_0, t); \quad (6.3)$$

drops only enter or leave the control volume at the edges. Differentiating in time, then dropping the integral since it is over an arbitrary region gives

$$\partial_t n + \partial_m (un) = 0. \quad (6.4)$$

Drop collapse events enter this model as a boundary condition $n(0, t) = 0$. This equation is a hyperbolic PDE written in conservation form.

To find u , we suppose a drop of mass m has virtual neighbors who are the mean distance away imposing an averaged value of the chemical potential $V(h)$ (4.31) on the central drop. Since the total length of the domain is conserved, the mean drop separation is

$$\ell(t) = \ell_0 N_0 / N = (\ell_0 / \bar{m}_0) \bar{m}(t), \quad (6.5)$$

where ℓ_0 is the average initial separation, and \bar{m}_0 is the average initial mass. The current mean mass may be computed as

$$\bar{m} = \frac{\int_0^\infty mn \, dm}{\int_0^\infty n \, dm} = \frac{M_c}{N(t)}. \quad (6.6)$$

The mean-field chemical potential is

$$V_c = \frac{1}{N(t)} \int_0^\infty V(m)n(m,t) \, dm, \quad (6.7)$$

where V_c varies in time. It is useful to define $m_c(t)$, the characteristic mass, by $V_c = V(h_m(m_c))$. We calculate $u(m)$ as the sum of the fluxes from the two identical virtual neighbor drops to the mass m drop, giving

$$u(m) = \frac{2}{\ell} \left[V(h_m(m)) - V_c \right]. \quad (6.8)$$

This can be simplified using (4.35) and (3.17) to obtain

$$V(h_m(m_c)) - V(h_m(m)) \sim \frac{\delta^3}{3^{5/4}} \left(\frac{1}{\sqrt{m_c}} - \frac{1}{\sqrt{m}} \right). \quad (6.9)$$

The characteristic speed becomes

$$u(m) = \frac{\beta}{\bar{m}\sqrt{m_c}} \left(1 - \sqrt{\frac{m_c}{m}} \right), \quad (6.10)$$

where the constant

$$\beta = \frac{2}{3^{5/4}} \delta^3 \mathbb{K} \quad (6.11)$$

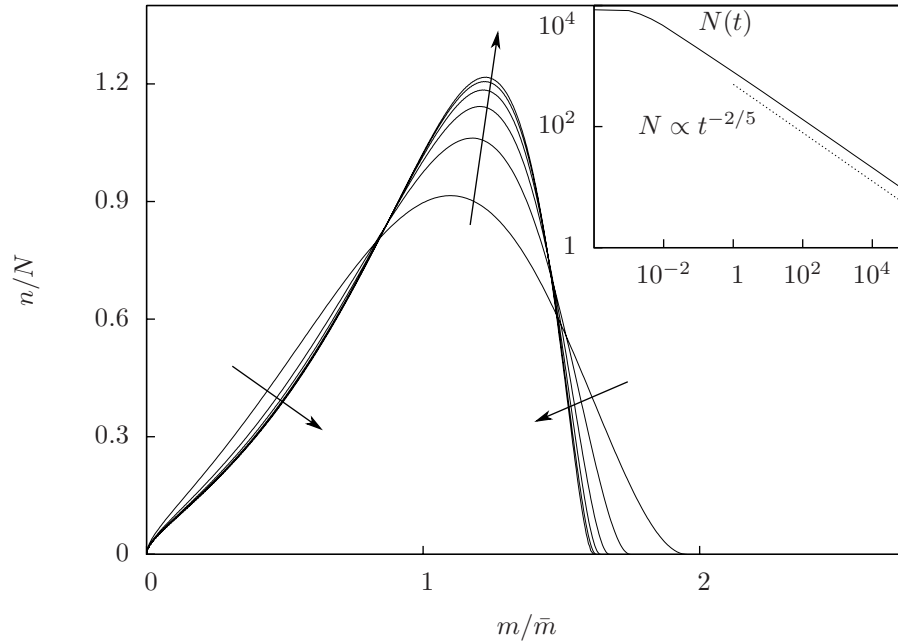


FIGURE 6.2: A numerical simulation of the drop distribution model (6.12) through a characteristic tracking method. In the inset, $N(t)$ exhibits power-law behavior for long times.

sets the timescale. Note that the timescale is inversely dependent on \mathbb{K} and scales like the flux as $O(\delta^{-3})$. The drop distribution model consists of

$$\partial_t n + \partial_m \left[\frac{\beta}{\bar{m} \sqrt{m_c}} \left(1 - \sqrt{\frac{m_c}{m}} \right) n \right] = 0 \quad (6.12a)$$

$$V(m_c) = \frac{1}{N(t)} \int_0^\infty V(m) n(m, t) dm \quad (6.12b)$$

$$\bar{m} = \frac{M_c}{\int_0^\infty n dm}. \quad (6.12c)$$

This is a transport-type equation with non-local terms m_c and \bar{m} in the characteristic velocity. Numerical simulation of this equation through characteristic tracking in Fig. 6.2 shows an initial distribution converging to a similarity shape. The inset shows $N(t)$ following the expected $t^{-2/5}$ power law for $\alpha = 0$ coarsening.

6.1.2 Asymptotic separation of variables

We solve (6.12) by making an intermediate asymptotic separation of variables. Let $\gamma = m_c/\bar{m}$. We rescale time by $t = t'/T$, $T = 1/\beta$ and drop the prime for convenience. This effectively accounts for the initial mass and separation data as a timescale; the initial data will not effect the form of the asymptotic distribution. We will suppose that

$$z = m/m_c, \quad t^b m_0 = m_c(t), \quad t^{-2a} f(z) = n(m, t), \quad (6.13)$$

for undetermined constants a and b . Note that other masses in the problem scale the same as m_c to leading order, and so γ should be a constant. This will be checked in CDS simulations shown below. The distribution $n(m, t)$ may have higher order time dependence, but we will focus on the leading order behavior that dominates at large times. This rescaled distribution is properly an intermediate asymptotic solution because there must be a time t_{\max} where $N(t_{\max}) = 1$ and the system has reached equilibrium. Using these rescalings in the conservation of mass equation (6.2), we see

$$M_c = t^{2b-2a} m_0^2 \int_0^\infty z f dz. \quad (6.14)$$

Since the left side does not depend on t , it must be the case that $b = a$. For $N(t)$, the rescaled equation is

$$N = t^{-a} m_0 \int_0^\infty f dz. \quad (6.15)$$

Next, we rescale (6.12a). The time derivative term is

$$\frac{\partial n}{\partial t} = \frac{\partial}{\partial t} \left[t^{-2a} f \left(\frac{m}{t^a m_0} \right) \right] = -t^{-2a-1} a (2f + z f'), \quad (6.16)$$

while the flux term is

$$\partial_m(un) = \frac{1}{m_c} \partial_z(un) = t^{-9a/2} C \left([1 - z^{-1/2}] f \right)', \quad (6.17)$$

where

$$C = \gamma m_0^{-5/2}.$$

Balancing powers of time in (6.16) and (6.17) yields

$$a = 2/5, \tag{6.18}$$

and so from (6.15)

$$N(t) \propto t^{-2/5}, \tag{6.19}$$

agreeing with previous models. The remaining ODE for the drop mass distribution $f(z)$ is

$$f' = \left(\frac{5C - 8z^{3/2}}{4z^{5/2} + 10Cz(1 - \sqrt{z})} \right) f. \tag{6.20}$$

We want smooth solutions with compact support on $0 \leq z \leq z_{\max}$, and we enforce this by choosing C and z_{\max} so that z_{\max} is an irregular singular point. Arguments in LSW theory (for example, [77, 9]) support this choice as it is the only one that preserves conservation of mass. This means that the denominator and its derivative in (6.20) are both zero at z_{\max} :

$$4z_{\max}^{5/2} + 10Cz_{\max}(1 - \sqrt{z_{\max}}) = 0 \tag{6.21a}$$

$$10z_{\max}^{3/2} + 10C - 15C\sqrt{z_{\max}} = 0. \tag{6.21b}$$

Solving this gives $z_{\max} = 9/4$ and $C = 27/10$. To determine γ and m_0 from C , we apply the change of variables $z = m/m_c$ to the definition of \bar{m} and calculate

$$\bar{m} = \frac{\int_0^\infty mn \, dm}{\int_0^\infty n \, dm} = m_c \frac{\int_0^{z_{\max}} z f \, dz}{\int_0^{z_{\max}} f \, dz} = m_c \int_0^{z_{\max}} z f \, dz. \tag{6.22}$$

Thus we can calculate γ independently from f as

$$\gamma^{-1} = \int_0^{z_{\max}} z f \, dz. \tag{6.23}$$

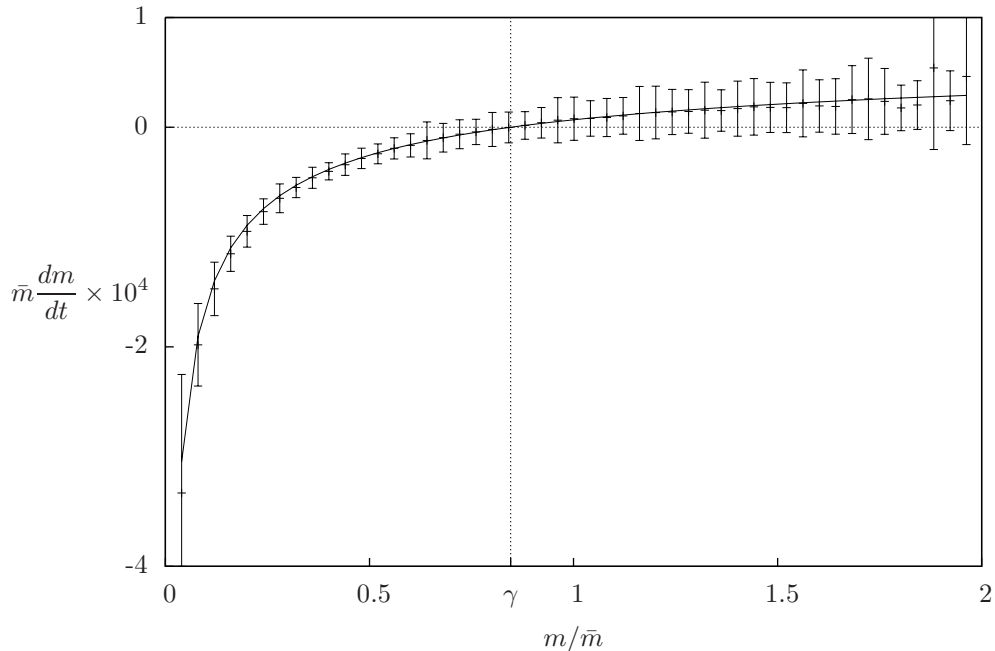


FIGURE 6.3: The characteristic velocity from the mean-field model compared to the bin-averaged velocities from a CDS simulation.

The equation (6.20) can be solved numerically starting at an arbitrary point $0 < z_0 < z_{\max}$ with arbitrary value $f(z_0)$ and integrating both left to 0 and right to z_{\max} , then scaling the result so that $\int_0^{z_{\max}} f dz = 1$. From the numerical solution to (6.20), we obtain $\gamma \approx 0.846$, a number that corresponds to the observed value of m_c in CDS simulations in Fig. 6.3. Here, $\frac{dm}{dt}$ is bin-averaged over a range of m for ≈ 25000 drops at a time well into the power-law coarsening regime. The error bars show the standard deviation in each bin, while the solid curve is the mean-field prediction. The agreement is quite good, especially for $m < \bar{m}$, and the predicted value of γ is a good estimate of the zero crossing point.

Figure 6.4 shows a comparison between the similarity solution (6.12) to the self-similar CDS histogram. The histogram shown is the average of 200 CDS simulations, each with identical initial drop distributions and parameters. The random seed used to generate the drop masses and separations from the distribution is different for each

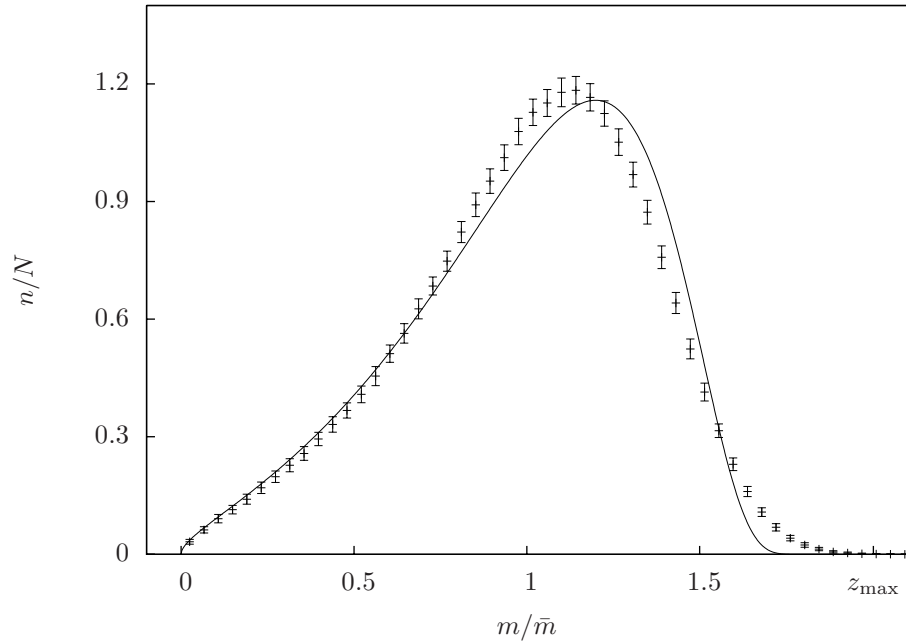


FIGURE 6.4: The asymptotic distribution f (solid line) compared to CDS histogram (points) averaged over 200 different realizations of the same random initial distribution. The error bars show the standard deviation in each bin. Both curves have been scaled to have area one.

run. Averaging over these different realizations is an attempt to reduce the influence of specific drop orderings to see the general trend. The error bars show the standard deviation of the number of drops in each bin. The solid line, $f(z)$, agrees with the histogram for $m < \bar{m}$. For larger drops there are significant differences between the curves. It is interesting to note that the LSW model has interesting uniqueness problems, especially with respect to perturbations to the large-mass portion of the histogram [11, 19, 49, 50]. We observed similar effects in (6.12). While (6.20) does indeed give a similarity solution in numerical computations, other initial distributions do not necessarily evolve toward it.

Asymptotic analysis of (6.20) shows that it has irregular singular points at each

edge of the distribution (one by design). At the left edge of support,

$$f \sim \sqrt{z}e^{\sqrt{z}} \quad \text{for } z \rightarrow 0^+. \quad (6.24)$$

At the right edge of support,

$$f \sim \exp\left(\frac{3}{z-z_{\max}}\right) \exp\left(\frac{541}{729}z\right) \quad \text{for } z \rightarrow z_{\max}^-. \quad (6.25)$$

The controlling factor for this expansion naturally depends on z_{\max} , which in turn depends on C . However, the expansion about $z = 0$ is independent of these parameters. Interestingly, the low-mass end of the distribution is where the best match with CDS histograms occurs.

6.2 Effect of the initial distribution

We now focus on the early times in the drop distribution evolution before the similarity scaling is valid. Noting that the form of the initial distribution was important in (6.12), we try different initial distributions of drop masses as initial conditions for the CDS model (4.40). We choose these distributions so that they are unlike the similarity distribution in some way. Figure 6.5 shows four choices: a normal distribution with a wider support, a triangle distribution with positive skew, a Gamma distribution $\text{PDF}(x) = xe^{-5x/2}/2.5^2$ with positive skew and a fat tail of large drops, and a Cauchy distribution with an even fatter tail (as well as undefined mean and variance). Bold red curves show the initial distribution, while the thinner blue lines show histograms evolving in similarity variables m/\bar{m} versus n/N . The green lines show the final histogram computed at $t = 10^{12}$. Each simulation uses $N_0 = 10^5$ initial drops and has $\mathbb{K} \approx 1/4$. The coarsening parameter is approximate because we must impose a maximum initial drop size for the unbounded distributions, effectively allowing us to compute \bar{m} even for the Cauchy distribution.

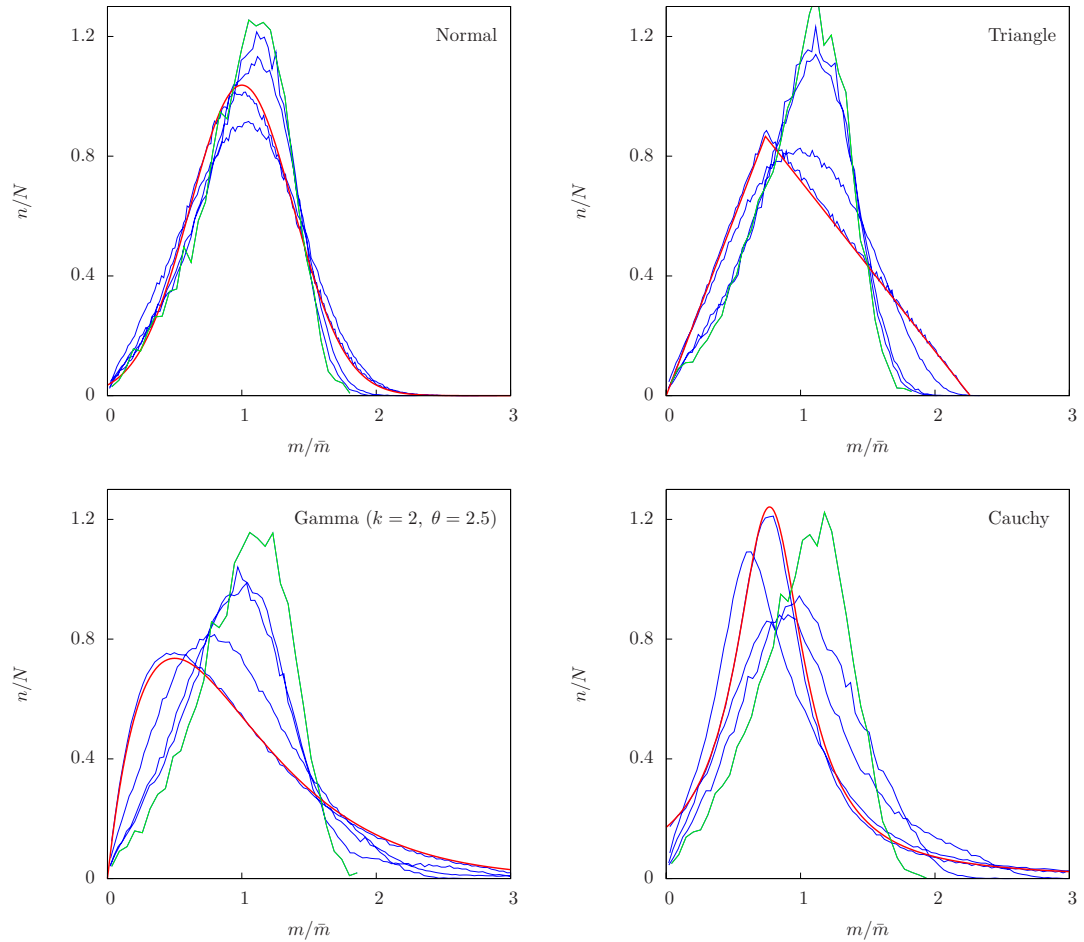


FIGURE 6.5: The evolution of four initial droplet mass distributions via the CDS model. The coarsening parameter \mathbb{K} is identical in each.

The large support of the normal distribution evidently does little to slow the evolution of the histogram toward similarity. Likewise, the positive skew of the triangle distribution quickly changes to negative skew, and the histogram in this simulation approaches similarity rapidly. These rapid convergence from these initial distributions is comparable to the convergence seen in the simulation in Fig. 6.1, where the initial distribution is uniform over a broad range of masses. In the simulation starting from a Gamma distribution, the large-drop tail evolves very slowly and seems to delay the change in skewness. This slow evolution of the large-mass tail is more dra-

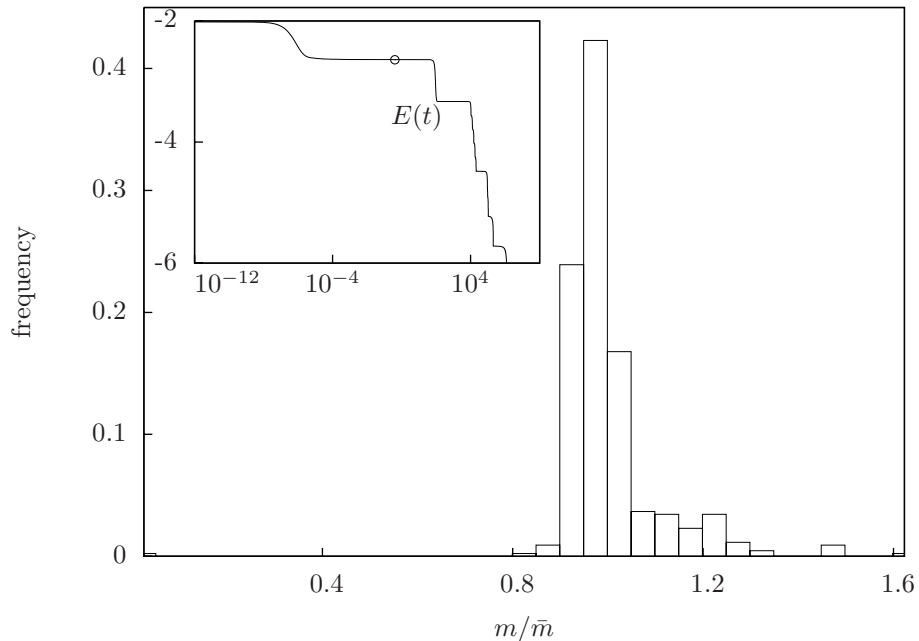


FIGURE 6.6: The distribution of drop masses from spinodal dewetting with $\delta = 0.1$ and $\alpha = 0$. This histogram was from one very large PDE simulation that dewetted to form 435 drops.

matic in the Cauchy initial distribution simulation, where the early evolution of the histogram does not appear to be approaching the similarity distribution in any way. Both the Gamma and Cauchy simulations also show small but significant deviations from the power law $N \propto t^{-2/5}$, even after $t = 10^{12}$. We conclude that initial distributions with fat tails of large drops can delay the onset of self-similar coarsening. This observation suggests that the uniqueness problems in the LSW model that occur at the large-mass end of the distribution [19] may also effect thin film drop coarsening.

The physical choice of initial distribution should be guided by the dewetting instability leading to initial drop formation. To this end, we performed a large simulation of the PDE (2.40) to see the resulting distribution of drop masses from the spinodal instability. For initial film thickness $\bar{h} = 0.3$ and domain size $L = 10^4$, we computed until the energy (3.1) decreased significantly and the rate of energy

decreased slowly. The histogram of the resulting 435 drops appears in Fig. 6.6. The inset shows the energy during the simulation with the circle representing the time at which the energy criteria were met and the histogram was computed. The collapse behavior after dewetting is visible in $E(t)$ to the right of the circle. The histogram is tightly clustered about the mean, and the drop center-to-center separation was quite uniform at $\ell_0 = 1/k_{\max}$ with no significant deviation.

Nucleation-based dewetting results in a different distribution of drops, but depends strongly on the location and number of nucleations (see [16] for more on the phenomenon). The structure of the nucleations in turn depends on their origins: material defects in the substrate, thermal fluctuations of the free surface height, contaminants in the fluid, and so on. Describing the drop distribution from nucleation dewetting requires making an assumption about the source of these perturbations in order to model how they appear across the surface of a fluid.

6.3 Early-time deviations: Stairsteps

We approximate the spinodal dewetting drop distribution in Fig. 6.6 by a uniform distribution with a very small width and set the drops to be a uniform distance apart. A CDS simulation of 10^5 drops in Fig. 6.7 shows an interesting far-from-similarity behavior in $N(t)$. Rather than power-law behavior, coarsening events are clustered into “stairsteps.” During each step, many drops collapse at nearly the same time, followed by a long period where no coarsening occurs. Eventually, the staircase features grow indistinct and the power-law behavior associated with self-similar coarsening appears (this is not shown in the figure). Figure 6.8 shows histograms at various times during coarsening denoted by circles on Fig. 6.7. Note each histogram is unscaled (m versus n), but the scale of the n axis decreases for later times. By (C), coarsening has begun, yielding a growing spike of large drops at the right edge of the

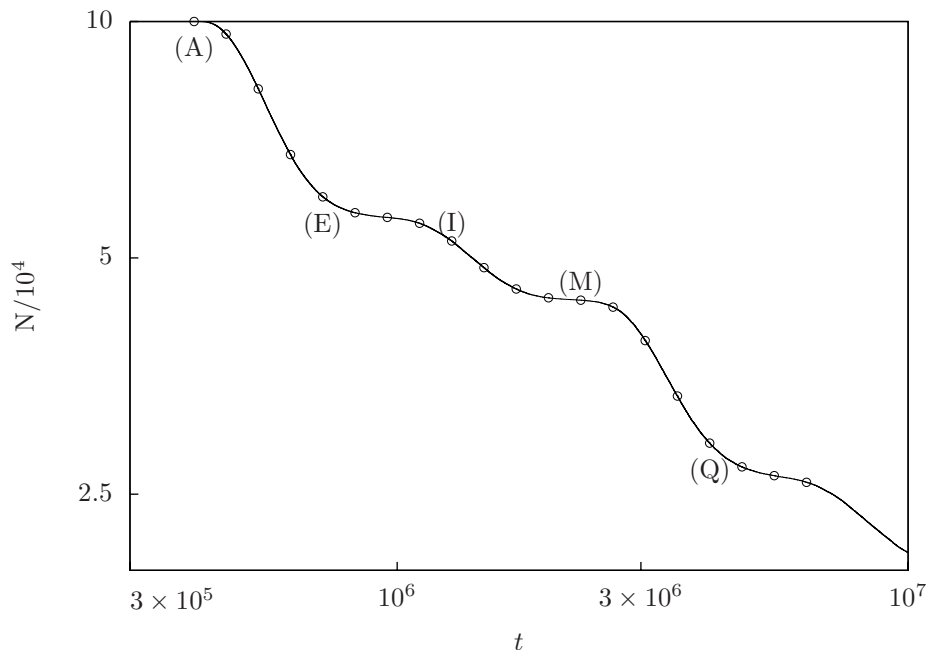


FIGURE 6.7: The far-from-similarity coarsening of an initially uniform random distribution of drops with a small variance. Circles correspond to histograms in Fig. 6.8. The first plot in each row of Fig. 6.8 is labeled here for reference.

distribution. However, coarsening proceeds too rapidly, and the population of small drops is depleted by (E). The distribution here is similar to the initial distribution in that it has a very small variance, but the data is bimodal. The smaller hump of the distribution causes another staircase (I)-(L) as it coarsens, but creates another spike at the large mass end. By (M), the distribution is similarly shaped to (E), though wider, and another staircase occurs. As steps continue, the distribution widens and gradually loses its recurring character.

By constructing a very special initial condition, we may prolong the staircase behavior arbitrarily. Suppose $N_0 = 2^J$, $\kappa < 1$, and ε is small. Then

$$m_j = \bar{m} + \varepsilon \mu_j \quad \text{for } j = 1, 2, \dots, N, \quad (6.26a)$$

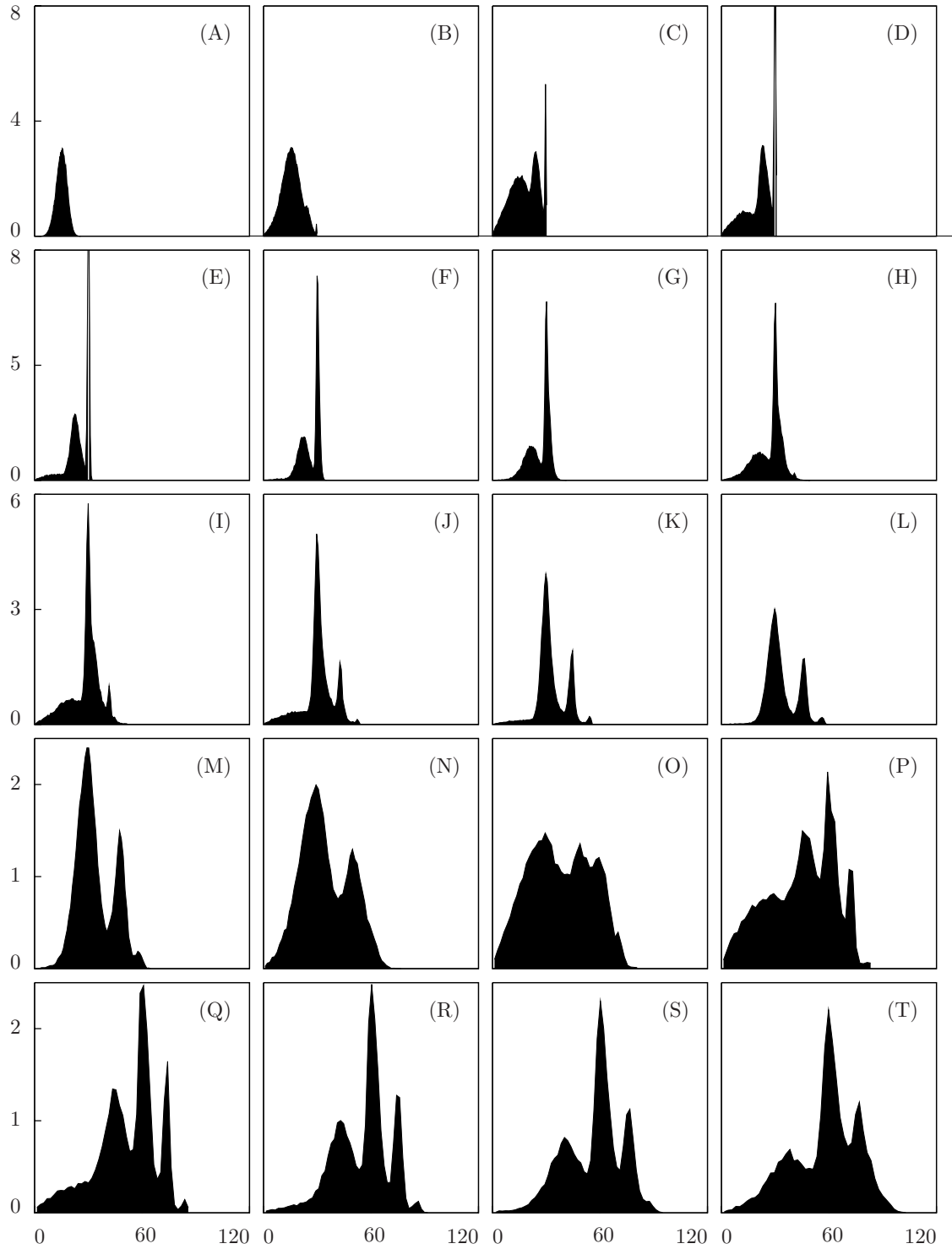


FIGURE 6.8: Histograms at various times during the coarsening simulation shown in Fig. 6.7. The vertical axis is in thousands of drops ($n/1000$), while the horizontal axis is in mass m .

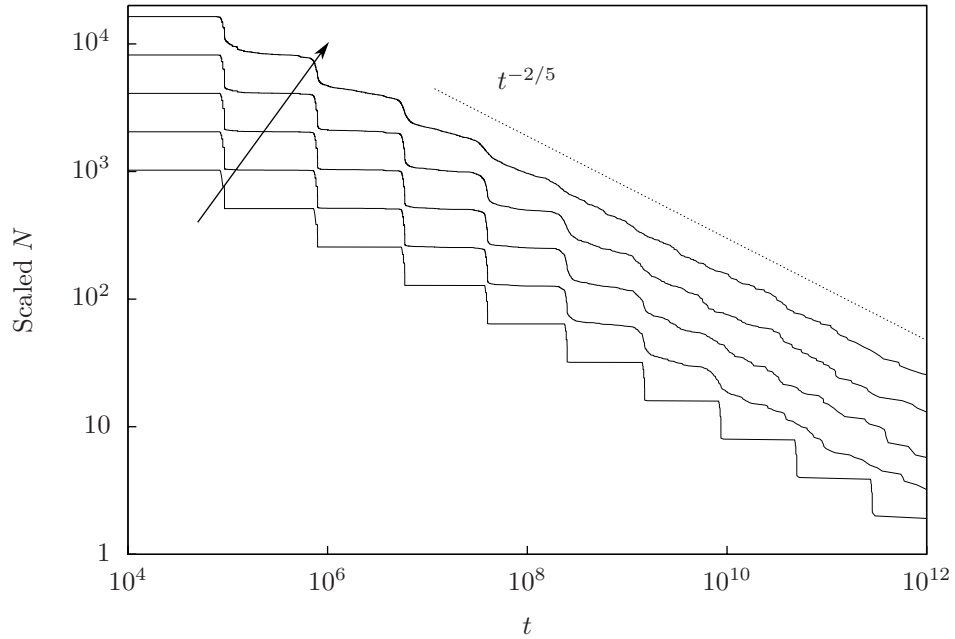


FIGURE 6.9: The coarsening of the “fractal” initial condition (6.26) in the CDS model. Each simulation has $N_0 = 2^{13}$, but N is scaled by powers of two so that the curves do not overlap. The arrow shows the direction of increasing disorder in the initial condition. For the lowest curve, the initial condition is undisturbed. Following the arrow, each curve has an identical distribution of masses, but with 0.5%, 1%, 2.5% and 5% of the drops randomly rearranged. The dotted line shows the power law corresponding to the similarity solution.

where

$$\mu_j = -\kappa^l + \sum_{k=0}^{k=l-1} \kappa^k \quad \text{for } l \text{ given by } \gcd(2^l, j) = 2^l, \quad (6.26b)$$

is an initial condition with $M_c = \bar{m}N_0$ (provided an extra $\kappa^J \varepsilon$ is added to m_{N_0}). This initial condition forces every even indexed drop to be larger than its neighboring odd indexed drops, but also every drop whose index is divisible by four is larger than every drop whose index is divisible by two, and so on. The coarsening events are predetermined. Drops with $l = 0$ disappear in the first stairstep, then drops with $l = 1$ in the second, and so on until one drop remains. Figure 6.9 shows the result of several CDS simulations with $N_0 = 2^{13}$ initial drops. For clarity, N has been

arbitrarily divided or multiplied by two so that curves do not overlap. The lowest curve is the result of (6.26) alone. The other curves have had this condition slightly perturbed by swapping the locations of between 0.5% and 5% of drops at random before the simulation begins. At long times, the $t^{-2/5}$ power law is clearly visible in the higher curves. The ratio of the time between stairsteps is approaching $2^{5/2}$ from above, in agreement with the power law. This provides an interesting example of how the prediction in [54] holds as an upper bound on the mean coarsening rate.

We do not yet understand the full connection between the small variance distribution and (6.26), but the behaviors are similar. Further work is needed especially to describe the pause in coarsening following a stairstep. While it is necessary so that the mean coarsening rate stays below $t^{-2/5}$, the mechanism through which smaller drops are depleted faster than they are generated is unclear in the uniform initial distribution case. In addition, techniques to improve on the mean-field approximation in the distribution model (6.12) could be imported from previous work on the LSW model. These may provide a similarity distribution that better approximates the CDS histogram.

Future directions for research

Droplet coarsening is a rich problem with many open questions to be explored. The addition of other physics, such as negative gravity for hanging drops [23] or the evaporation of drops[56], has potential to yield interesting behaviors. Even without extra complications, there are two issues unaddressed in the basic model. First, drop coarsening is interesting in that it involves two independent modes of coarsening: collision and collapse. We have focused on collapse dominated coarsening, but collision coarsening has several unexplored features. Second, this work has been focused on one-dimensional coarsening. The true physical problem operates in two dimensions, with the associated increase in complexity.

7.1 Collision dominated coarsening distributions

Glasner and Witelski [25] noted that the $N \propto t^{-2/5}$ coarsening rate was the same if the coarsening events were mostly collapses, mostly collisions, or a mix of the two events. This result is in agreement with Otto et al. [54], whose result puts this power law as the upper bound on the time-averaged coarsening rate. However, the self-similar LSW-style coarsening described in Chapter 6 deals only with collapse events.

It would be interesting to construct a similar averaged model for collision dominated coarsening. The “conservation of drops” assumption leading to 6.12 no longer holds if collision events are possible. Two drops of non-zero mass may annihilate themselves and produce a drop of a different size. These sorts of events have been modeled before in other contexts by the Smoluchowski equation (see [66, 40] for instance). In the usual context, this model describes the diffusive motion of rafts of atoms across a two-dimensional substrate. Interaction kernels model the probability of collisions between different sized rafts. Under strong assumptions on the form of these kernels, this model may be solved.

However, the adaption of this sort of model to describe droplet collisions will require further work to understand the details of Smoluchowski-type models. Drop collisions are perhaps more difficult to model than other coarsening-by-collision systems because the most likely collision scenario involves three drops. A pair of drops traveling together with a larger drop chasing a faster-moving smaller drop will encounter another singleton blocker drop whose presence prevents the smaller drop from escaping. The actual collision involves the coalescence of only two of the drops, the smaller drop and either the chaser or blocker.

Another interesting feature of collision dominated coarsening is that while the arguments in Chapter 6 about mean mass and mean separation still hold, they are less descriptive of the state of the system. Given that $N \propto t^{-2/5}$, then by the no-flux boundary conditions at the edges of the domain, $\bar{m} \propto t^{2/5}$ and $\ell \propto t^{2/5}$. However, the three-drop interactions typical of collision dominated coarsening cause large variance in $\bar{\ell}$. Figure 7.1 [25] (reprinted here from [25, Fig. 14]) shows that drops tend to travel in pairs whose separation is much smaller than ℓ . After a collision event involving three drops, the newly coalesced drop and the other large survivor are now in close proximity. Together they form a new large drop/small drop pair with a small separation between them. The pair moves off, coarsening again by collision when

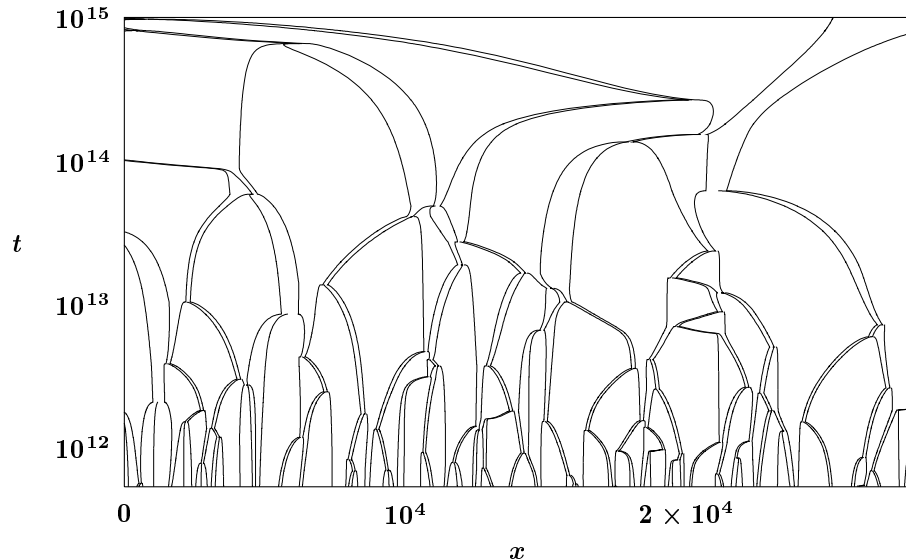


FIGURE 7.1: World lines of colliding droplets with $\mathbb{K} = 1.5$. Each curve represents the center of mass of a droplet. Here, $\delta = 0.01$. (From [25, Fig. 14], reprinted by permission.)

another blocker drop approaches. A statistical description of this coarsening process must be able to model this extra spatial correlation between drops.

It would be very interesting to see if CDS simulations show radically different histograms of drop sizes for collision dominated coarsening than for collapse dominated coarsening. If so, it may go to explain the observations of Limary and Green [39] that drop populations did not follow an LSW-style negatively skewed distribution, but were positively skewed in a manner more consistent with the Smoluchowski model.

7.2 Coarsening in two dimensions

Extending this work to two dimensions would allow for comparison to physical models and potentially new behavior. Some pioneering work on this topic has been carried out by Pismen and Pomeau [56], although details in Figure 5 appear to show small drops moving toward larger ones, the opposite of what we predict here. Preprints by Glasner [21] and Glasner et al. [20] support our conclusions.

The extension of our model two two dimensions could be accomplished by revising the steady-state drop description (Chapter 3) to cover radially symmetric drops. The CDS derivation would be similar, and the flux terms in (4.40) would become

$$\frac{dP_i}{dt} = C_p(P_i) \int_{|\vec{x}-\vec{X}_i|=w_i} \nabla\mathcal{V} \cdot \vec{n} ds, \quad \frac{d\vec{X}_i}{dt} = C_x(P_i) \int_{|\vec{x}-\vec{X}_i|=w_i} \nabla\mathcal{V} ds, \quad (7.1)$$

where \vec{n} is the outward unit normal from the contact line $|\vec{x} - \vec{X}_i| = w(P_i)$. To find $\nabla\mathcal{V}$, the elliptic problem (4.33) must be solved in two dimensions. Including the proper boundary conditions, this is

$$\begin{aligned} \nabla^2\mathcal{V} &= 0 \\ \mathcal{V} &= V(h_m(P_i)) \quad \text{at } |x - X_i| = w(P_i) \text{ for } i = 1 \dots N \\ \nabla\mathcal{V} \cdot \vec{n} &= 0 \quad \text{at } \partial\Omega, \end{aligned} \quad (7.2)$$

where Ω is the domain. The domain has hole of radius $w(P_i)$ at each drop with a Dirichlet condition specified around each edge. This boundary value problem is similar to the one studied by McKenney et al. [45], though they consider a Dirichlet condition on $\partial\Omega$ as well. Their method allows for a solution on a coarse grid throughout the domain with a finer discretization of the edge of each domain hole. An even faster formulation may be possible, since we only want $\nabla\mathcal{V}$ on $|\vec{x} - \vec{X}_i| = w(P_i)$. The dilute limit (see Sec. 4.4) could be used to reduce the domain holes to forcing-function terms in the PDE.

The LSW technique is a more promising approach. It can be employed to replace the flux integral with a mean-field flux in a natural way. This would be enough to obtain an expression for the coarsening rate and the distribution shape. However, it would be (a) restricted to collapse dominated coarsening and (b) without the corroborating support provided by a large numerical simulation.

Appendix A

Physical variables simulation of the lubrication equation

It is advantageous to be able to compute solutions to the lubrication equation (2.40) that provide not only the height $h(x, t)$, but also provide accurately the pressure $p(x, t)$ and the flux $J(x, t)$. All of these quantities enter into the CDS model in Chapter 4. This appendix describes a numerical scheme simulating (2.40) as four coupled first order partial differential equations. This scheme allows for the easy addition of additional physics through the modification of the pressure, the imposition of proscribed fluxes at the boundary, and other modifications to (2.40) that are useful for working with a coarsening system of drops. The disadvantage of this scheme is that it involves computing $4N - 2$ points to find h on a size N grid. It is similar to a two-equation scheme proposed [27] that tracks only h and p , splitting the problem into parabolic and elliptic parts.

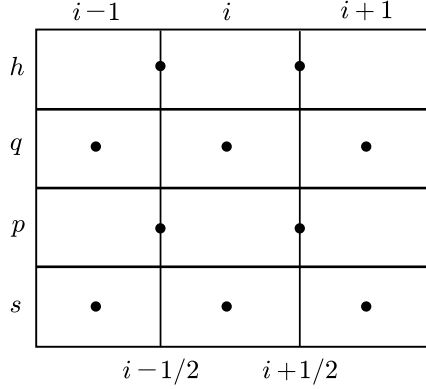


FIGURE A.1: The stencil for the four-equation discretization of the film equation (2.40)

A.1 Discretization

We rewrite (2.40) as

$$\partial_t h = \partial_x q, \tag{A.1a}$$

$$q = h^3 \partial_x p, \tag{A.1b}$$

$$p = -\partial_x s + U'(h), \tag{A.1c}$$

$$s = \partial_x h, \tag{A.1d}$$

where h is the height, q is the (negative) flux, p is the pressure, and s is the slope. This is similar to the Keller box method [32]. Only (A.1a) has time dependence; the other equations are coupled boundary value problems. Like a differential-algebraic system, the equations for q , p , and s serve as constraints on the h equation.

We discretize our quantities in space and time. We show a Backward Euler time difference, but in practice we employ θ -weighting to achieve closer to $O(\Delta t^2)$ accuracy. To keep the bandwidth small, we will use second order differences in space to approximate derivatives in x , and we will compute every-other variable at cell sides ($i + \frac{1}{2}$), see the stencil diagram Fig. A.1. On N grid points on a domain of

	$h_{i-3/2}$	$p_{i-3/2}$	q_{i-1}	s_{i-1}	$h_{i-1/2}$	$p_{i-1/2}$	q_i	s_i	$h_{i+1/2}$	$p_{i+1/2}$	q_{i+1}	s_{i+1}
$h_{i-1/2}$		0	▲	0	▲	0	▲	0				
$p_{i-1/2}$			0	▲	▲	▲	0	▲	0			
q_i				0	▲	▲	▲	0	▲	▲		
s_i					▲	0	0	▲	▲	0	0	

FIGURE A.2: A packing diagram for a 4×4 block of the Jacobian of the four equation system (A.2). A “▲” represents a non-zero entry.

$0 \leq x \leq L$, $\Delta x = L/N$ and $x = i\Delta x$. This gives

$$\frac{1}{\Delta t} (h_{i-1/2}^{n+1} - h_{i-1/2}^n) - \frac{1}{\Delta x} (q_i - q_{i-1}) = 0 \quad (\text{A.2a})$$

$$q_i - \frac{\bar{h}_i^3}{\Delta x} (p_{i+1/2} - p_{i-1/2}) = 0 \quad (\text{A.2b})$$

$$p_{i-1/2} + \frac{1}{\Delta x} (s_i - s_{i-1}) - U'(h_{i-1/2}) = 0 \quad (\text{A.2c})$$

$$s_i - \frac{1}{\Delta x} (h_{i+1/2} - h_{i-1/2}) = 0 \quad (\text{A.2d})$$

where quantities without superscripts are at time $n+1$ and $\bar{h}_i = \frac{1}{2} (h_{i+1/2} + h_{i-1/2})$. Boundary conditions are required for q and s at $i=0$ and $i=N$, leaving the total number of points in the domain at $4N-2$. This discretization is implicit, and must be solved through some root-finding method. We employ a Newton method, but there are some choices as to the form of the residual r and Jacobian J that arise from the packing order of $\{h, q, p, s\}$. We choose

$$r = [h_{1/2}, p_{1/2}, q_1, s_1, \dots, h_{i-1/2}, p_{i-1/2}, q_i, s_i, \dots, h_{N-1/2}, p_{N-1/2}]^T. \quad (\text{A.3})$$

This packing of r provides J with a tight band structure. One can verify that this packing has minimal bandwidth by enumerating all possible packings (that is $\{h, p, q, r\}$, $\{h, q, p, r\}$, $\{q, p, r, h\}$, \dots), but in general this can be achieved by grouping all of the quantities with left-leaning stencils, followed by the quantities with right leaning stencils, as in (A.3). The band structure of the Jacobian consists of 4×4 blocks, packing i quantities with $i-1/2$ quantities, as seen in Fig. (A.2). The

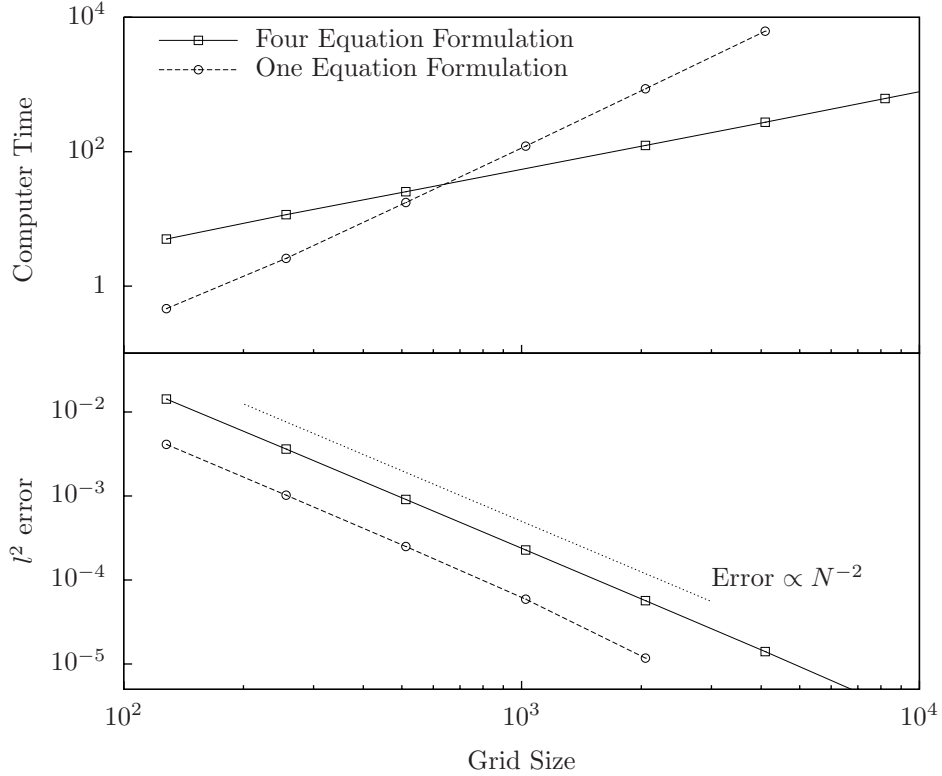


FIGURE A.3: The computer time for a test problem using the traditional one equation approach for the film equation and the four equation approach (A.1).

bandwidth is seven, but the work required to compute each entry is minimal as most are constant.

Knowing the structure of r and J , we can now solve the linear system by LU factorization on a $7 \times (4N - 2)$ problem and use the result in a Newton solver to find the quantities h , p , q , and s at the next time-step. In practice, we employ LAPACK to perform the factorization at each Newton step, and about three Newton steps are required for convergence each time-step using the L^2 norm of the update as the convergence criterion.

Figure A.3 shows the running time for a test problem of a parabola on a δ -height UTF relaxing towards steady-state for two time units. Computations are carried out using (A.1) and using a traditional one equation formulation with a width five

stencil. Both methods are using Backward Euler time differences. Interestingly, (A.1) is faster for larger grids, with a cross-over occurring at about 1000 grid points. Both methods are second order accurate in space, as can be seen in the lower panel.

A.2 Initial conditions and adaptive time-stepping

If an initial condition (IC) h^0 is specified for height, it is necessary to generate the values of p^0 , q^0 , and s^0 . The simplest approach is to use the residual equations (A.2) to generate, in order, s^0 , p^0 , then q^0 . In practice, this procedure results in small deviations between the chosen IC and the effective IC.

The film equation is sensitive to the form of the initial condition (though the four equation formulation is less so), and effective computation requires adaptive time-stepping so that small steps may be taken initially, followed by larger steps once the IC is “acclimated”. In addition, since we are interested in simulating coarsening, a metastable phenomena, it very practical to be able to take large time steps when the change in h is small. We use a simple adaptive time-step algorithm that can be summarized as

1. Use Newton’s Method to solve (A.2). If the error after any step is less than ε_0 , go to step (3).
2. If after M iterations of Newton’s Method the error is still larger than ε_0 , stop.
3. If the error is less than $\varepsilon_1 > \varepsilon_0$, accept the time-step, increase Δt by a small multiplicative factor, and go to step (1).
4. Otherwise, reject the time-step, reduce Δt by a large multiplicative factor, set h , p , q , and s to their values at the previous time, and go to (1).

If Δt becomes smaller than machine precision, the algorithm terminates and further solution is impossible.

Bibliography

- [1] G.I. Barenblatt. *Scaling*. Cambridge U. P., Cambridge, U.K., 2003.
- [2] C.M. Bender and S.A. Orszag. *Asymptotic Methods and Perturbation Theory*. Springer-Verlag, New York, 1999.
- [3] F. Bernis and A. Friedman. Higher order nonlinear degenerate parabolic equations. *J. Diff. Eq.*, 83(1):179–206, 1990.
- [4] A.J. Bernoff and T.P. Witelski. Linear stability of source-type similarity solutions of the thin film equation. *Appl. Math. Lett.*, 15(5):599–606, 2002.
- [5] A.L. Bertozzi. The mathematics of moving contact lines in thin liquid films. *Not. Am. Math. Soc.*, pages 689–697, June/July 1998.
- [6] A.L. Bertozzi, G. Grün, and T.P. Witelski. Dewetting films: bifurcations and concentrations. *Nonlinearity*, 14:1569–1592, 2001.
- [7] J. Bischof, D. Scherer, S. Herminghaus, and P. Leiderer. Dewetting modes of thin metallic films: Nucleation of holes and spinodal dewetting. *Phys. Rev. Lett.*, 77(8):1536–1539, 1996.
- [8] D. Bonn, J. Eggers, J. Indekeu, J. Meunier, and E. Rolley. Wetting and spreading. Submitted to *Rev. Mod. Phys.*, 2007.
- [9] A.J. Bray. Theory of phase-ordering kinetics. *Adv. Phys.*, 43(3):357–459, Jun 1994.
- [10] F. Brochard-Wyart, H. Hervet, C. Redon, and F. Rondelez. Spreading of “heavy” droplets: 1. Theory. *J. Coll. Int. Sci.*, 142(2):518–527, 1991.
- [11] J.A. Carrillo and T. Goudon. A numerical study on large-time asymptotics of the Lifshitz-Slyozov system. *J. Sci. Comput.*, 20(1):69–113, February 2004.
- [12] H.-C. Chang and E.A. Demekhin. *Complex Wave Dynamics on Thin Films*, chapter 9, pages 271–285. Elsevier, 2002.
- [13] S. Dai and R.L. Pego. Universal bounds on coarsening rates for mean-field models of phase transitions. *SIAM J. Math Anal.*, 37(2):341–371, 2005.

- [14] P.-G. de Gennes. Wetting: statics and dynamics. *Rev. Mod. Phys.*, 57(3):827–863, July 1985.
- [15] P.-G. de Gennes, F. Brochard-Wyart, and D. Quere. *Capillarity and wetting phenomena: drops, bubbles, pearls, waves*. Springer Verlag, New York, 2003.
- [16] J.A. Diez and L. Kondic. On the breakup of fluid films of finite and infinite extent. *Phys. Fluids*, 19:072107, 2007.
- [17] J. Eggers. Contact line motion for partially wetting fluids. *Phys. Rev. E*, 72:061605, 2005.
- [18] S. Esedoğlu and J. Greer. Upper bounds on the coarsening rate of discrete, ill-posed, nonlinear diffusion equations. To appear in *Commun. Pure Appl. Math.*
- [19] B. Giron, B. Meerson, and P.V. Sasorov. Weak selection and stability of localized distributions in Ostwald ripening. *Phys. Rev. E*, 58(4):4213–4216, Oct 1998.
- [20] K. Glasner, F. Otto, T. Rump, and D. Slepčev. Ostwald ripening of droplets: The role of migration. To appear in *Phys. Fluids*.
- [21] K.B. Glasner. Ostwald ripening in the thin film equations. Unpublished, available online.
- [22] K.B. Glasner. Spreading of droplets under the influence of intermolecular forces. *Phys. Fluids*, 15(7):1837–1842, July 2003.
- [23] K.B. Glasner. The dynamics of pendant droplets on a one-dimensional surface. *Phys. Fluids*, 19:102104, 2007.
- [24] K.B. Glasner and T.P. Witelski. Coarsening dynamics of dewetting films. *Phys. Rev. E*, 67:016302:1–12, 2003.
- [25] K.B. Glasner and T.P. Witelski. Collision versus collapse of droplets in coarsening of dewetting thin films. *Physica D*, 209:80–104, 2005.
- [26] M.B. Gratton and T.P. Witelski. Coarsening of unstable thin films subject to gravity. *Phys. Rev. E*, 77:016301, 2008.
- [27] G. Grün and M. Rumpf. Simulation of singularities and instabilities arising in thin film flow. *Euro. J. Appl. Math*, 12:293–320, 2000.

- [28] S. Herminghaus and F. Brochard. Dewetting through nucleation. *C. R. Physique*, 7:1073–1081, 2006.
- [29] S. Herminghaus, K. Jacobs, K. Mecke, J. Bischof, A. Fery, M. Ibn-Elhaj, and S. Schlagowski. Spinodal dewetting in liquid crystal and liquid metal films. *Science*, 282(5390):916–919, 1998.
- [30] L.M. Hocking. The influence of intermolecular forces on thin fluid layers. *Phys. Fluids*, 5(4):793–798, April 1993.
- [31] C. Huh and L.E. Scriven. Hydrodynamic model of steady movement of a solid/liquid/fluid contact line. *J. Colloid Interf. Sci.*, 35(1):85–101, 1971.
- [32] H.B. Keller. *Numerical solutions of partial differential equations*, volume II, chapter A new difference scheme for parabolic problems, pages 327–350. Academic Press, 1971.
- [33] J.R. King. ‘Instantaneous source’ solutions to a singular nonlinear diffusion equation. *J. Eng. Math*, 27(1):31–72, 1993.
- [34] J.R. King and M. Bowen. Moving boundary problems and non-uniqueness for the thin film equation. *Eur. J. Appl. Math*, 12:321–356, 2001.
- [35] R.V. Kohn and F. Otto. Upper bounds on coarsening rates. *Commun. Math Phys.*, 229(3):275–295, 2002.
- [36] R.S. Laugesen and M.C. Pugh. Properties of steady states for thin film equations. *Eur. J. Appl. Math*, 11:293–351, June 2000.
- [37] L. Leger and J.F. Joanny. Liquid spreading. *Rep. Prog. Phys.*, 55(4):431–486, 1992.
- [38] I.M. Lifshitz and V.V. Slyozov. The kinetics of precipitation from supersaturated solid solutions. *J. Phys. Chem. Solids*, 19(1/2):35–50, 1961.
- [39] R. Limary and P.F. Green. Dynamics of droplets on the surface of a structured fluid film: late-stage coarsening. *Langmuir*, 19(6):2419–2424, 2003.
- [40] A. Lo and R.T. Skodje. Kinetic and monte carlo models of thin film coarsening: Cross over from diffusion-coalescence to Ostwald growth modes. *J. Chem. Phys.*, 112(4):1966–1974, 2000.

- [41] J.A. Marqusee and J. Ross. Kinetics of phase transitions: Theory of Ostwald ripening. *J. Chem. Phys.*, 79(1):373–378, 1983.
- [42] J.A. Marqusee and J. Ross. Theory of Ostwald ripening: Competitive growth and its dependence on volume fraction. *J. Chem. Phys.*, 80(1):536–543, 1984.
- [43] A. Martin, O. Rossier, A. Buguin, P. Auroy, and F. Brochard-Wyart. Spinodal dewetting of thin liquid films at soft interfaces. *Euro. Phys. J. E*, 3:337–341, 2000.
- [44] O.K. Matar, R.V. Craster, A. Münch, and T.P. Witelski. Euromech 490: Dynamics and stability of thin liquid films and slender jets. In *Discussion*, 2007.
- [45] A. McKenney, L. Greengard, and A. Mayo. A fast Poisson solver for complex geometries. *J. Comput. Phys.*, 118:348–355, 1995.
- [46] V. Mitlin. Dewetting revisited: New asymptotics of the film stability diagram and the metastable regime of nucleation and growth of dry zones. *J. Colloid Interf. Sci.*, 227:371–379, 2000.
- [47] V.S. Mitlin. Dewetting of a solid surface: analogy with spinodal decomposition. *J. Colloid Interf. Sci.*, 156:491–497, 1993.
- [48] V.S. Mitlin and N.V. Petviashvili. Nonlinear dynamics of dewetting: kinetically stable structures. *Phys. Lett. A*, 192:323–326, 1994.
- [49] B. Niethammer and R.L. Pego. Well-posedness for measure transport in a family of nonlocal domain coarsening models. *Indiana U. Math J.*, 54:499–530, 2005.
- [50] B. Niethammer and J.J.L. Velázquez. Global stability and bounds for coarsening rates within the mean-field theory for domain coarsening. *Commun. Part. Diff. Eq.*, 31:1679–1708, 2006.
- [51] A. Oron and S.G. Bankoff. Dynamics of a condensing liquid film under conjoining/disjoining pressures. *Phys. Fluids*, 13(5):1107–1117, 2001.
- [52] A. Oron, S.H. Davis, and S.G. Bankoff. Long-scale evolution of thin liquid films. *Rev. Mod. Phys.*, 69:931–980, 1997.
- [53] W. Ostwald. *Lehrbruck der Allgemeinen Chemie*, volume 2. Leipzig, Germany, 1896.

- [54] F. Otto, T. Rump, and D. Slepčev. Coarsening rates for a droplet model: rigorous upper bounds. *SIAM J. Math. Anal.*, 38(2):503–529, 2006.
- [55] L.M. Pismen. Nonlocal diffuse interface theory of thin films and the moving contact line. *Phys. Rev. E*, 64:021603:1–9, 2001.
- [56] L.M. Pismen and Y. Pomeau. Mobility and interactions of weakly nonwetting droplets. *Phys. Fluids*, 16(7):2604–2612, 2004.
- [57] C. Pozrikidis. Effect of surfactants on film flow down a periodic wall. *J. Fluid Mech.*, 496:105–127, December 2003.
- [58] G. Reiter. Dewetting of thin polymer films. *Phys. Rev. Lett.*, 68(1):75–78, 1992.
- [59] G. Reiter, A. Sharma, A. Casoli, M.-O. David, R. Khanna, and P. Auroy. Thin film instability induced by long-range forces. *Langmuir*, 15:2551–2558, 1999.
- [60] O. Reynolds. On the theory of lubrication and its application to Mr. Beauchamp Tower’s experiments, including an experimental determination of the viscosity of olive oil. *Royal Society, Phil. Trans.*, 1, 1886.
- [61] L.W. Schwartz. Unsteady simulation of viscous thin-layer flows. In *Free surface flows with viscosity*, pages 203–233. Computational Mechanics Publications, Boston, 1997.
- [62] L.W. Schwartz, R.V. Roy, R.R. Eley, and S. Petrash. Dewetting patterns in a drying liquid film. *J. Colloid Interf. Sci.*, 234:363–374, 2001.
- [63] R. Seemann, S. Herminghaus, and K. Jacobs. Dewetting patterns and molecular forces: a reconciliation. *Phys. Rev. Lett.*, 86(24):5534–5537, 2001.
- [64] A. Sharma. Many paths to dewetting of thin films: Anatomy and physiology of surface instability. *Euro. Phys. J. E*, 12(3):397–407, November 2003.
- [65] A. Sharma and R. Verma. Pattern formation and dewetting in thin films of liquids showing complete macroscale wetting: From ”pancakes” to ”swiss cheese”. *Langmuir*, 20(23):10337–10345, 2004.
- [66] D.S. Sholl and R.T. Skodje. Late-stage coarsening of adlayers by dynamic cluster coalescence. *Physica A*, 231(4):631–647, 1996.
- [67] I. Stakgold. *Green’s Functions and Boundary Value Problems*. John Wiley & Sons, Inc., 1998.

- [68] V. M. Starov, M. G. Velarde, and C. J. Radke. *Wetting and Spreading Dynamics*. CRC Press, Boca Raton Florida, 2007.
- [69] L.H. Tanner. Spreading of silicone oil drops on horizontal surfaces. *J. Phys. D*, 12(9):1473, 1979.
- [70] U. Thiele. Open questions and promising new fields in dewetting. *Euro. Phys. J. E*, 12(3):409–414, November 2003.
- [71] U. Thiele, M.G. Velarde, K. Neuffer, and Y. Pomeau. Film rupture in the diffuse interface model coupled to hydrodynamics. *Phys. Rev. E*, 64:031602, 2001.
- [72] K. Tsumuraya and Y. Miyata. Coarsening models incorporating both diffusion geometry and volume fraction of particles. *Acta Metall.*, 31(3):437–452, 1983.
- [73] P.W. Voorhees. The theory of Ostwald ripening. *J. Stat. Phys.*, 38(1/2):231–252, 1985.
- [74] P.W. Voorhees and M.E. Glicksman. Ostwald ripening during liquid-phase sintering – effect of volume fraction on coarsening kinetics. *Metall. Mater. Trans. A*, 15(6):1081–1088, 1984.
- [75] C. Wagner. Theorie der alterung von niederschlagen durch umlosen (Ostwald-Reifung). *Z. Elektrochem*, 65:581, 1961.
- [76] S.J. Watson, F. Otto, B.Y. Rubinstein, and S.H. Davis. Coarsening dynamics of the convective Cahn-Hilliard equation. *Physica D*, 178(3-4):127–148, April 2003.
- [77] D. Weaire and S. McMurry. Some fundamentals of grain growth. *Solid State Phys.*, 50:1–35, 1996.
- [78] M.B. Williams and S.H. Davis. Nonlinear theory of film rupture. *J. Colloid Interf. Sci.*, 90:220–228, 1982.
- [79] T.P. Witelski and A.J. Bernoff. Dynamics of three-dimensional thin film rupture. *Physica D*, 147(1-2):155–176, 2000.
- [80] T.P. Witelski, D.G. Schaeffer, and M. Shearer. A discrete model for an ill-posed nonlinear parabolic PDE. *Physica D*, 160:189–221, 2001.
- [81] W.W. Zhang and J.R. Lister. Similarity solutions for van der Waals rupture of a thin film on a solid substrate. *Phys. Fluids*, 11(9):2454–2462, 1999.

- [82] L. Zhornitskaya and A.L. Bertozzi. Positivity-preserving numerical schemes for lubrication-type equations. *SIAM J. Numer. Anal.*, 37(2):523–555, 2000.

Biography

Michael Brian Gratton was born on June 5, 1979 in Topeka, Kansas, USA. He obtained his B.S. in Mathematics from Harvey Mudd College in May 2002 and his M.A. and Ph.D. in Mathematics from Duke University in May 2004 and April 2008, respectively. Gratton has accepted a three year postdoctoral fellowship in applied mathematics at Northwestern University.

Gratton served as Graduate Student Representative for two terms, 2003–2004 and 2005–2006, and was an active participant in the Mathematical Problems in Industry (MPI) from 2004 onwards. He co-authored the paper “Coarsening of unstable thin films subject to gravity” with Thomas P. Witelski [26].